Thermomechanical and Vibration Analysis of Stiffened Unitized Structures and Threaded Fasteners

Balakrishnan Devarajan

Dissertation submitted to the Faculty of the

Virginia Polytechnic Institute and State University

in partial fulfillment of the requirements for the degree of

Doctor of Philosophy

in

Engineering Mechanics

Rakesh K. Kapania, Chair

Mark S. Cramer

Saad A. Ragab

Gary D. Seidel

Scott W. Case

December 10, 2018

Blacksburg, Virginia

Keywords: Thermomechanical, stiffener, threaded fasteners, isogeometric analysis, NURBS, dynamic and eigenvalue analysis

Thermomechanical and Vibration Analysis of Stiffened Unitized Structures and Threaded Fasteners

Balakrishnan Devarajan

(ABSTRACT)

This dissertation discusses the thermomechanical analyses performed on threaded fasteners and curvilinearly stiffened composite panels with internal cutouts. The former problem was analyzed using a global/local approach using the commercial finite element software ANSYS while a fully functional code using isogeometric analysis was developed from scratch for the latter. For the threaded fasteners, a global simplified 3D model is built to evaluate the deformation of the structure. A second local model reproducing accurately the threads of the fasteners is used for the accurate assessment of the stresses in the vicinity of the fasteners. The isogeometric analysis code, capable of performing static, buckling and vibration analysis on stiffened composite plates with cutouts using single patch, multiple patches and level set methods is then discussed. A novel way to achieve displacement compatibility between the panel and stiffeners interfaces is introduced. An easy way of modeling plates with complicated cutouts by using edge curves and generating a ruled NURBS surface between them is described. Influence on the critical thermal buckling load and the fundamental mode of vibration due to the presence of circular, elliptical and complicated cutouts is also investigated. Results of parametric studies are presented which show the influence of ply orientation, size and orientation of the cutout, and the position and profile of the curvilinear stiffener.

The numerical examples show high reliability and efficiency when compared with other published solutions and those obtained using ABAQUS, a commercial software.

Thermomechanical and Vibration Analysis of Stiffened Unitized Structures and Threaded Fasteners

Balakrishnan Devarajan

(GENERAL AUDIENCE ABSTRACT)

Aircraft in flight are subjected to different loads due to maneuvers and gust; there external forces cause internal loads and depend on the location of the panel in the aircraft. The internal loads, may result in the buckling of the panel. Hence, there is a need for studying structural efficiency and develop strong and stiff lightweight structures. Stiffened composite panels is a technology capable of addressing these needs. However, when used in space vehicles moving at hypersonic speeds, such structures experience significant temperature rise in a very short time resulting from the aerodynamic heating due to friction between the vehicle surface and the atmosphere. Such phenomena is more prominent during reentry and launch processes. Hence, it is really important to consider thermal effects while designing and analyzing such structures. Composite stiffened panels have many advantages like small manufacturing cost, high stability, great energy absorption, superior damage tolerance etc. One of the main failure modes for stiffened composite panels is thermal buckling. An extensive literature review on thermal buckling of stiffened composite panels was conducted in this dissertation. Thermal buckling and vibration analysis as well as a parametric study of a stiffened composite panel with internal cutouts was conducted, and verified using ABAQUS, a Finite Element Software.

Dedication

To my parents: Devarajan and Lakshmi

Thank you for your endless support in this journey

For keeping faith in me

For being there when I needed you

Thank you for everything

Acknowledgments

I would like to express my heartfelt gratitude to my research advisor Dr. Rakesh K. Kapania for his invaluable guidance and support in helping me conduct and complete this work. I would also like to thank the members of my Ph.D committee, Dr. Saad Ragab, Dr. Mark Cramer, Dr. Scott Case and Dr. Gary Seidel for their support. A big thanks to all the people I have come to know through the course of my time at Virginia Tech and Blacksburg, I will always enjoy and cherish your friendship. I would like to acknowledge, Institute for Critical Technology and Applied Science (ICTAS), Ahmic Aerospace and AFRL-VT-WSU for their financial support. Special thanks to Dr. Shuvodeep De for being there to answer all my academic and research questions.

Contents

List of Figures

List of Tables

Chapter 1

Introduction

1.1 Literature Review

1.1.1 Design and analysis of threaded fasteners

Threaded connections like bolts, screws and fasteners are common structural components in any assembled mechanical assembly. These types of connections are widely employed since they not only provide a mean to connect different components, but they also allow structures to be assembled and disassembled with greater ease compared to welded and riveted joints. Threaded connections have been analyzed for years by hand calculations. As the complexities in geometry and loading arose, finite element method started to be increasingly used for such analyses. Most of the initial analyses were conducted on 2-D axisymmetric models. Mackerle [3] presented a review of the finite element methods for the analysis of fasteners and joining system including threaded connections, bolted joints and screws. Le [4] investigated the interaction and stresses developed in an actual 3-dimensional helical threaded screw using PATRAN/NASTRAN and correlated the results with widely accepted theory and experimental results. A methodology for calculating stress distributions

at the roots of screw threads in initial clamping state and obtaining stress concentration factor (SCF) using a 3D stress analysis on bolted joints under tensile loadings was presented by Sawa *et al.* [5]. Rafatpanah [6] developed a method to generate the three-dimensional thread geometry without discontinuities in ANSYS and compared the results with those obtained using typical hand calculations.

Submodeling technique was used by Shoji and Sawa [7] to calculate the stress at the root of bolt threads. Islam and Kapania [8] employed a similar global/local technique to capture the stress distribution in an adhesive joint by discretizing it with a very fine finite element mesh. Fukuoka and Nomura [9] proposed an effective modelling scheme for three dimensional finite element analysis, which could accurately construct helical thread geometry using the equations defining the thread cross section perpendicular to the bolt axis. It was possible to construct finite element models of bolted joints with high accuracy and computational efficiency. Henson and Hornish [10] evaluated common analysis methods for bolted joints in launch vehicles. To the best of authors' knowledge, there is very little literature describing the behavior of threaded inserts as the ones considered in the following work.

Ransom and Knight [11] present a schematic for global/local solution strategy. The terms *submodeling* and *global/local analysis* are often seen to be used in literature with the latter more in papers pertaining to composite panels. Kapania et al. [12] implemented a global/local analysis and calculated the static response of simply supported composite plates with circular cut-outs. Haryadi et al. [13] extended this by using the Ritz method in the global analysis and the finite-element method for the local analysis. Motivated by their work, Jrad

et al. [14] showed the feasibility of ABAQUS to perform the global/local analysis of a notched plate.

1.1.2 Composite stiffened panels using Isogeometric analysis

In recent times, unitized structures are being used to construct lighter and more environment friendly aircraft. The key idea of such a design is to have the stiffening members as an integral part of the structure [15]. Advanced multi-layered composite materials offer high strength to weight ratios and are hence being increasingly used in aerospace and shipbuilding industries amongst others. However, when used in hypersonic space vehicles such structures experience significant temperature rise in a short time resulting from the aerodynamic heating due to friction between the vehicle surface and the atmosphere. Such phenomena is more prominent during reentry and launch processes. For this reason, considering the thermal effects is important in design and analysis of such structures.

Numerous researchers in the past have investigated this problem. Noor and Burton [16],[17] and [18] analyzed the thermal buckling of laminated composite plates using 3D equations of elasticity. Although such an approach can yield exact solutions, it is unable to solve complex geometries with different boundary conditions. Furthermore, 3D modeling of plates can be computationally very expensive. However, the computational cost can be reduced without compromising much on the accuracy by deducing 2D models from the 3D models by means of several approximations and assumptions. The major 2D theories are : the linear classical thin plate theory (CPT) by Kirchhoff [19, 20], the first order shear deformation theory

(FSDT) [21, 22, 23] and the higher order shear deformation theory (HSDT) [24, 25, 26]. Of these, the CPT delivers very good results for thin plates and FSDT for moderately thick plates. However while using FSDT, it is imperative to use shear correction factors (SCFs) to amend the unrealistic shear strain energy, which are problem specific and are cumbersome to compute in some cases [27]. To eliminate these shortcomings, Higher-Order Shear Deformable Theories (HSDT) including the higher-order terms of the in-plane displacement [28, 29, 30, 31] have been proposed. However, these theories do not capture interlaminar shear stresses accurately. To overcome this shortcoming, researchers have come up with layer-wise (LW) theories [32, 33] and zigzag (ZZ) theories [34]. Layer-wise theory models shear distribution separately for each ply and hence has achieves consistent and detailed stress distributions. For predicting higher modes or for thicker composite plates, use of layer-wise theory is highly recommended. However such methods are computationally expensive for instance, the number of degrees of freedom to be solved in a layer-wise theory formulation increases as the number of plate layers increase. Hence, such methods also have to rely a lot on hybrid approaches to capture the interlaminar behavior more accurately.

Isogeometric Analysis (IGA) was introducted by Hughes et al. [35, 36] which implements an isoparametric formulation by using NURBS basis functions to describe the geometry and to construct the finite basis approximations. The IGA developed rapidly and has been successfully applied in various fields [37, 38, 39, 40, 41] including laminated composite plates [42, 43, 44] and functionally graded plates under a thermal environment [28, 45, 46]. Even though Qin et al.[47] used IGA isogeometric analysis to analyze the static response of stiff-

ened panels, studies emphasizing isogeometric analysis for the thermal behavior of stiffened composite plates are limited. Several authors in the past have studied the behavior of stiffened plates. A finite element algorithm was developed by Mukhopadhyay and Mukherjee [48] to study the buckling of stiffened panels under uniaxial compression. Prusty and Satsangi [49] used the same algorithm to perform structural analysis of stiffened isotropic plates and shells.

Due to an increase in requirement of laminated composite for a plethora of engineering applications, the use of plates with arbitrarily shaped cutouts are unavoidable. The response of structures to loads can be significantly affected due to the presence of cutouts. Since the study of laminated composites with cutouts is a complex problem, numerical methods are used extensively. Vibration and buckling analysis of such structures have been performed using various numerical approaches like the finite strip method [50], the finite element method (FEM) [51, 52, 53], meshfree methods [54], Rayleigh —Ritz method [55] and [56], extended finite element method (XFEM) [57]. Isogeometric analysis [35], [58] is being widely used over the last ten years. It offers many benefits such as exact geometry representation, easy mesh refinement, higher-order continuity, and it avoids the mesh generation procedure when using the traditional way. Many insights into splines techniques [59], mathematical properties [60], [61] and integration method [62], [63] have been gained. Many problems have been successfully solved using IGA including fluid mechanics [60], plates and shells [64], [65], [43], [42] damage and fracture mechanics [66], contact mechanics [67] and structural shape optimization [68].

1.1.3 Modeling curvilinearly stiffened panels using Level Set method

The higher-order smoothness of the NURBS basis functions have huge benefits with regards to the analysis of plates and shells. Based on the Kirchhoff plate theory, construction of rotation-free isogeometric shell was first proposed [69], and then developed for multiple NURBS patches by Kiendl [70]. Later, this element was extended for vibration and buckling analyses of laminated plates [2], functionally graded plates [65], bending and buckling analysis of laminated composite plates [42, 43, 44] and cloth simulation [67].

However, most of the problems investigated were single-patch structures and simple geometry. In the case of a clover shaped internal cutout (Figure 4.7) where the geometry is much more complex, a trimmed NURBS surface is useful. A NURBS surface and a set of ordered boundary curves lying within the parameter space of the surface [71] can be used to describe a trimmed NURBS surface. Shojaee et al. [2, 72] divided a rectangular plate with a heart shaped cutout into multiple NURBS patches, and to ensure continuity between adjacent patches, the authors applied the bending strip method. However this approach is quite cumbersome to implement and is also observed to complicate the unification of design and analysis, which is the sole aim of IGA. Trimmed NURBS surfaces were handled by Schmidt et al. [73] using a local reconstruction technique, which can handle trimmed NURBS surfaces under an isogeometric analysis framework. The method involved reconstructing trimmed NURBS patches using a least square approximation or by an interpolation method having known the trimming curves. The method is effective and can be easily applied to an

arbitrarily shaped area on the surface. However, the method could not exactly describe trimmed boundaries and the number of sampling points heavily influence the accuracy of the reconstructed boundaries. In order to model complex geometry problems, the IGA has been used in combination with an enrichment function similar to XFEM, to develop XIGA [74]. It has also been used in combination with the finite cell method (FCM) [75] and [76]. In this method, internal cutouts were described using level sets. However, level set methods using IGA were developed mostly elastostatic problems, and are yet to be implemented for thermal buckling analysis of stiffened laminated plates with complicated internal cutouts. The objective of this research, is to fill this gap.

Thermal effects, especially thermal buckling is important to be considered in design and analysis. Such problems have been researched by many in the past. For instance, Noor and Burton [16],[77] and [18] used 3D elasticity to analyze the thermal buckling of multilayered and sandwich plates. However, it is difficult to solve problems which involve complicated geometry under different boundary conditions. The problem becomes even more challenging if the plate is reinforced with stiffeners.

Several authors in the past have studied the behavior of such stiffened plates. A finite element algorithm was developed by Mukhopadhyay and Mukherjee [48] to study the buckling of stiffened panels under uniaxial compression. Prusty and Satsangi [49] used the same algorithm to perform structural analysis of stiffened isotropic plates and shells. While the aforementioned authors studied straight stiffeners, curvilinearly stiffened panels were analyzed by Tamijani and Kapania [78], Zhao and Kapania [1] and Shi et al. [79]. It has been

found by Hao et al. [80] that curvilinear stiffeners if used can improve the strength margins of panels since they reinforce the cutouts in them. The tension field resulting due to the presence of curvilinear stiffeners was examined and the loading path was compared with results obtained using straight stiffeners.

1.1.4 Free vibration of stiffened panels

Liew et al [81, 82] studied the free vibration of intermediate inclined stiffeners [82]. They used the first order shear deformation theory for the plate formulation.

Reddy and Khdeir [83] used multiple plate theories in their detailed work on the buckling and vibration responses of composite laminated plates. Carrera et al. [84] studied the problem of thin composite plate vibrations when subjected to in-plane loads using the Carrera unified formulation. Lee and Lee [82] used the first-order shear-deformation theory on stiffened anisotropic plates to study the effects of the fiber ply orientation, aspect ratio, and the positioning of the stiffeners on the free vibration mode shapes. Rikards et al. [85] used an equivalent layer shell theory to study the buckling and vibration responses of laminated composite stiffened shells. Patel et al. [86] used finite element approach to analyze the static and dynamic instability of stiffened shells when subjected to uniform in-plane harmonic edge loading.

The Differential Quadrature (DQ) method was used by Zeng and Bert [87] and it was extended to study the free vibration of eccentrically stiffened plates. The DQ method is based on approximation of a function and hence its partial derivatives with respect to a

space variable can be assumed by a linear sum of the function values at discrete grid points. It works very well in solving boundary value problems. Wei et al. [88] developed the discrete singular convolution (DSC) method and analyzed the free vibration of a plate. The DSC algorithm is based on the distribution and wavelet theories. Differential equations are solved numerically via the singular kernels of data type. The DSC is able to predict higher frequencies of plates (Zhao et al. [89]); however, DSC method has not been applied for more complicated structures.

The moving least square (MLS) method reconstructs continuous functions from a set of data. Recently, the MLS data interpolation technique was used to establish the Ritz method for the vibration analysis of plates by Zhou and Zheng [90]. Researchers have also applied the MLS technique to analyze structural problems using the meshfree method [78]. The essential boundary conditions were enforced through a point substitution technique. They studied the convergence, the influence of grid points, the MLS radius of influence, and the number of Gaussian integration points. Olson and Hazell [91] and Olson [92] used laser holography for vibration problems in ribbed plates. Bedair and Troitsky [93] studied the fundamental frequency characteristics of stiffened plates with a simply supported boundary condition with concentric or eccentric stiffeners using energy formulation and mathematical programming technique . Liu et al. [94] performed sensitivity analysis of the fundamental natural frequency.

Sheikh and Mukhopadhyay [95] used the finite element method to study the large amplitude free flexural vibration and transient response of eccentrically stiffened plates. They focused

on how the laying way and the eccentricity affected the frequency of structures.

1.1.5 Dissertation Outline

This dissertation is divided into six chapters. Chapter 2 discusses the thermomechanical analysis of threaded fasteners. The chapter details the preliminary 2D analysis conducted using different bolt models and discusses the difference in the results for thermal and mechanical loads. The model and material properties of a hypersonic wind tunnel sensor are then detailed and the results of the global local analysis are presented. Chapter 3 introduces the concept of isogeometric analysis and provides basic mathematical foundations. The chapter then discusses the concept of patches in a NURBS framework and achieving displacement compatibility between the stiffener and the plate. This part of the chapter is expected to provide the reader details of how the proposed method is efficient and less time consuming to analyze stiffened plates with complicated cutouts. Chapter 4 tackles the same problem using level set method to model the cutouts. The level set method is discussed in detail along with mathematical foundations and the results are compared with the multipatch method and with available literature. Chapter 5 extends the multipatch method to analyze free vibration problems and Chapter 6 summarizes the results and discusses scope for future work in the area.

Chapter 2

Thermo-Mechanical Analysis and Design of Threaded Fasteners

2.1 Introduction

Threaded inserts are additional components used to improve the performance of bolted connections, especially when the connecting parts are made of softer material like aluminum or copper. These devices are usually made of hard steel, they are characterized by a threaded hole to secure the bolt and they are pressed in the connecting part with whom they interlock producing a stronger bond as opposed to just drilling a filleted hole in the soft metal. The overall strength of the joint is improved and thread damage is avoided. Quite often, keylocking threaded inserts are used which are easy to install and remove. The keys are driven down into the threads of the surrounding base material, locking the insert in place. Furthermore, keylocking mechanism provides a positive mechanical lock against rotation. The mounted threaded insert with keylocking mechanisms analyzed in this work is visualized in Figure 2.1.

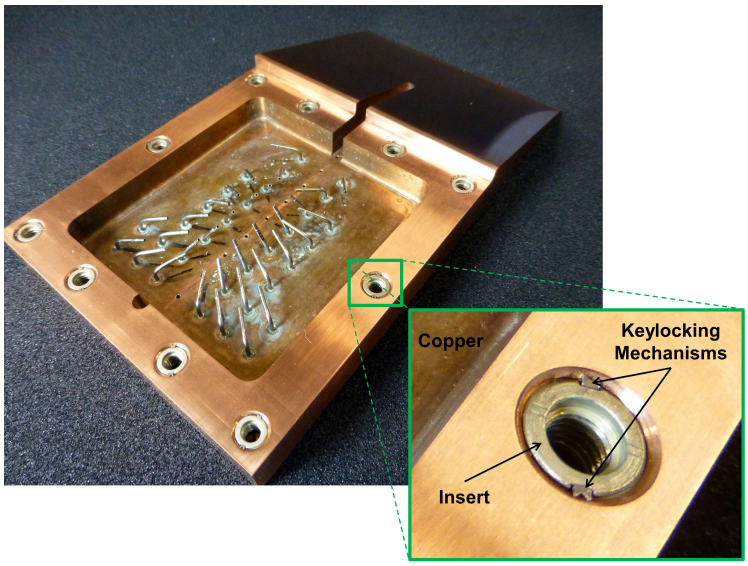

Figure 2.1: Threaded insert with keylocking mechanisms mounted in the copper component of a sensor.

When subjected to thermal loading, the interface between the insert and the part can experience high stresses due to differential expansion caused by different coefficient of thermal expansion (CTE) characterizing the connecting parts, the insert and the bolt. This chapter presents a global/local analysis of such an interface and to study how a highly realistic modelling of the region affects the stress concentration calculations. Global/local analysis has been used to analyze critical components for over 25 years.

Here, A two-step approach is proposed where first a global model is analyzed by assuming a geometrical approximation of threaded bolts and inserts as featureless cylinders. The stresses in the global model arise as a result of the highly constrained interaction at the interface between bolts, inserts and the soft material. Analyzing the entire model using a greater mesh refinement and accurate geometric features in order to obtain more accurate results at the interface will be time consuming and costly. Hence, the approach is to build a submodel

of the local region around the insert, characterized by realistic geometry modelling and finer mesh, to capture the stress distribution more accurately.

Submodeling is also known as the cut-boundary displacement method as the displacements calculated at the cut boundary of the global model are specified as the boundary conditions for the submodel. Deriving from the St Venant's principle, the stress concentration effects are localized and hence if the boundaries of the submodel are sufficiently far away from the interface, accurate results can be obtained. Submodeling techniques has the advantages of eliminating the need for complicated transition regions in solid mesh models and also enables one to experiment with different designs at the region of interest without regenerating a complete new mesh thus, using fewer resources.

2.2 Preliminary Analysis

Before approaching the analysis of a real tri-dimensional structure a preliminary study is carried out taking advantage of an ANSYS benchmark model (ANSYS Documentation\MechanicalAPDL\Technology Demonstration Guide\39.Bolt Thread Simulation) [96]. The purpose of this analysis is to gain knowledge about the thermo-mechanical behavior of threaded joints and the impact of different modeling techniques on the predicted maximum stress of the assembly. In particular, two different ways to model the interface between the bolt and the connecting components were considered: 1) bonded contact without modeling the thread, and 2) frictional contact with detailed modeling of the thread geometry. The models are visualized in Figures 2.2(a) and 2.2(b) respectively.

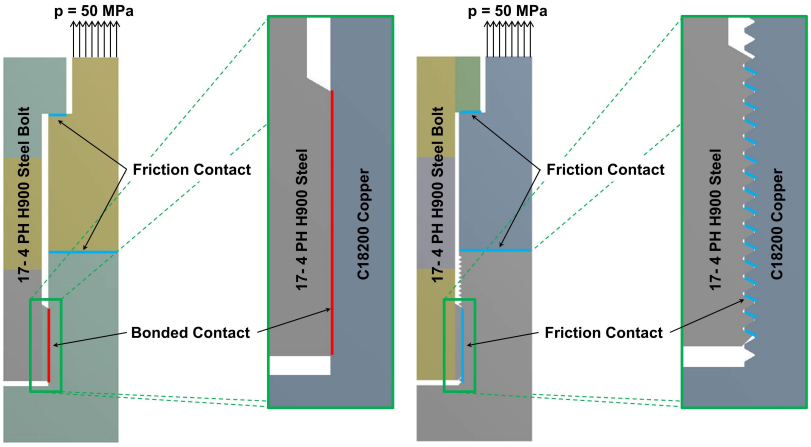

(a) Bolt with bonded contact (b) Bolt with friction contact

Figure 2.2: Bolt modeling techniques

Both modeling techniques are commonly used for representing bolted connections, however, the effect of thermal loads may generate substantial differences in the stress distribution predicted, causing a gross overestimation of the maximum stress developing in the bolt. Two types of loads are applied to each model: 1) mechanical load in the form of a 50 MPa positive pressure applied on the top of the assembly and, 2) thermal load in the form of uniform temperature of 150 $^{\circ}F$. The von Mises stresses developing in the structure subjected to these load conditions are visualized in Figure 2.3. If only the mechanical pressure is applied to the assembly, the stress distribution is little affected by the type of bonded contact and by the fact that the thread geometry is modeled or simplified into a smooth surface (Figures 2.3(a) and 2.3(b)). These results were expected since this modeling technique is widely used to simplify the mesh of bolted joint subjected to mechanical loads and is known to be rather accurate in reproducing the correct stress distribution.

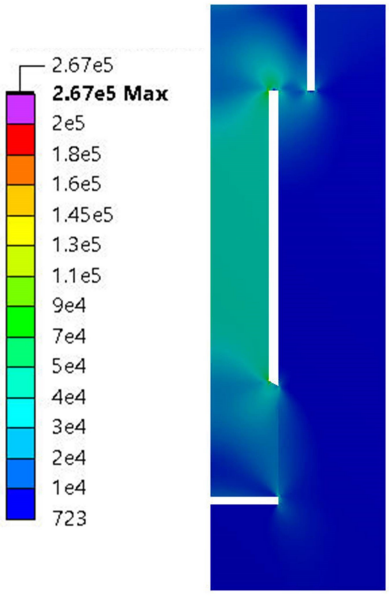

(a) Bonded contact : Pressure

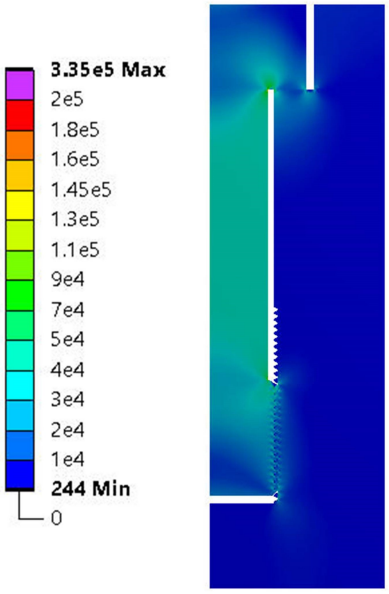

(b) Friction contact : Pressure

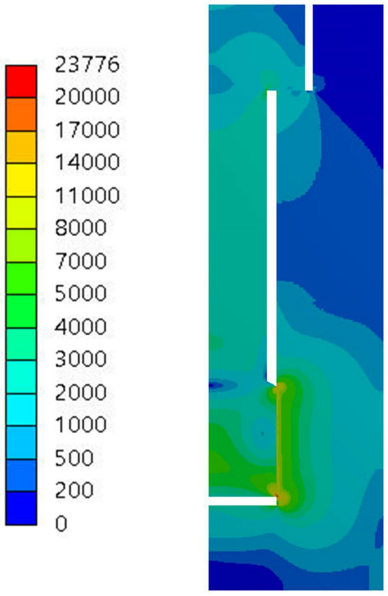

(c) Bonded contact : Temperature

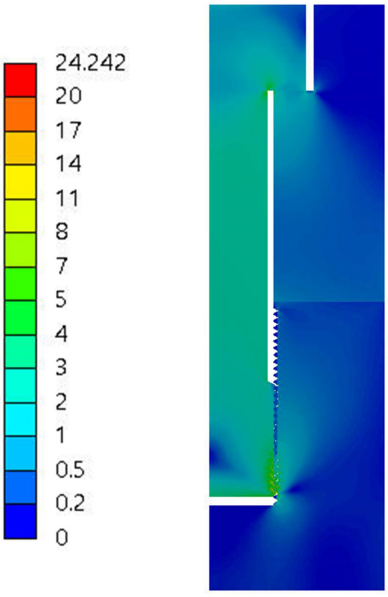

(d) Friction contact : Temperature

Figure 2.3: von Mises Stress plot of the 2D axisymmetric models under various loading conditions

On the other hand, when the same thermal load is applied to the two models (Figures 2.3(c) and 2.3(d)), the computed stress distributions do not match. In particular, the model using the bonded contact at the interface between the steel bolt and the copper component, seems to overpredict the value of the stress. This is due to the differential expansion that the two materials undergo when exposed to high temperature. If a bonded contact is imposed at the interface, the steel and the copper parts are constrained to have the same deformation to satisfy the bonded contact condition thus developing an unrealistically high stress level. In reality, the interaction between the thread of the bolt and the thread of the copper component behave like a frictional contact, thus allowing differential deformation between the parts made of different material with little increase in stress. For this reason, modeling accurately the threads and using frictional contacts instead of bonded contacts as in the second model, is a more accurate technique to evaluate the stresses due to thermal load.

2.3 Hypersonic Wind Tunnel Sensor Analysis - Global Model

The purpose of this work is to design a hypersonic (Mach 6) wind tunnel sensor capable of withstanding high temperature and pressure loads for a substantial amount of time. The assembly is characterized by the use of components made of different materials joined by bolts and screws. At high temperature, the differential thermal expansion that characterizes different metals can become a problem. The results of the preliminary analysis presented in the previous section indicate that to have an accurate prediction of the thermal stresses

in the bolts, it is necessary to accurately model both the threads of the bolts and the joining components, and establish a frictional contact between them to avoid unnatural stress concentration predicted by a finite element model. However, given the complexity of the sensor geometry and the number of bolts and screws that characterize this assembly, this approach is not practical. An enormous amount of time would be required to produce a usable mesh and the resulting high number of elements required to mesh the threads would hinder the solution of the analysis. Instead, the analysis of this structure is approached in two steps: 1) model the bolted junctions without thread and using bonded contacts to compute the global displacements and stresses field (global model), and 2) use a local detailed model of the bolts to accurately evaluate the stresses in the vicinity of the junctions.

2.3.1 Geometry and Mesh - Global Model

The sensor is visualized in Figure 2.4. The structure includes three main parts: 1) a steel mounting bracket, 2) a steel base plate, and 3) a copper flat plate, which houses the pressure and temperature sensors. These parts are assembled using various types of steel bolts and screws.

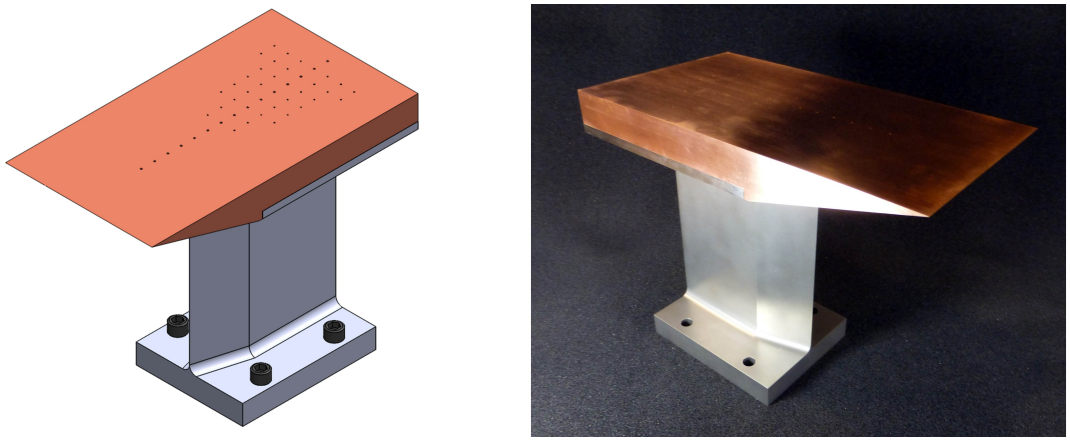

(a) As CAD Geometric model (b) As built structure

Figure 2.4: A hypersonic wing tunnel sensor

The mesh of the global model (no thread on the joints) is shown in Figure 2.5. A combination of structured and unstructured meshes is used to represent as accurately as possible the geometry of the structure. A total of 633,837 solid elements is used to mesh the sensor. Figure 2.6 shows the detail of the mesh of the screws used to connect the component. As discussed above, in the global model the threads are not modeled.

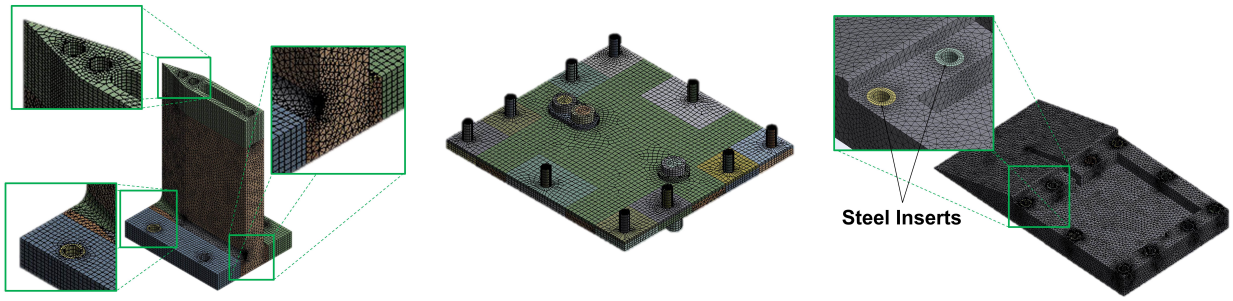

(a) Strut mesh (b) Base plate mesh (c) Flat plate mesh

Figure 2.5: Sensor global mesh

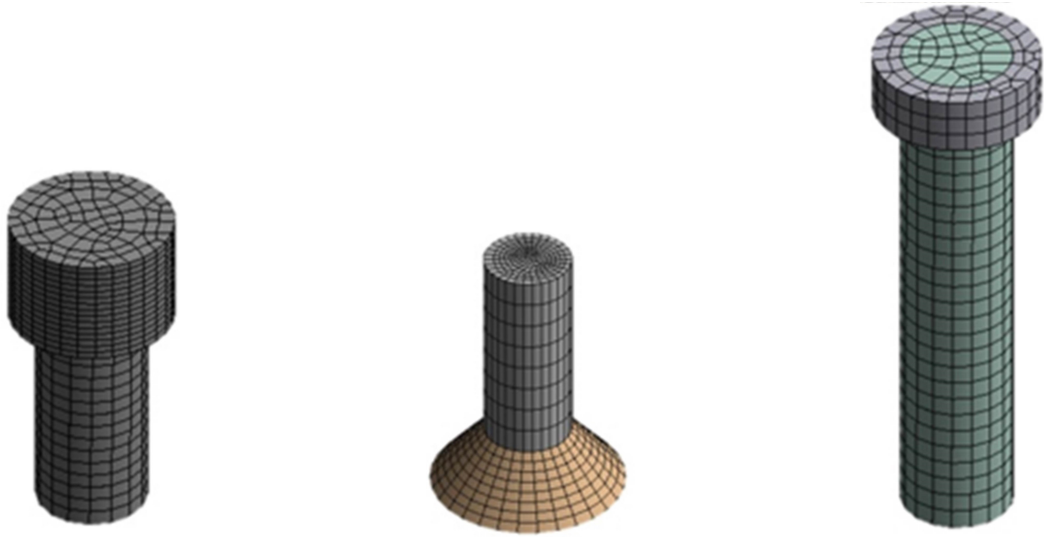

(a) Socket head cap screw

(b) Flat head socket screw

(c) Low head cap screw

Figure 2.6: Screws mesh detail

2.3.2 Materials, Load Conditions, Boundary Conditions - Global Model

Materials

The properties of the materials used to fabricate the sensor components and the screws are listed in Table 2.1.

Load Conditions

The sensor is subjected to mechanical and thermal loads.

- **Mechanical loads:** pressure of 1.627 psi applied to the top surface of the copper plate and pressure of 68.05 psi applied on the bottom surface of the copper plate.
- **Thermal load:** Uniform temperature of 540°F.

Table 2.1: Material properties

Material	C18200 Copper	Steel 17-4 PH H900	Steel ASTM A574	ASTM F835
Component	Flat Plate	Strut Base Plate	Socket Head Screws Low Profile Screws	Flat Head Screws
HR	B65-75	C40	C38-43	C38-43
E (ksi)	18,900	29,000	29,700	29,700
α $(\mu in/in°F)$	9.8	6.4	6.1	6.1
σ_Y $[68\ °F]$ (ksi)	40	200	150-170	140
σ_U $[68\ °F]$ (ksi)	57	210	170-190	160
σ_Y $[540\ °F]$ (ksi)	38	161	112.5-127.5	105
σ_U $[540\ °F]$ (ksi)	53	178	127.5-142.5	105

Boundary Conditions

The screws connecting the strut to the wall of the wind tunnel are fixed to prevent the rigid motion of the structure. The contact between the strut, bottom plate and flat plate are modeled as frictional contacts. Bonded contact conditions are used to connect the head and the shank of the screws to the connecting parts. These type of connection constrain the bonded surfaces to deform together.

2.3.3 Analysis Results - Global Model

A linear thermo-mechanical analysis is carried out leveraging ANSYS software package and the von Mises stress distribution is obtained. The results presented in Figure 2.7 focus on a local high stress region appearing in the copper plate around one of the inserts/screws assembly. Given the results of the preliminary analysis these stresses are most probably over estimated.

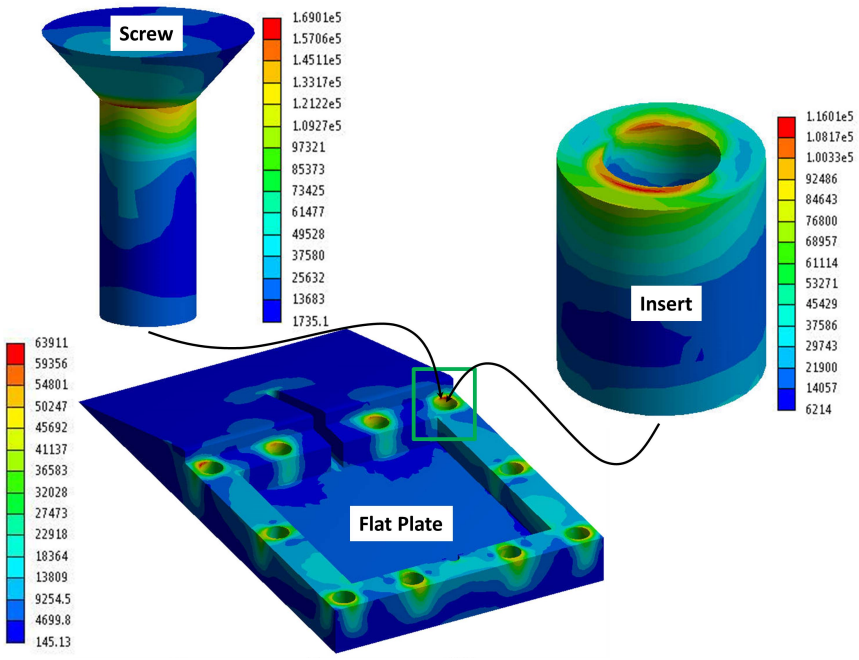

Figure 2.7: von Mises stresses due to thermo-mechanical loading in the flat plate, insert and flat head screw

Moreover, the maximum von Mises stresses computed in the considered components for this model, exceed the ultimate stresses of the materials associated. A more detailed and accurate analysis must be carried out before evaluating the design for its adequecy.

2.4 Hypersonic Wind Tunnel Sensor Analysis - Local Model

The results obtained from the global analysis assuming a bonded contact are not accurate in the vicinity of the threaded joints. Since modeling the threads of every screw in this structure is not practical, the submodeling approach was used to compute a more accurate stress distribution in the regions of interest. The assumption that is used to justify the

validity of this modeling technique is that the deformation field of the structure is not affected by the bonded contacts used to model the screw connection in the global model, if sufficiently far from the bond. Based on this assumption we can isolate a small portion of the model around the screw and accurately model the threads and the insert. The process and the results are presented in the following.

2.4.1 Geometry and Mesh - Local Model

The geometry of the local model is presented in Figure 2.8. A local portion of the structure is simply extracted from the global model and re-meshed to account for the fastener threads.

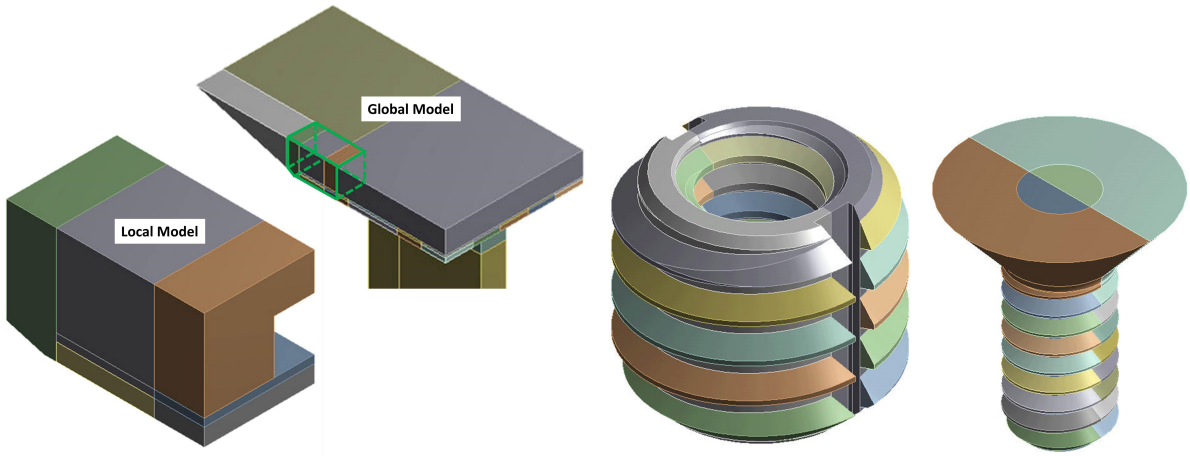

(a) Local model (b) Threaded insert (c) Threaded screw

Figure 2.8: Local model geometry

A refined mesh of the local portion of the model is generated using a mix of structured and unstructured mesh as presented in Figure 2.9.

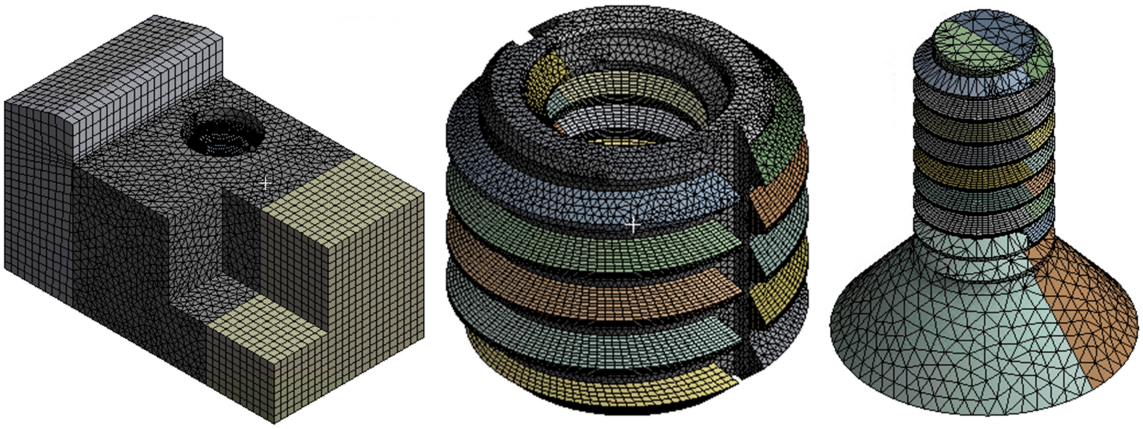

(a) Copper plate portion (b) Threaded insert (c) Threaded screw

Figure 2.9: Local model mesh

Table 2.2: Mesh details

Body	Number of Nodes	Number of Elements
Insert	71546	206605
Bolt	24590	39218
Flat plate	39465	148220
Bottom plate	8020	6624

2.4.2 Materials, Load Conditions, Boundary Conditions - Local Model

Materials

The materials used in the local model are the same as the ones used in the global model.

Load Conditions

The thermo-mechanical load condition used for the local model is the same used for the analysis of the global model.

Boundary Conditions

The boundary conditions enforced on the local model must take into account the displacement field computed in the global model analysis. In fact, the boundaries of the local model are subjected to a prescribed displacement equal to the deformation computed in the global analysis. Since the mesh of the local model and the mesh of the global model are not congruent at the cut boundaries, it is necessary to interpolate the displacements computed in the global analysis onto the nodes of the boundaries of the local model. In addition, the interface between the threads of the different parts are modeled as frictional contacts. The boundary conditions are visualized in Figure 2.10.

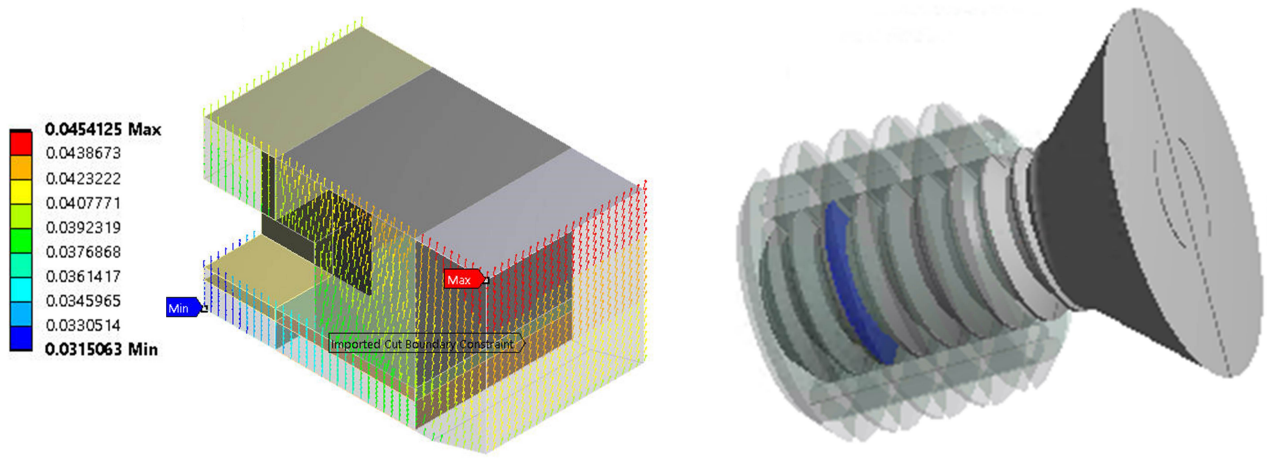

(a) Cut boundary displacements (b) Frictional contacts

Figure 2.10: Boundary conditions

Validation - Local Model

The validation of the local model is achieved by comparing the deformation profile of the free surface of the model with the deformation of the same region of the global model. If the

boundaries of the local model are chosen in the correct fashion, the local effects of the stress concentration at the bounded contacts of the fasteners in the global model are negligible. This means that the displacement field of the free boundaries should not be affected by how the fasteners are modeled. Figure 2.11 shows that the deformation of the free boundary computed with the two models matches exactly, thus confirming that the portion of the structure reproduced in the local model, satisfy the condition of the cut boundaries to be sufficiently distant from the insert and screw interfaces.

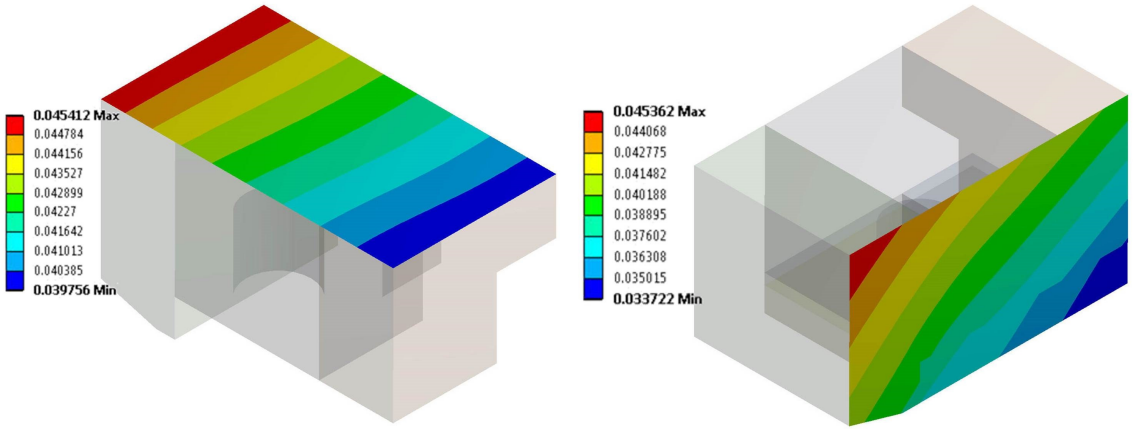

(a) Using a Global model

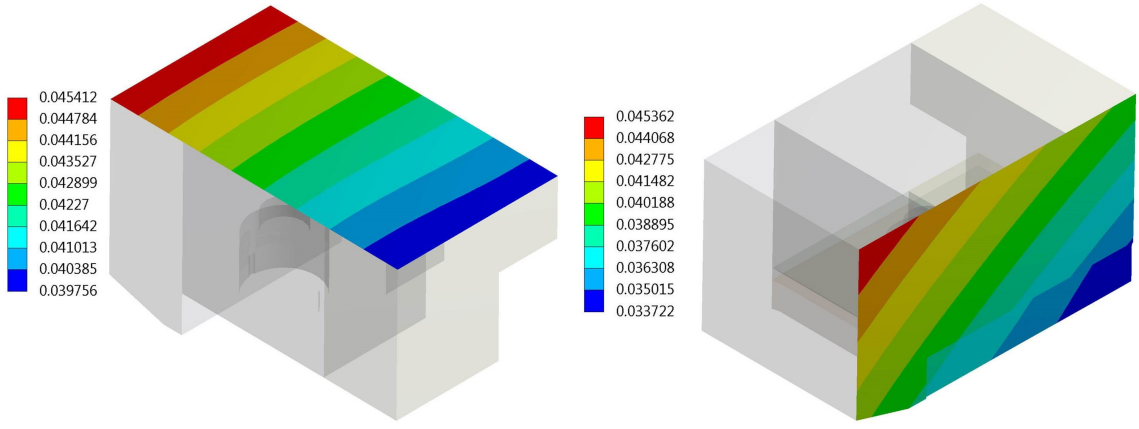

(b) Using a Local model

Figure 2.11: Deformation of the free boundary

2.4.3 Analysis Results - Local Model

A linear thermo-mechanical analysis is carried out using ANSYS software package and the von Mises stress distribution is obtained for the local model. The results are presented in Figure 2.12. The value of the stresses computed in the local model are substantially reduced with respect to the stresses compute with the global model. In particular, the maximum stress in the copper plate is reduced by a factor greater than two. In general, the maximum von Mises stress in the copper plate, threaded insert and flat head screw are all below the ultimate stress of the respective materials. Thus confirming that this particular design can withstand the load conditions for which it was designed. The reduction of the stresses is mainly due to the use of the frictional contacts between the threaded surfaces. This particular contact allows the surfaces of different components to slide with respect to one another thus reliving the stresses induced by the differential thermal deformation of the components. Thus, the two step global/local methodology proposed in this chapter shows the advantage in combining two modeling techniques for the analysis of threaded joints subjected to thermo-mechanical load conditions. Detailed conclusions can be found in Chapter 6

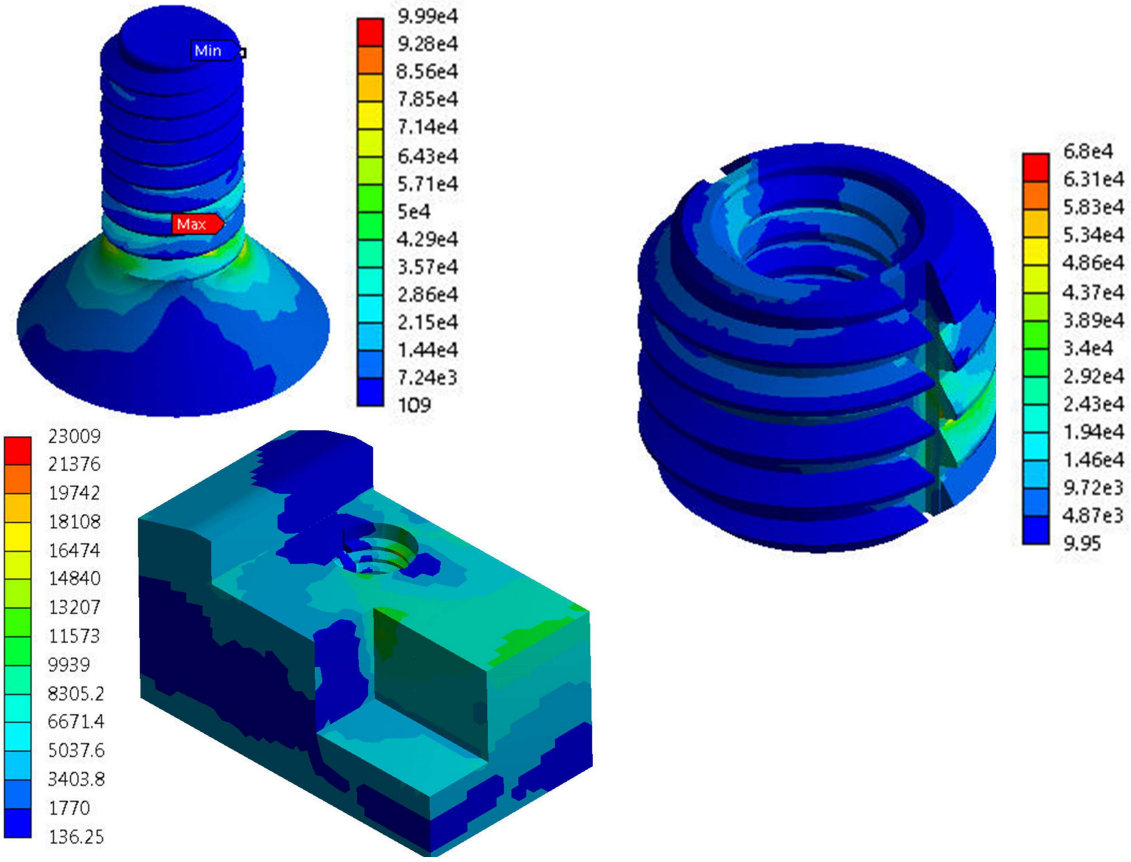

Figure 2.12: von Mises stresses due to thermo-mechanical loading in the local model, insert and flat head screw

Chapter 3

Analysis of Stiffened Laminated Composite Plates with Cutouts Using Isogeometric Method

3.1 Introduction

In this chapter, thermal buckling analysis of stiffened laminated composite plates with complicated cutouts is presented. The plate and the stiffener are subjected to a uniform rise in temperature for various boundary conditions. The stiffness matrices and thermal force vector are derived using the first-order shear deformation theory (FSDT). Cutouts are modeled using multiple NURBS patches generated by creating a ruled surface between two curves. First, the present method is verified by comparing it against results from available literature. The effect on the critical buckling temperature due to variations in width-to-thickness ratio, fiber orientation and boundary conditions are then analyzed and useful conclusions are summarized from the results.

3.2 Mathematical foundations

3.2.1 Laminated composite panel

According to the first-order shear deformation theory (FSDT) the displacement field is considered as the first-order Taylor series expansion of the mid-plane displacement variables with respect to plate thickness as follows: Consider a stiffened composite plate with a circular cutout as shown in Figure 3.1. The mid-plane of the panel O_{xy} the global coordinate system. The plate is assumed to have a uniform thickness with no plydrops. Let u be the displacements in the x-axis and v be the in-plane displacements along the y-axis.Let w be the transverse deflection along the z-axis.

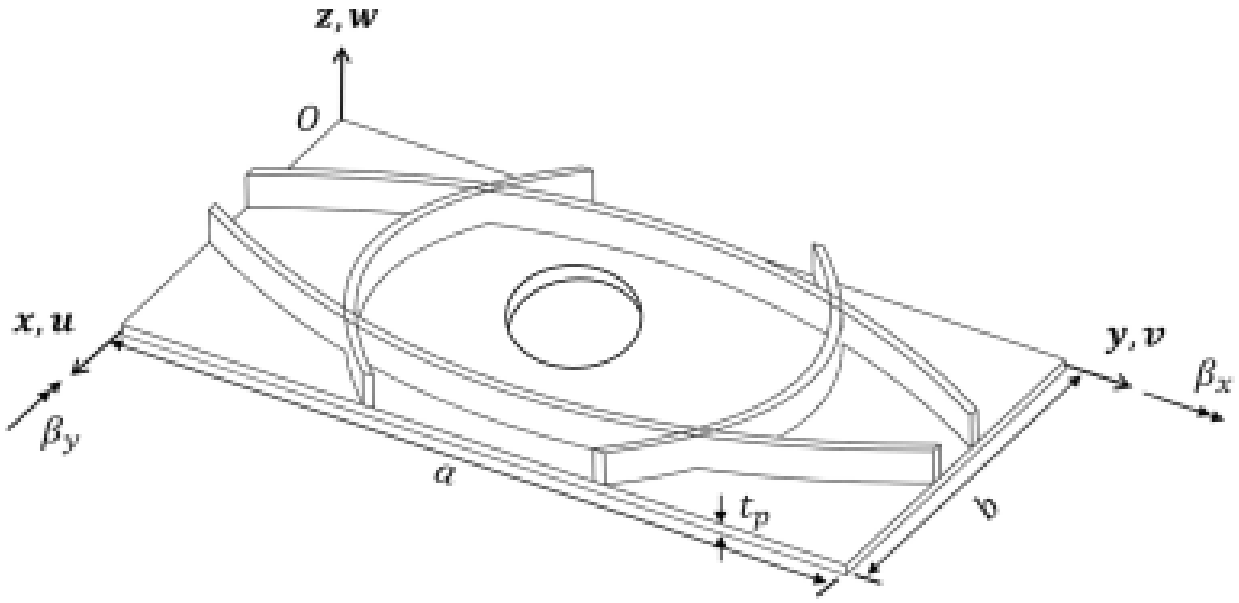

Figure 3.1: Geometry and nomenclature of a stiffened composite panel with a central cutout. Redrawn and modified from [1]

Let β_y and β_x be rotation components of the panel around the x- and y-axes, respectively.

The displacement components of the panel can now be written as,

$$\begin{aligned} u\left(x,y,z,t\right) &= u_0\left(x,y,z,t\right) + z\beta_x\left(x,y,t\right) \\ v\left(x,y,z,t\right) &= v_0\left(x,y,z,t\right) + z\beta_y\left(x,y,t\right) \\ w\left(x,y,z,t\right) &= w_0\left(x,y,z,t\right) \end{aligned} \tag{3.1}$$

The plate strain energy U_p can be written as,

$$U_p = \frac{1}{2}\int_{\Omega}\int \boldsymbol{\varepsilon}_{\mathbf{p}}^{\mathbf{L}\mathrm{T}}\mathbf{D}_{\mathbf{p}}\boldsymbol{\varepsilon}_{\mathbf{p}}^{\mathbf{L}}\mathrm{d}\Omega \tag{3.2}$$

Where, $\mathbf{D}_p$ depends on the material property, stacking sequence, ply orientation and thickness of the plate. Derivation of $\mathbf{D}_p$ is explained in Section 3.2.2. The generalized strains $\boldsymbol{\varepsilon}_{\mathbf{p}}^{\mathbf{L}}$ can be expressed in terms of the generalized displacements $\mathbf{u_p}$ of the panel as,

$$\boldsymbol{\varepsilon}_{\mathbf{p}}^{\mathbf{L}} = \begin{Bmatrix} \varepsilon_x^0 \\ \varepsilon_y^0 \\ \gamma_{xy}^0 \\ \kappa_x^0 \\ \kappa_y^0 \\ \kappa_{xy}^0 \\ \gamma_{xz}^0 \\ \gamma_{yz}^0 \end{Bmatrix} = \begin{bmatrix} \frac{\partial}{\partial x} & 0 & 0 & 0 & 0 & 0 \\ 0 & \frac{\partial}{\partial x} & 0 & 0 & 0 & 0 \\ \frac{\partial}{\partial x} & \frac{\partial}{\partial x} & 0 & 0 & 0 & 0 \\ 0 & 0 & 0 & 0 & \frac{\partial}{\partial x} & 0 \\ 0 & 0 & 0 & 0 & 0 & \frac{\partial}{\partial x} \\ 0 & 0 & 0 & 0 & \frac{\partial}{\partial x} & \frac{\partial}{\partial x} \\ 0 & 0 & 0 & \frac{\partial}{\partial x} & 1 & 0 \\ 0 & 0 & 0 & \frac{\partial}{\partial x} & 0 & 1 \end{bmatrix} \begin{Bmatrix} u_0 \\ v_0 \\ w_0 \\ \beta_x \\ \beta_y \end{Bmatrix} = \mathbf{B_p u_p} \tag{3.3}$$

The strain energy of the composite panel U_p is,

$$U_p = \frac{1}{2}\iint_{\Omega} \mathbf{u_p}^T \mathbf{B_p}^T \mathbf{D_p} \mathbf{B_p} \mathbf{u_p} d\Omega \tag{3.4}$$

For thermal bucking analysis, the geometric stiffness due to inplane stress resultants is considered. Thus, the potential W_p of the panel due to in-plane stress vector $\overline{\sigma}_{\mathbf{p}} = \begin{pmatrix} \sigma_x^0 & \sigma_y^0 & \tau_{xy}^0 & 0 & 0 \end{pmatrix}$ is,

$$W_p = \frac{1}{2}\int_{\Omega}\int \overline{\sigma}_{\mathbf{p}} \boldsymbol{\varepsilon}_{\mathbf{p}}^{\mathbf{NL}} \mathrm{d}\Omega \tag{3.5}$$

The nonlinear strain factor matrix is:

$$\left[\mathbf{B}_p^{NL}\right] = \begin{bmatrix} 0 & 0 & \frac{\partial}{\partial x} & 0 & 0 \\ 0 & 0 & \frac{\partial}{\partial y} & 0 & 0 \\ 0 & 0 & 0 & \frac{\partial}{\partial x} & 0 \\ 0 & 0 & 0 & \frac{\partial}{\partial y} & 0 \\ 0 & 0 & 0 & 0 & \frac{\partial}{\partial x} \\ 0 & 0 & 0 & 0 & \frac{\partial}{\partial y} \end{bmatrix} \tag{3.6}$$

The in-plane stress matrix can be written as:

$$\boldsymbol{\sigma}_{\mathbf{p}} = \begin{pmatrix} t\sigma_y^0 & t\tau_{xy}^0 & 0 & 0 & 0 & 0 \\ t\tau_{xy}^0 & t\sigma_y^0 & 0 & 0 & 0 & 0 \\ 0 & 0 & \frac{t^3}{12}\sigma_y^0 & \frac{t^3}{12}\tau_{xy}^0 & 0 & 0 \\ 0 & 0 & \frac{t^3}{12}\tau_{xy}^0 & \frac{t^3}{12}\sigma_y^0 & 0 & 0 \\ 0 & 0 & 0 & 0 & \frac{t^3}{12}\sigma_y^0 & \frac{t^3}{12}\tau_{xy}^0 \\ 0 & 0 & 0 & 0 & \frac{t^3}{12}\tau_{xy}^0 & \frac{t^3}{12}\sigma_y^0 \end{pmatrix}, \tag{3.7}$$

Hence, Equation 3.5 can be written as

$$W_p = \frac{1}{2}\int_{\Omega}\int \mathbf{u_p^T B_p^{NLT}} \sigma_{\mathbf{p}} \mathbf{B_p^{NL}} \mathbf{u_p} \mathrm{d}\Omega \tag{3.8}$$

3.2.2 Orthotropic layers

The constitutive equation in the local coordinate system for the k^{th} orthotropic elastic laminate can be derived from Hooke's law as

$$\begin{Bmatrix} \sigma_1 \\ \sigma_2 \\ \tau_{12} \\ \sigma_3 \\ \tau_{31} \\ \tau_{23} \end{Bmatrix}^{(k)} = \begin{bmatrix} Q_{11} & Q_{12} & 0 & 0 & 0 & 0 \\ Q_{21} & Q_{22} & 0 & 0 & 0 & 0 \\ 0 & 0 & Q_{66} & 0 & 0 & 0 \\ Q_{31} & Q_{32} & 0 & Q_{33} & 0 & 0 \\ 0 & 0 & 0 & 0 & Q_{55} & 0 \\ 0 & 0 & 0 & 0 & 0 & Q_{44} \end{bmatrix}^{(k)} \begin{Bmatrix} \varepsilon_1 - \alpha_1 T \\ \varepsilon_2 - \alpha_2 T \\ \gamma_{12} \\ \varepsilon_3 - \alpha_3 T \\ \gamma_{31} \\ \gamma_{23} \end{Bmatrix}^{(k)} \tag{3.9}$$

where Q_{ij} are the elastic coefficients in the material coordinate system, T is the temperature change and α_i is the thermal coefficient of expansion in the principal i^{th}-direction. The transformed material constants are expressed as,

$$\begin{Bmatrix} \overline{Q}_{11} \\ \overline{Q}_{12} \\ \overline{Q}_{22} \\ \overline{Q}_{16} \\ \overline{Q}_{26} \\ \overline{Q}_{66} \end{Bmatrix} = \begin{bmatrix} c^4 & 2c^2s^2 & s^4 & 4c^2s^2 \\ c^2s^2 & c^4+s^4 & c^2s^2 & -4c^2s^2 \\ s^4 & 2c^2s^2 & c^4 & 4c^2s^2 \\ c^3s & cs(s^2-c^2) & -cs^3 & 2cs(s^2-c^2) \\ cs^3 & cs(c^2-s^2) & -c^3s & 2cs(c^2-s^2) \\ c^2s^2 & -2c^2s^2 & c^2s^2 & (c^2-s^2)^2 \end{bmatrix} \begin{Bmatrix} Q_{11} \\ Q_{12} \\ Q_{22} \\ Q_{66} \end{Bmatrix}, \tag{3.10}$$

$$\begin{bmatrix} \overline{Q}_{44} & \overline{Q}_{13} \\ \overline{Q}_{45} & -\overline{Q}_{36} \\ \overline{Q}_{55} & \overline{Q}_{23} \end{bmatrix} = \begin{bmatrix} c^2 & s^2 \\ -cs & cs \\ s^2 & c^2 \end{bmatrix} \begin{bmatrix} Q_{44} & Q_{13} \\ Q_{55} & Q_{23} \end{bmatrix}, \; \overline{Q}_{33} = Q_{33} \tag{3.11}$$

$$\begin{Bmatrix} \alpha_x \\ \alpha_y \\ \alpha_{xy} \end{Bmatrix} = \begin{bmatrix} c^2 & s^2 \\ s^2 & c^2 \\ 2cs & -2cs \end{bmatrix} \begin{Bmatrix} \alpha_1 \\ \alpha_2 \end{Bmatrix}, \; \alpha_z = \alpha_3 \tag{3.12}$$

where $c = \cos\theta$ and $s = \sin\theta$.

Using this, $\mathbf{D}_p$ can now be written as

$$\mathbf{D}_p = \begin{bmatrix} \mathbf{A} & \mathbf{B} & \mathbf{0} \\ \mathbf{B} & \mathbf{D} & \mathbf{0} \\ \mathbf{0} & \mathbf{0} & \mathbf{A}^{\mathrm{s}} \end{bmatrix} \tag{3.13}$$

where,

$$(A_{ij},B_{ij},D_{ij}) = \int_{-h/2}^{h/2} \overline{Q}_{ij}(1,z,z^2)\mathrm{d}z, \quad A_{ij}^{\mathrm{s}} = K \int_{-h/2}^{h/2} \overline{Q}_{ij}\mathrm{d}z \tag{3.14}$$

where A_{ij}, B_{ij} and D_{ij} are valid for $i, j = 1, 2, 6$, and A_{ij}^{s} for $i, j = 4, 5$ according to the Voigt notation. K denotes the transverse shear correction coefficient. A value of $K = 5/6$ was used for the analyses.

3.2.3 Curvilinear stiffener

Consider a stiffener attached to a plate as shown in the figure below.

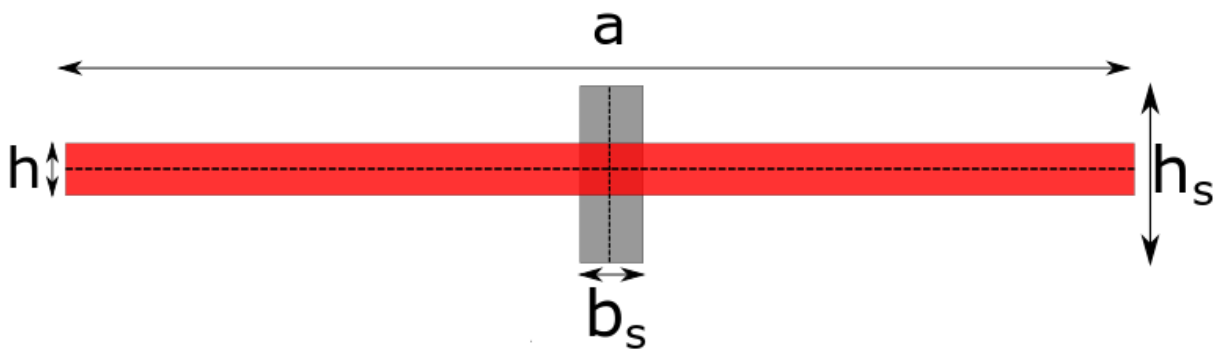

Figure 3.2: Composite plate (red) stiffened by a rectangular stiffener (gray)

The width and height of the rectangular stiffener are given as b_s and h_s, respectively. Details of the coordinate system and nomenclature can be found in [1]. The stiffener is modeled using 1D 2^{nd} order NURBS basis. The stiffener is modeled using the Timoshenko Beam theory.

The coordinates any point on the stiffener can be calculated using :

$$\mathbf{r_s} = \sum_{i=1}^{k} R_i(\varsigma)\mathbf{r_s}_i, \tag{3.15}$$

where $R_i(\varsigma)$ is the basis function corresponding to the i^{th} control point and m is the number of the control points in one element.

Let $\mathbf{u}_s = [u_t, v_n, w_b, \beta_t, \beta_n]^T$ be the degrees of freedom of the stiffener. The displacement of stiffener can then be written as:

$$\mathbf{u_s} = \sum_{i=1}^{m} R_i(\varsigma)\mathbf{u_s}_i, \tag{3.16}$$

where $\mathbf{u}_{si}$ is the displacement vector of the i^{th} control point.

The length of the stiffener is [97]:

$$\Gamma = \int_{\Gamma} d\Gamma = \int_{-1}^{1} J \mathrm{d}\varsigma, \tag{3.17}$$

where

$$J = \| \mathbf{r}_{\mathbf{s}}^{'} \| = \| \frac{d\mathbf{r}_{\mathbf{s}}}{d\varsigma} \| \tag{3.18}$$

is the Jacobian.

The curvature of stiffener can be written as:

$$\frac{1}{R} = \frac{\| \mathbf{r}^{'} \times \mathbf{r}^{''} \|}{\| \mathbf{r}^{'} \|^3} \tag{3.19}$$

The stiffener strain energy U_s is written as:

$$U_s = \frac{1}{2} \int_{\Gamma} \varepsilon_{\mathbf{s}}^{\mathbf{LT}} \mathbf{D}_{\mathbf{s}} \varepsilon_{\mathbf{s}}^{\mathbf{L}} \mathrm{d}\Gamma \tag{3.20}$$

The strain displacement relation of the composite stiffener is [98],

$$\varepsilon_{\mathbf{s}} = \begin{Bmatrix} \varepsilon_t^0 \\ \gamma_n^0 \\ \gamma_b^0 \\ \kappa_t^0 \\ \kappa_n^0 \end{Bmatrix} = \begin{bmatrix} \frac{d}{dt} & \frac{1}{R} & 0 & 0 & 0 \\ -\frac{1}{R} & \frac{d}{dt} & 0 & 0 & 0 \\ 0 & 0 & \frac{d}{dt} & 1 & 0 \\ 0 & 0 & 0 & \frac{d}{dt} & \frac{1}{R} \\ 0 & 0 & 0 & -\frac{1}{R} & \frac{d}{dt} \end{bmatrix} \begin{Bmatrix} u_t \\ v_n \\ w_b \\ \beta_t \\ \beta_n \end{Bmatrix} = \mathbf{B_s u_s} \tag{3.21}$$

where $\frac{1}{R}$ is the curvature of the stiffener and is evaluated at each integration point. Substituting Equation 3.20 into Equation 3.21 we get,

$$U_s = \frac{1}{2} \int_{\Gamma} \mathbf{u_s}^{\mathrm{T}} \mathbf{B_s}^{\mathrm{T}} \mathbf{D_s} \mathbf{B_s^L} \mathbf{u_s} \mathrm{d}\Gamma, \tag{3.22}$$

where $\mathbf{u}_s$ is the stiffener displacement in the local coordinate system and Γ is the arc length domain of the curvilinear stiffener.

The constitutive relation that relates strains and curvatures to the stresses in the stiffener is:

$$\sigma_{\mathbf{s}} = \mathbf{D_s} \boldsymbol{\varepsilon}_{\mathbf{s}}^{\mathbf{L}} = \begin{pmatrix} E_s A & 0 & 0 & E_s A e & 0 \\ 0 & G_s A_n & 0 & 0 & G_s A_n e \\ 0 & 0 & G_s A_b e & 0 & 0 \\ E_s A e & 0 & 0 & E_s I_n & 0 \\ 0 & G_s A_n e & 0 & 0 & G_s J_t \end{pmatrix} \begin{pmatrix} \varepsilon_t \\ \gamma_b \\ \gamma_n \\ \kappa_t \\ \kappa_n \end{pmatrix}, \tag{3.23}$$

where E_s is Young's modulus, $A = b_s h_s$ is the cross-sectional area of the stiffener,$G_s = \frac{E_s}{2(1+\nu)}$ is the shear modulus, e is the eccentricity. $A_n = K_n$A and $A_b = K_b A$ are the shearing areas in the directions n and b, respectively, b_s and h_s are the width and the height of the stiffener respectively, K_n and K_b are the shear correction factors in the n and b directions respectively. I_n and I_b are the second moments of areas A_n and A_b, respectively. J_t is the torsion constant of the rectangular stiffener.

$$W_s = \frac{1}{2}\int_\Gamma \mathbf{u_s}^{\mathrm{T}} \mathbf{B_s^{NLT}} \sigma_{\mathbf{s}} \mathbf{B_s^{NL}} \mathbf{u_s} \mathrm{d}\Gamma. \tag{3.24}$$

$$\mathbf{B_s^{NL}} = \begin{pmatrix} \frac{1}{J}\frac{\partial}{\partial \varsigma} & 0 & 0 \\ 0 & \frac{1}{J}\frac{\partial}{\partial \varsigma} & \frac{1}{R} \\ 0 & -\frac{1}{R} & \frac{1}{J}\frac{\partial}{\partial \varsigma} \end{pmatrix}. \tag{3.25}$$

The matrix caused by in-plane stress is written as:

$$\boldsymbol{\sigma_s} = \begin{pmatrix} A\sigma_t & 0 & 0 \\ 0 & (I_n + e^2 A)\sigma_t & 0 \\ 0 & 0 & (I_n + e^2 A)\sigma_t \end{pmatrix}, \tag{3.26}$$

Where σ_{tt} is the tangential stress, and σ_{tn} and σ_{tb} are the the shear stresses. The nonlinear term of the in-plane normal strain described in the local curvilinear coordinate system t_{nb} is [1],

$$\varepsilon_t^{NL} = \frac{1}{2}\left(\frac{\mathrm{d}w_b}{\mathrm{d}t}\right)^2 + \frac{z^2}{2}\left(\frac{\mathrm{d}\beta_t}{\mathrm{d}t} + \frac{\beta_n}{R}\right)^2 + \frac{z^2}{2}\left(\frac{\mathrm{d}\beta_n}{\mathrm{d}t} - \frac{\beta_t}{R}\right)^2 \tag{3.27}$$

where axial stress is:

$$\sigma_{tt} = \frac{\sigma_x^0 + \sigma_y^0}{2} + \frac{\sigma_x^0 - \sigma_y^0}{2}\cos 2\alpha + \sigma_{xy}^0 \sin 2\alpha \tag{3.28}$$

where α is the angle between the t-direction and x axis.

Before building the linear system of equations of the stiffened plate, the degrees of freedom of the plate and curvilinear stiffener should be unified. Detailed steps to achieve this are as follows:

- First, the plate and the stiffener are meshed independently and the location of the stiffener control points is identified. Take Figure 5.2 for instance, where the control point A belongs to the plate element k.

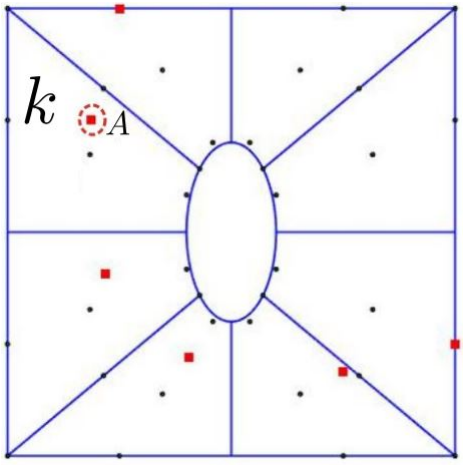

Figure 3.3: Mesh plot of the curvilinearly stiffened plate in the physical space.

We can compute the natural coordinates $(\bar{\xi}, \bar{\eta})$ of the stiffener control point in the plate element by solving Equation 3.29 since the stiffener and the plate control points are known.

$$\mathbf{r_s} \mid_A = \sum_{j=1}^{4} R_j(\bar{\xi}_A, \bar{\eta}_A)\mathbf{x_{p}}_j \mid_k . \tag{3.29}$$

- Since the natural coordinates are not obtained, the displacement of the stiffener is:

$$\mathbf{u_s} \mid_A = \sum_{j=1}^{4} R_j(\bar{\xi}_A, \bar{\eta}_A)\mathbf{u_{p}}_j \mid_k . \tag{3.30}$$

- The displacements of any points in the stiffener element can be computed as:

$$\mathbf{u_{sg}} = \sum_{j=A} R_j(\varsigma)\mathbf{u_{s}}_j. \tag{3.31}$$

- Then, substituting Equation 3.30 into Equation 3.31 results in the following equation:

$$\mathbf{u_{sg}} = \sum_{j=A} R_j(\varsigma) \sum_{i=1}^{4} R_i(\bar{\xi}_j, \bar{\eta}_j)\mathbf{u_{p}}_i \mid_k \tag{3.32}$$

- Rewriting the displacement approximations in a matrix form,

$$\mathbf{u_{sg}} = \mathbf{N}_{ps}\mathbf{u_p} \mid_k . \tag{3.33}$$

- Now the displacement $\mathbf{u}_{sg}$ are described in the global coordinate system. Hence the

stiffener displacements should be transformed to the local curvilinear coordinate system. The transformation matrix is:

$$\mathbf{T} = \begin{pmatrix} \cos\alpha & \sin\alpha & 0 & 0 & 0 \\ -\sin\alpha & \cos\alpha & 0 & 0 & 0 \\ 0 & 0 & 1 & 0 & 0 \\ 0 & 0 & 0 & \cos\alpha & \sin\alpha \\ 0 & 0 & 0 & -\sin\alpha & \cos\alpha \end{pmatrix}, \tag{3.34}$$

where α is the angle between t and the x axes and, whose value is calculated at each integration point.

$$\alpha = tan^{-1}\Big(\frac{y'}{x'}\Big) \tag{3.35}$$

The prime ' refers to the first derivative with respect to the stiffener arc length, $d()/d\Gamma$.

Finally, the translation of the degrees of freedom from stiffener to plate is complete. Hence, the stiffener strain energy the energy caused by in-plane stresses can be written as,

$$U_s = \frac{1}{2}\int \mathbf{u_p^T N_{ps}^T T^T B_s^{LT} D_s B_s^L T N_{ps} u_p} \mathrm{d}\Gamma, \tag{3.36}$$

$$W_s = \frac{1}{2}\int_\Gamma \mathbf{u_p^T N_{ps}^T T^T B_s^{NLT} \boldsymbol{\sigma}_s B_s^{NL} T N_{ps} u_p} \mathrm{d}\Gamma. \tag{3.37}$$

Hamilton's principle can now be used in deriving the weak form of the governing equation.

$$\int_{t_1}^{t_2} [(\delta U_p + \delta U_s) - (\delta W_p + \delta W_s)] \mathrm{d}t = 0, \tag{3.38}$$

where t_1 and t_2 are the initial and final times, respectively.

$$\int_{t_1}^{t_2} \left[\begin{array}{c} \int\int_{\Omega} \delta \mathbf{u_p^T} (\mathbf{B_p^{LT}} \mathbf{D_p} \mathbf{B_p^L}) \mathbf{u_p} \mathrm{d}\Omega + \int_{\Gamma} \delta \mathbf{u_p^T} (\mathbf{N_{ps}^T} \mathbf{T^T} \mathbf{B_s^{LT}} \mathbf{D_s} \mathbf{B_s^L} \mathbf{T} \mathbf{N_{ps}}) \mathbf{u_p} \mathrm{d}\Gamma \\ - \int\int_{\Omega} \delta \mathbf{u_p^T} \mathbf{B_p^{NLT}} \sigma_{\mathbf{p}} \mathbf{B_p^{NL}} \mathbf{u_p} \mathrm{d}\Omega - \int_{\Gamma} \delta \mathbf{u_p^T} \mathbf{N_{ps}^T} \mathbf{T^T} \mathbf{B_s^{NLT}} \boldsymbol{\sigma}_{\mathbf{s}} \mathbf{B_s^{NL}} \mathbf{T} \mathbf{N_{ps}} \mathbf{u_p} \mathrm{d}\Gamma \end{array} \right] \mathrm{d}t = 0. \tag{3.39}$$

3.2.4 Isogeometric analysis

The concept of IGA is to use the same basis functions to generate CAD and to discretize the solution to the boundary value problem. This isoparametric formulation in combination with the properties of NURBS basis functions allows the geometry to be modeled exactly from the coarsest level of refinement, and maintains this exact representation as the mesh is refined. The elements are constructed by a knot span which is an array of non-decreasing sequence of parameter values [35]. NURBS basis functions are used to construct the exact geometry, as well as the corresponding solution space. In this section, we present a primer on NURBS and also some basic formulations of IGA. Knot vectors can be defined as:

$$\Xi = \{\xi_1, \xi_2, ..., \xi_{n+p+1}\} \tag{3.40}$$

B-spline basis functions are defined recursively starting with piecewise constants $p = 0$

$$N_i^0(\xi) = \begin{cases} 1 & if \quad \xi_i < \xi < \xi_{i+1} \\ 0 & \text{otherwise} \end{cases} \tag{3.41}$$

For higher values like $p = 0, 1, 2...$ the basis functions are defined using a recursion relation

$$N_i^p(\xi) = \frac{\xi - \xi_i}{\xi_{i+p} - \xi_i} N_i^{p-1}(\xi) + \frac{\xi_{i+p+1} - \xi}{\xi_{i+p+1} - \xi_{i+1}} N_{i+1}^{p-1}(\xi) \tag{3.42}$$

where ξ_1 is the i^{th} knot, n is the number of basis functions and p is the polynomial order.

We denote Non-uniform Rational B-splines (NURBS) functions expressed as

$$R_{i,p}(\xi) = \frac{N_{i,p}(\xi) w_i}{\sum_{j=1}^{n} N_{j,p}(\xi) w_j} \tag{3.43}$$

Where w_i is the weight corresponding to the i^{th} control point. For a 2-dimensional surface, the basis functions are expressed as:

$$R_{i,j}^{p,q}(\xi,\eta) = \frac{N_{i,p}(\xi) N_{j,q}(\eta) w_{i,j}}{\sum_{i=1}^{n} \sum_{j=1}^{m} N_{i,p}(\xi) N_{j,q}(\eta) w_{i,j}} = \frac{N_{i,p}(\xi) N_{j,q}(\eta) w_{i,j}}{W(\xi,\eta)} \tag{3.44}$$

The 2D surface is generated using the basis functions, $R_{i,j}$, and the control points $P_{i,j}$

$$\boldsymbol{S}(\xi,\eta) = \sum_{i=1}^{n} \sum_{j=1}^{m} R_{i,j}^{p,q}(\xi,\eta) \boldsymbol{P}_{i,j}, \tag{3.45}$$

Further details can be found in [35] and [44].

3.2.5 Achieving displacement compatibility

To build the stiffened plate equations, the degrees of freedom of the stiffener need to be transformed to that of the plate. This was achieved efficiently by Shi et al.[99]. Their method allowed the stiffener to be placed anywhere in the plate domain and did not have to share nodes with the plate. This was achieved by first identifying which element a particular node of the stiffener belongs to and subsequently, calculating the coordinates of the node in the shape element space. This is computationally expensive as one has to traverse through elements for potential stiffener node locations. However, in isogeometric analysis, the basis functions are defined in the parametric domain (UV space, see Figure 3.4). This feature is leveraged to develop an inverse point projection algorithm using Newton's method since every point in the physical space has a corresponding point in the parametric space as shown in Figure 3.4. Projecting coordinates from the parametric space of a NURBS patch to the physical space is an easy task which can be performed using the NURBS formulation. However, projecting the coordinates from the physical space to the parametric space is not that straightforward. This problem can be mathematically described as finding the parametric coordinate $\xi_{\mathbf{p}}(\mathbf{P})$ such that the distance between the physical coordinate $\mathbf{x}(\mathbf{P})$ of the point under consideration $\mathbf{P}$ and the NURBS projection $\mathbf{S}(\xi_{\mathbf{p}}(\mathbf{P}))$ is minimized, i.e.

$$\xi_{\mathbf{p}}(\mathbf{P}) \parallel \mathbf{S}(\xi_{\mathbf{p}}(\mathbf{P})) - \mathbf{x}(\mathbf{P}) \parallel_{\mathbf{2}} \leq \parallel \mathbf{S}\{\xi\} - \mathbf{x}(\mathbf{P}) \parallel_{\mathbf{2}} \ \forall\, \xi, \xi_{\mathbf{p}} \ \in \ \Omega^{\mathbf{2}} \tag{3.46}$$

In their book, Piegl and Tiller [100] propose a nonlinear iteration technique based on the

popular Newton's method to find an optimal value for $\xi_{\mathbf{p}}$. This method works really well for physical points on the patch (point inversion) as well as off the target patch (point projection). However, such an iterative method necessitates the evaluation of NURBS basis functions and its derivatives for the point under consideration during each iteration. When the problem involves a lot of points to project, such a method can become computationally expensive. Therefore, to improve the computational efficiency it is important to choose the accuracy (tolerance) and the grid size for a point projection algorithm.

This issue can be solved to a great extent by choosing bounding boxes in order to compute the lower and the upper distance bounds. This reduces the candidate pair numbers to a large scale and makes the method more efficient and faster. The initial value of $\xi_{\mathbf{p}}$ greatly influences the number of iterations taken to converge and thus the numerical cost associated with this method. Hence, with an inappropriate initial value, there are even chances that the method wouldn't converge at all. The local support of the basis functions that are associated with a control point can be used to determine the initial value while projection control points onto the NURBS patch boundary surface. The knot vectors associated with these basis functions can exactly define the upper and lower bounds. Hence, the median coordinates in the parametric space can be determined and for patches with moderately high polynomial degrees of the basis functions an initial guess can be determined.

This bound using the functions' support are then used as the projection range. The remaining points in the parametric space can be excluded giving rise to an increase in computational efficiency. This way, the coordinates of a particular stiffener control point can be mapped to

the parametric space and the corresponding value of basis function at that point can be used for displacement mapping. The algorithm was implemented using an intial guess, a specified tolerance value and a maximum number of iterations to compute the point in the parametric space. It was seen that convergence was always achieved in less than 10 iterations. The MATLAB script to implement this process can be found in Section 6.1.

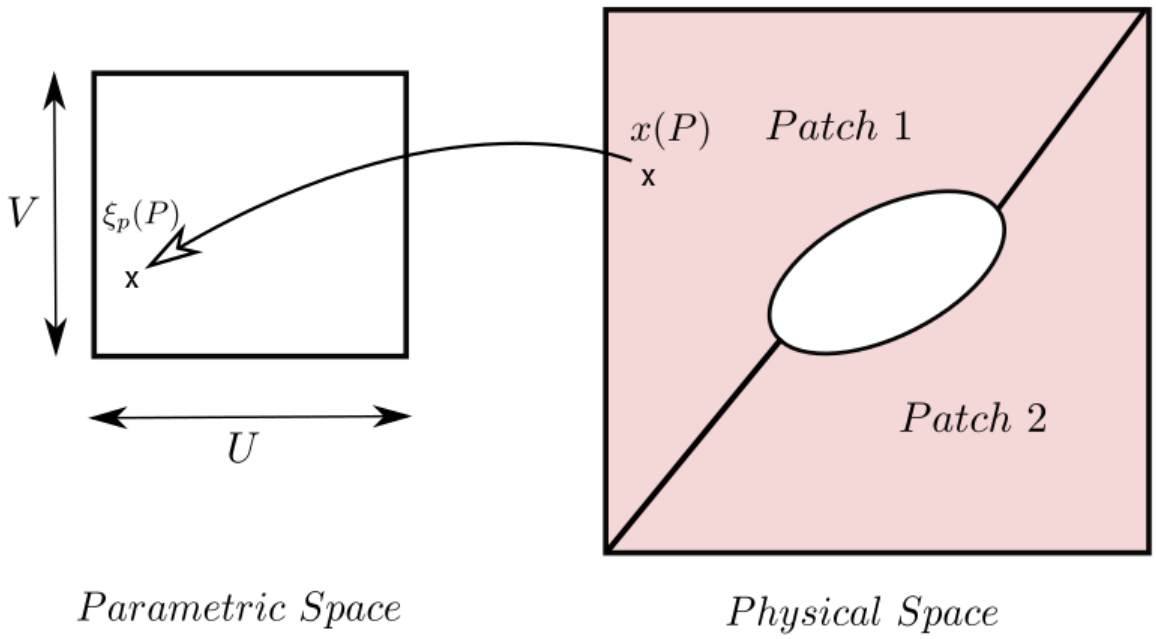

Figure 3.4: Mapping from physical space to parametric space

Figure 3.5 shows one such stiffener control point (circled) which is a part of the NURBS patch highlighted in green. The global coordinates of this control point are $(-0.3750, 0)$ and the corresponding parametric coordinates are $(0.3810, 0.6081)$.

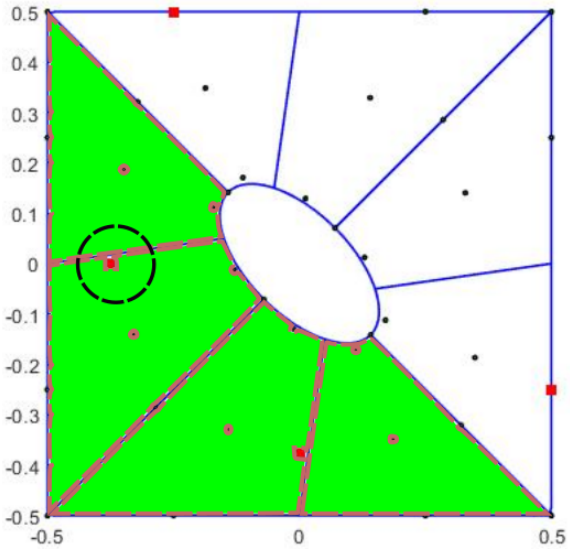

Figure 3.5: Stiffener control point (circled) and the plate mesh formed using patch 1 (green) and patch 2(white)

Table 3.1: Global and parametric coordinates of the stiffener control point

Global Coordinates		Parametric Coordinates	
x	y	U	V
−0.3750	0	0.3810	0.6081

3.2.6 Multipatch modeling of plate geometry

Sometimes the stiffened panels have internal cutouts and this poses a challenge in the modeling aspect. When the geometry of the cutout is quite complicated, describing the geometry using multiple patches is convenient. A NURBS patch defines a subdomain and the knot spans subdivide the subdomain into elements. In this case, first the inner and the outer profile of such a panel is constructed using 1D NURBS curves as shown in Figure 3.6. The outer curve is constructed using the knot vector [0, 0, 0, .25, .5, .5, .75, 1, 1, 1] and the inner curve using the knot vector [0, 0, 0, .5, .5, 1, 1, 1]

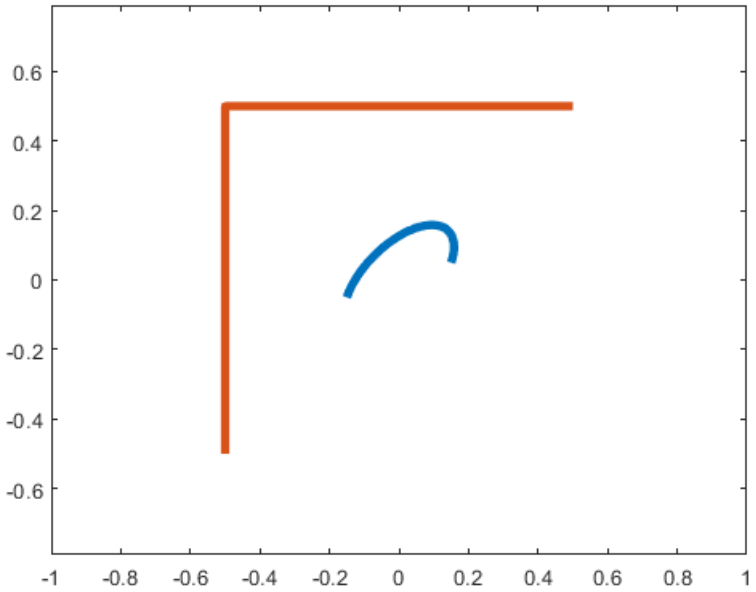

Figure 3.6: Inner and the outer curve which would form the ruled NURBS surface

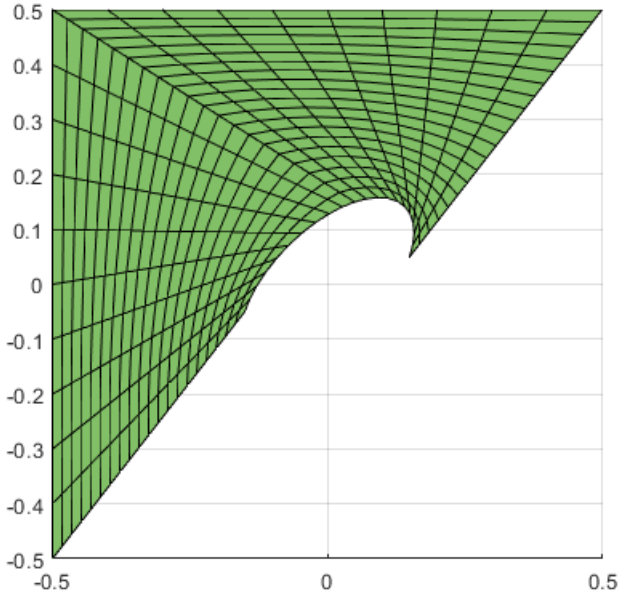

Figure 3.7: Ruled surface created between the inner and the outer curves

Then a ruled surface is generated between the two curves which makes up the first patch. The ruled surface between the two curves is obtained by linear interpolation between every two corresponding points on the curves. The next step is the creation of the second patch which is created by rotating the first patch by 180 degrees since the panel is symmetric about the axis of rotation. Such a methodology can be adopted to create cutouts of any complicated profile. The advantage of such a technique is that the user only needs to know the coordinates of the control points of the respective curves which make up the ruled surface. Popular NURBS software packages like Rhinoceros 3D (Rhino) can be used to provide the user with the coordinates of control points and corresponding knot vectors of the respective curves.

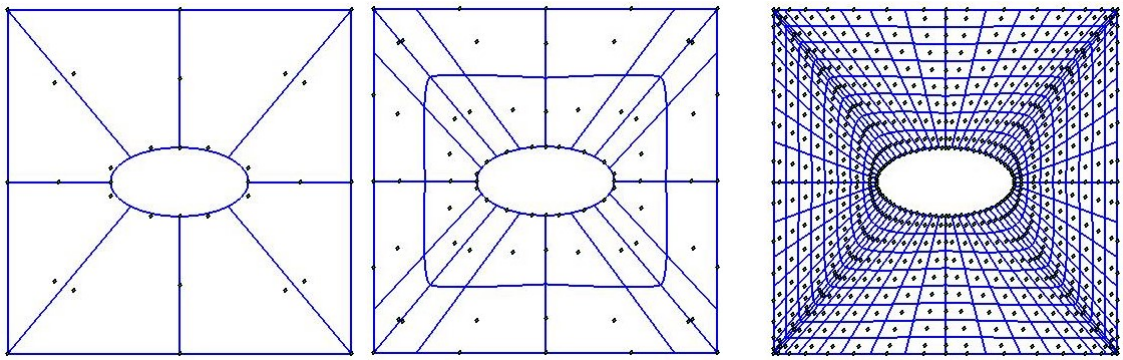

(a) refinement = 0; 4 elements (b) refinement = 1; 16 elements (c) refinement = 3; 256 elements

Figure 3.8: Isogeometric mesh plot with various degrees of refinement

Each patch was then meshed individually to various levels of refinement until convergent results were obtained as shown in Figure 3.8. It can be observed that IGA preserves the geometry even in the coarsest mesh (refinement =0).

3.2.7 Modeling complicated cutouts using a single NURBS patch

In this case, first the inner and the outer profile of such a panel is constructed using 1D NURBS curves as shown in Figure 3.9. The control points and weights used to construct these curves are detailed in Table 3.2 and Table 3.3. Figure 3.10 and Table 3.4 describe the mesh and the connectivity matrix for the coarsest mesh respectively.

Table 3.2: Control points and weights of the inner curve

P_{ij}	x	6	5	4	3	2	2	2	2	2	1.414	4	4.243	6	5.657	8	5.657	6
	y	8	8	8	8	8	7	6	5	4	1.414	2	1.414	4	2.828	6	5.657	8
	z	0	0	0	0	0	0	0	0	0	0	0	0	0	0	0	0	0
W		1	1	1	1	1	1	1	1	1	0.707	1	0.707	1	0.707	1	0.707	1

Table 3.3: Control points and weights of the outer curve

P_{ij}	x	10	5	0	0	0	5	10	10	10
	y	10	10	10	5	0	0	0	5	10
	z	0	0	0	0	0	0	0	0	0
W		1	1	1	1	1	1	1	1	1

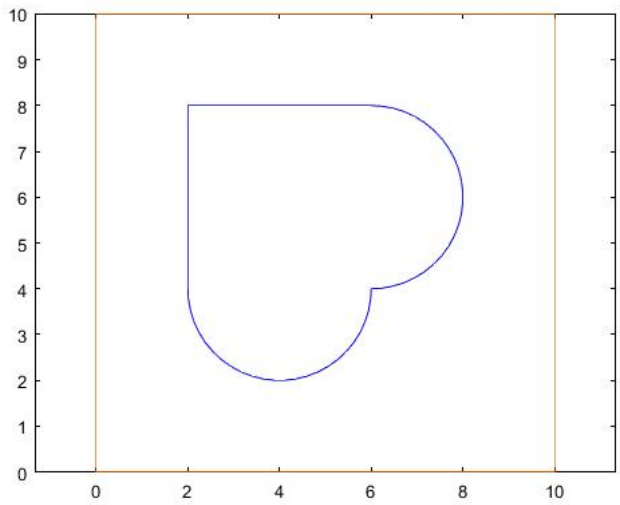

Figure 3.9: Inner and the outer curve to generate a plate with a complicated cutout

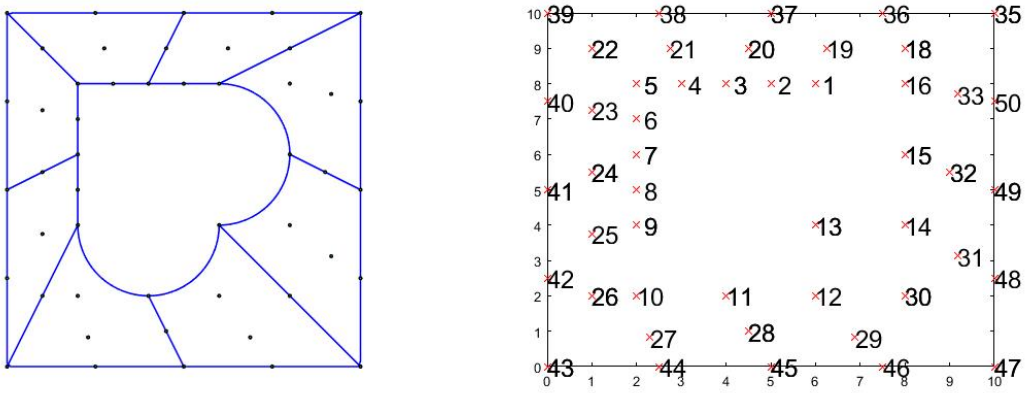

(a) Mesh Plot (b) Connectivity Plot

Figure 3.10: Mesh and connectivity plot of a plate with a complicated cutout

Table 3.4: Connectivity matrix of a plate with a complicated cutout

Element	**Node**								
	1	**2**	**3**	**4**	**5**	**6**	**7**	**8**	**9**
1	1	2	3	18	19	20	35	36	37
2	3	4	5	20	21	22	37	38	39
3	5	6	7	22	23	24	39	40	41
4	7	8	9	24	25	26	41	42	43
5	9	10	11	26	27	28	43	44	45
6	11	12	13	28	29	30	45	46	47
7	13	14	15	30	31	32	47	48	49
8	15	16	1	32	33	18	49	50	35

The FSDT which relies on C^0 continuity of the basis functions is employed in the patch interior unlike Kirchhoff-Love shell theory that relies on higher-order continuity of the basis functions as mentioned in [101].

3.2.8 A Three point parametrization of the curvilinear stiffener

Previous researchers [78], [1] and [79] involved curvilinear stiffeners with a parabolic profile. Using the parametric equation of the parabola and the start and the end point coordinates,

one can obtain the three control points which could define the Bezier curve [102]. Since any parabolic stiffener can be represented using three control points, the coordinates of the end control points $\Delta\epsilon$ and Point 2 (where δ_{dist} refers to the point [δ_{dist} ,δ_{dist}]) were used to represent the curvilinear stiffener.

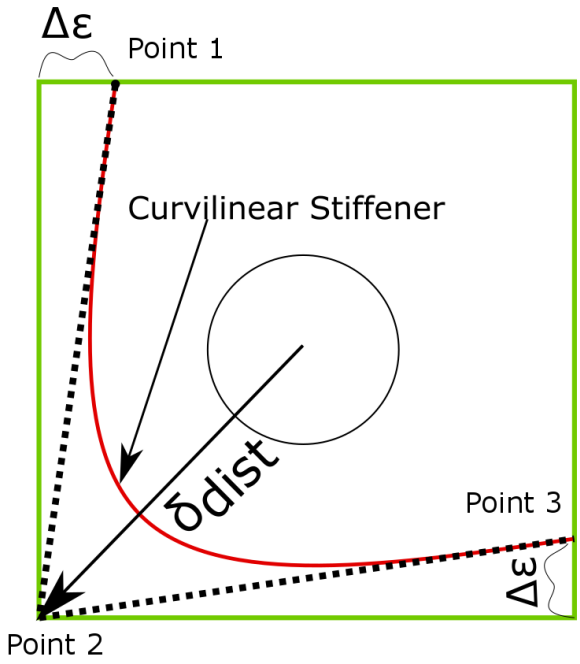

Figure 3.11: Parametrization of curvilinear stiffener

3.3 Thermal buckling- A two step analysis

In comparison to simple square plates where thermal loads can be converted to equivalent mechanical loads to find the critical buckling temperature, plates with cutouts pose a greater challenge. Application of constant through the thickness temperature results in regions of stress concentration at the cutouts. Hence the equivalent mechanical load concept cannot be used to compute the critical thermal buckling load and the problem needs to be approached

as a two step process. First, a static analysis was performed to compute the stresses in the presence of thermal loads and the resulting stresses are then used in the initial stress matrix to compute the geometric stiffness matrix. For numerical calculations, the NURBS basis functions of order $p = 2$ along with a Gaussian quadrature scheme were used to perform integration for each element.

3.4 Results and Discussion

To demonstrate and validate the method, thermal buckling analysis of curvilinearly stiffened laminated composite plates with various cutouts is carried out. Results are compared with those in existing literature for some cases while for some others, using commercially available software like ABAQUS. Parametric studies were performed which show the influence of both the cutout profile and the shape and position of the curvilinear stiffeners in the results.

3.4.1 Thermal buckling of laminated composite plates

Over the years and most recently [103], several researchers have analyzed the thermal buckling of symmetric laminated plates. A four layered symmetric crossply laminate $[0°/90°/90°/0°]$ with two width to depth ratios of $a/h = 10$ (Figure 3.2) and 100 were investigated for [25] two sets of boundary conditions. The plate is assumed to be a square of edge length 1 unit to make normalizations easy.

$$CCCC: \ u_0 = 0, v_0 = 0, \psi_x = 0, \psi_y = 0, w_0 = 0 \tag{3.47}$$

on all four edges.

$$SSSS: \begin{cases} u_0 = v_0 = w_0 = \phi_y = \phi_z = 0 \quad \text{on } x = 0,\ a \\ u_0 = v_0 = w_0 = \phi_x = \phi_z = 0 \quad \text{on } y = 0,\ b \end{cases} \tag{3.48}$$

Material properties are defined as [26], [25] and[103]

$$\begin{gathered} E_L/E_T = 15,\ G_{LT}/E_T = 0.5,\ G_{TT}/E_T = 0.3356, \\ \nu_{LT} = 0.3,\ \nu_{TT} = 0.49,\ \alpha_L/\alpha_0 = 0.015,\ \alpha_T/\alpha_0 = 1 \end{gathered} \tag{3.49}$$

where L and T refer to the directions parallel and perpendicular to the fibers and α_0 is the normalization factor for the thermal expansion coefficient. Table 3.5 illustrates the comparison of critical temperature obtained by NURBS-based IGA and FEM-Q16 [26], [25] and[103]. The critical buckling temperature values of the thinner plate have been scaled by 100.

Table 3.5: Critical thermal buckling load variation due to change in the angle of orientation of the elliptical cutout

	SSSS		CCCC	
L/h	FEM−Q16	Present	FEM−Q16	Present
100	0.0996	0.0995	0.3348	0.3343
10	0.0757	0.0752	0.1601	0.1604

3.4.2 Isotropic plate with a circular hole at the center

In order to illustrate the performance of IGA code in modeling holes, an isotropic plate with a circular hole at the center was considered. Variation of the critical thermal buckling load with respect to the radius of the hole was compared against Avci et al.[104]. The results

were obtained for simply supported (SSSS) and clamped (CCCC) boundary conditions. The material properties use are :

$$E = 208\ GPa,\ \nu = 0.3,\ \alpha = 1.17e-5 \tag{3.50}$$

As seen from Table 3.6, the results are in good agreement with those given in [104].

Table 3.6: Variation of critical load with respect to radius of the circular cutout

	CCCC		SSSS	
$\frac{radius}{width}$	Present	Avci	Present	Avci
0	29.35	29.16	10.83	10.97
0.1	28.70	28.57	10.79	10.82
0.2	30.33	29.07	10.73	10.68
40.3	37.05	35.37	11.29	11.14
0.4	52.29	49.67	12.81	12.57
0.5	80.40	78.55	15.70	15.34

3.4.3 Composite plate with elliptical cutout

To evaluate the versatility of this method, buckling analysis of plates with an elliptical cutout was considered. Results are compared with the ones obtained using ABAQUS. A unit square domain is considered with an elliptical cutout.

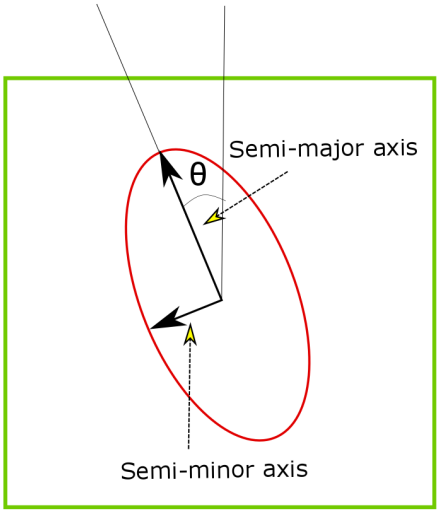

Figure 3.12: Dimensions and orientation of an elliptical cutout

The ellipse is defined by the semi major axis, the semi minor axis and the angle of orientation θ. For validation purposes, an ellipse of semi-major axis = 0.2, semi-minor axis = 0.1 and $\theta = 0$ was considered.

Number of elements	ABAQUS	Present
16	0.636	0.467
64	0.406	0.386
256	0.3782	0.378
1024	0.377	0.377

Table 3.7: The convergence of the critical thermal buckling load of a four-layer [0°/90°/90°/0°] laminated composite square plate.

It can be observed from Table 3.7 that the IGA approach yields relatively accurate results even for coarser meshes. For mode shape comparison (Figure 3.13) purposes, a plate with an elliptical cutout ($\theta = -45°$) was modeled in ABAQUS with an irregular mesh composed of 1028 elements. S8R: An 8-node doubly curved thick shell, reduced integration element was used to mesh the domain. IGA mode shape plot was obtained using 1024 elements.

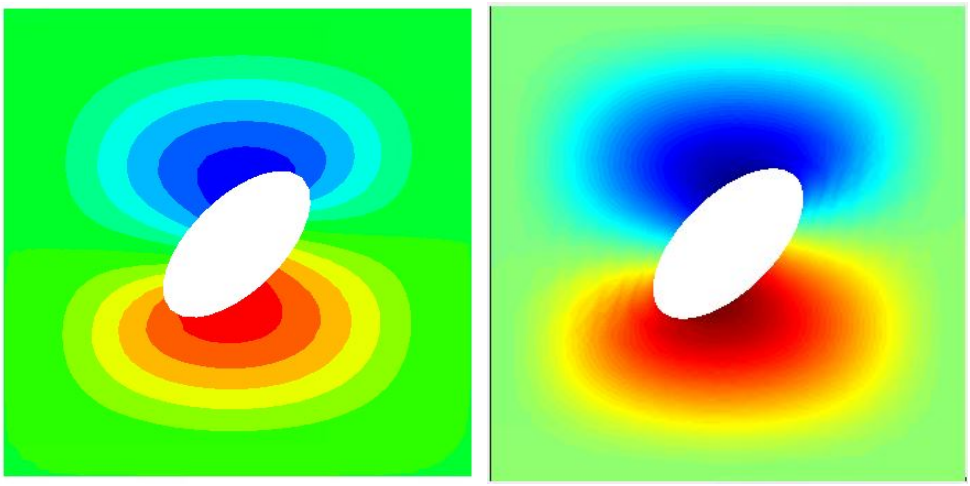

(a) ABAQUS (b) IGA

Figure 3.13: Buckling mode shape plots of a plate with an elliptical cutout ($\theta = -45°$)

Next, the variation of critical buckling load with respect to change in eccentricity and angle of orientation of the cutout was analyzed. Table 3.8 presents the results for three different eccentricities.

Table 3.8: Variation of thermal buckling load of a four-layer [0°/90°/90°/0°] laminated composite square plate.

θ	**Semi-minor axis=0.1 Semi-major axis=0.2**	**Semi-minor axis=0.1 Semi-major axis=0.3**	**Semi-minor axis=0.2 Semi-major axis=0.3**
0	0.375	0.402	0.622
15	0.386	0.443	0.649
30	0.420	0.543	0.718
45	0.462	0.652	0.807

If the plate is made of isotropic material, there is little to no effect of the orientation of the ellipse on the critical buckling load. However, there is a significant effect on the critical buckling load if the plate is made of laminated composite layers as can be seen in Table 3.8. The critical buckling load is heavily influenced by the eccentricity of the elliptical cutout. For

a crossply symmetric laminate, there is a monotonic increase in critical buckling load as the angle changes from 0 to 90°. However, the trend is not repeated for other ply orientations. Antisymmetric angle ply laminates experience a decrease in buckling load from $\theta = 0°$ to $\theta = 45°$ and then an increase from $\theta = 45°$ to $\theta = 90°$. This is due to the domination of B_{11} and B_{22} terms. However, the trend in the antisymmetric crossply laminate is the exact opposite. This is due to the domination of the coupling terms B_{16} and B_{26} terms. Symmetric angle ply laminates show very little sensitivity to change in cutout orientation angle due to the dominance of D_{16} and D_{26} terms.

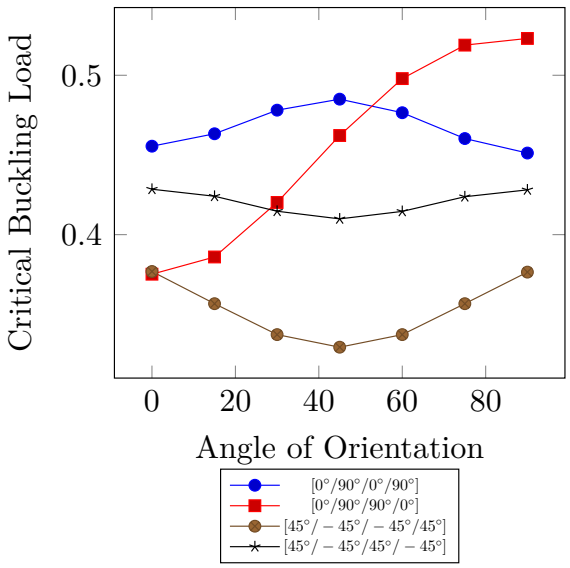

Figure 3.14: Variation of critical buckling load with respect to the angle of orientation of the elliptical cutout for different ply orientations

Table 3.9: Critical thermal buckling load variation due to change in the angle of orientation of the cutout

Ply Orientation				
θ	$[0°/90°/0°/90°]$	$[0°/90°/90°/0°]$	$[45°/-45°/-45°/45°]$	$[45°/-45°/45°/-45°]$
0°	0.456	0.375	0.377	0.429
15°	0.463	0.386	0.357	0.424
30°	0.478	0.420	0.337	0.415
45°	0.485	0.462	0.329	0.410
60°	0.477	0.498	0.337	0.415
75°	0.460	0.519	0.357	0.424
90°	0.451	0.523	0.377	0.428

3.4.4 Curvilinearly stiffened composite panels with central circular cutout

In this section, the influence of the central cutouts on clamped stiffened composite panels is studied. The stiffener is assumed to be fabricated from isotropic material with Young's modulus = E_T, Poisson's ratio = ν_{LT} and coefficient of thermal expansion = α_0. The stiffness ratio $\gamma = EI/bD$ and the area ratio $\delta = A_s/bt_p$ are 5 and 0.1 respectively, unless specified otherwise. To check the accuracy of the present displacement compatibility algorithm, results for clamped curvilinearly stiffened composite plate are compared with those obtained using ABAQUS. The curvilinear stiffener configuration was adopted from [105] and scaled proportionally to match the dimensions of the plate. From the ABAQUS library, the plate was meshed using 2040 S8R elements and curvilinear stiffener was meshed using 192 S8R elements (48 divisions along the arc length and 4 divisions along the depth direction). The IGA plate model was meshed using 1024 elements and the curvilinear stiffener using 32 elements. The critical buckling temperature result was observed to converge for these mesh

configurations. The first five eigen buckling models were extracted for each case. The buckling mode shapes obtained using the IGA approach are similar to the buckling mode shapes obtained using ABAQUS as can be seen from Figure 3.15.

	Present		ABAQUS	
Mode		ΔT_{cr}		ΔT_{cr}
1	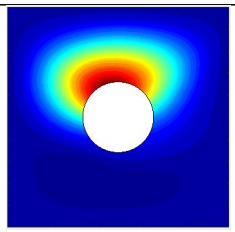	0.515	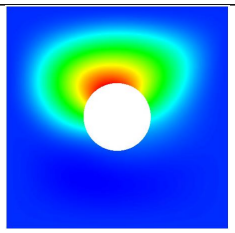	0.518
2	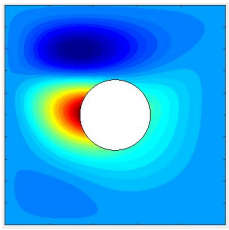	0.726	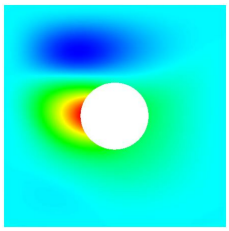	0.720
3	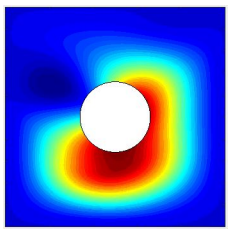	0.799	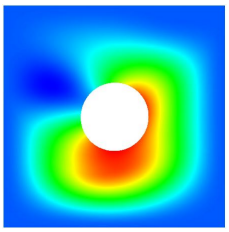	0.792
4	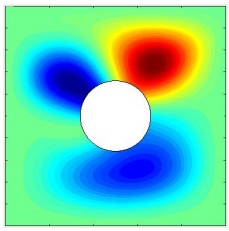	0.865	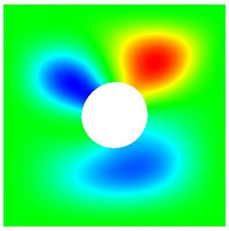	0.882
5	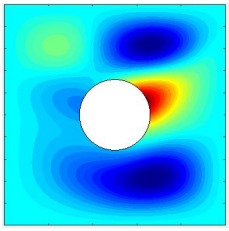	0.991	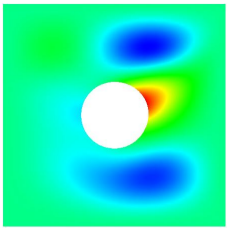	1.001

Figure 3.15: The first five eigenmode shape plots for a plate with curvilinear stiffener using a IGA and ABAQUS, a commercial available software.

3.4.5 Curvilinearly stiffened composite panels with an elliptical central cutout

In this section, results of curvilinearly stiffened composite panels with elliptical cutouts are presented. An ellipse of semi-major axis = 0.2 and semi-minor axis = 0.1 is considered for all cases. The variation of the critical thermal load with respect to angle orientations, ply orientations, stiffness ratios and different stiffener profiles (defined by $\Delta\epsilon$ Figure 3.11) are presented in Table 3.12 and Table 3.11.

Table 3.11: Variation of critical buckling load with respect to angle of orientation of the elliptical cutout for different ply orientations for $\gamma = 5$

$\Delta\epsilon = \mathbf{0}$				
θ	$[0°/90°/0°/90°]$	$[0°/90°/90°/0°]$	$[45°/-45°/-45°/45°]$	$[45°/-45°/45°/-45°]$
0	0.489	0.404	0.432	0.466
15	0.494	0.413	0.406	0.462
30	0.508	0.448	0.381	0.452
45	0.515	0.490	0.371	0.446

Table 3.12: Variation of critical buckling load with respect to the angle of orientation of the elliptical cutout for different ply orientations for $\gamma = 5$

$\Delta\epsilon = \mathbf{0.25}$				
θ	$[0°/90°/0°/90°]$	$[0°/90°/90°/0°]$	$[45°/-45°/-45°/45°]$	$[45°/-45°/45°/-45°]$
0	0.566	0.480	0.467	0.550
15	0.573	0.495	0.436	0.546
30	0.591	0.539	0.408	0.535
45	0.599	0.587	0.397	0.529

Table 3.13: Variation of critical buckling load with respect to the angle of orientation of the elliptical cutout for different ply orientations for $\gamma = 10$

$\Delta\epsilon = \mathbf{0}$				
θ	$[0°/90°/0°/90°]$	$[0°/90°/90°/0°]$	$[45°/-45°/-45°/45°]$	$[45°/-45°/45°/-45°]$
0	0.500	0.409	0.443	0.478
15	0.505	0.419	0.415	0.474
30	0.519	0.453	0.389	0.464
45	0.525	0.495	0.378	0.459

Table 3.14: Variation of critical buckling load with respect to the angle of orientation of the elliptical cutout for different ply orientations for $\gamma = 10$

$\Delta\epsilon = \mathbf{0.25}$				
θ	$[0°/90°/0°/90°]$	$[0°/90°/90°/0°]$	$[45°/-45°/-45°/45°]$	$[45°/-45°/45°/-45°]$
0	0.581	0.500	0.479	0.572
15	0.587	0.515	0.446	0.570
30	0.604	0.560	0.417	0.560
45	0.612	0.608	0.405	0.554

Comparing Tables 3.11 and 3.12 it can be observed that the stiffener profile plays a key role in the structural stability of the plate. Increasing the stiffness ratio is observed to increase the critical buckling load. However the response of the plate with respect to change in orientation angle follows the same trend as described in Section 3.4.3.

3.4.6 Composite panels with a complicated central cutout

To check the accuracy of the single patch algorithm, results for composite plate with a complicated cutout are compared with those obtained using ABAQUS. The profile of the internal cutout was obtained from [2]. From the ABAQUS library, the plate was meshed using 1076 S8R elements. The IGA plate model was meshed using 1024 elements. The critical buckling temperature result was observed to converge for these mesh configurations.

The first five eigen buckling models were extracted for each case. The buckling mode shapes obtained using the IGA approach are similar to the buckling mode shapes obtained using ABAQUS as can be seen from 3.16

	Present		ABAQUS	
Mode		ΔT_{cr}		ΔT_{cr}
1	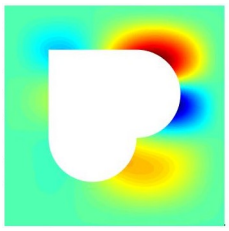	0.450	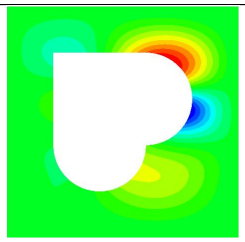	0.449
2	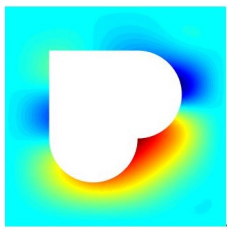	0.468	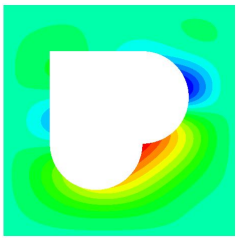	0.467
3	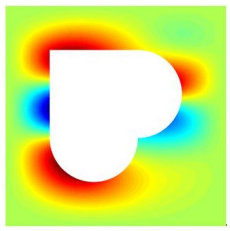	0.490	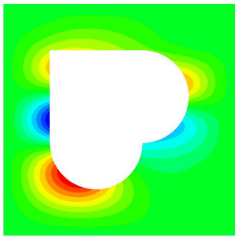	0.489
4	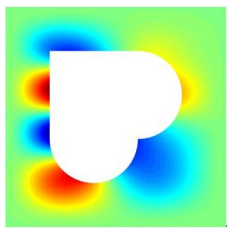	0.491	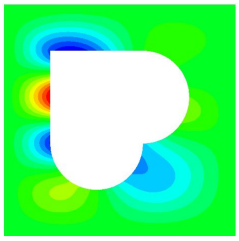	0.490
5	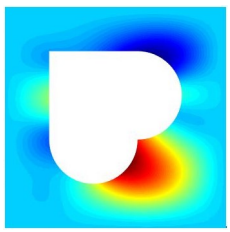	0.538	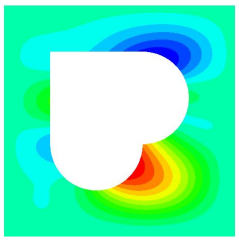	0.537

Figure 3.16: The first five eigenmode shape plots for a plate with a complicated cutout using a IGA and ABAQUS, a commercial available software.

3.5 Displacement Compatibility : Computational advantages

In this section, comparison of computational cost involved in achieving displacement compatibility using the Gauss point method [99, 106] and the modified Newton's method Section 3.2.5 is discussed. The computations are performed on a desktop computer with Intel(R) Xeon(R) 3.20 GHz CPU processor. The present method has been coded in the Matlab®. A stiffened plate with a central circular cutout of radius 0.15 was considered. The material properties, ply orientation and stiffener profile were the same as mentioned in Section 3.2.5. The levels of mesh refinement for the plate and the stiffener are assumed to be the same. The computational time (in seconds) to achieve displacement compatibility are compared for this case. It is observed from Table 3.16 that the Newton's method has significant computational advantages over the Gauss point method.

Table 3.16: Comparison of computational time (in seconds) between the modified Newton's method and the Gauss point method

Refinement	Newton's Method	Gauss point Method
2	0.45	6.38
3	0.55	9.41
4	0.80	17.92

3.6 Convergence studies

Convergence studies on a stiffened plate with a cutout are not as straightforward as a simple plate problem since the size of the cutout, mesh size of the stiffener and the plate affect the

results. We consider a stiffened plate with a central circular cutout. The material properties, ply orientation and stiffener profile were the same as mentioned in Section 3.2.5. Figures 3.17, 3.18 and 3.19 present the change of critical buckling loads with respect to various stiffener and plate mesh sizes for cutouts of varying radii. The stiffener mesh density has very little effect on the results for plate mesh refinement ≥ 3. However, as the radius of the cutout is increased to 0.25, the stiffener mesh density impacts the convergence to a much higher degree (Figure 3.17).

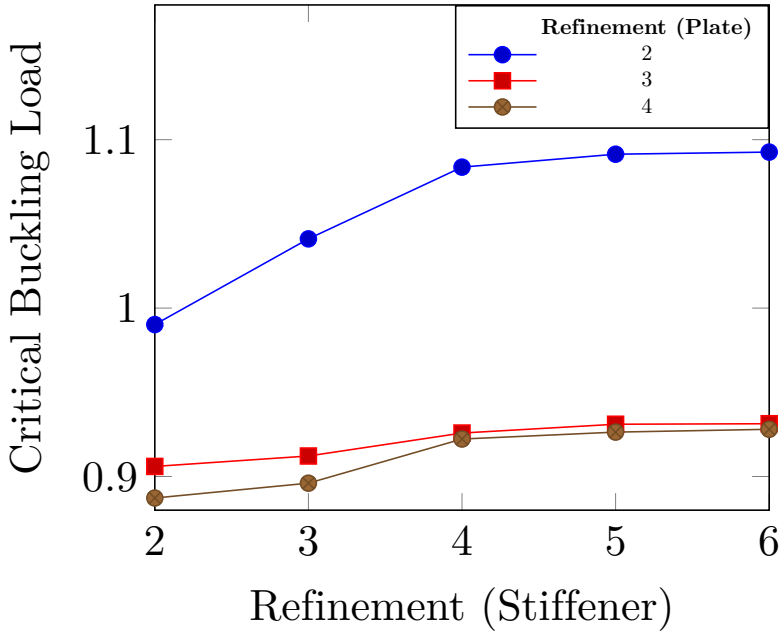

Figure 3.17: Variation of critical buckling load with respect to various stiffener and plate mesh sizes for $radius = 0.25$

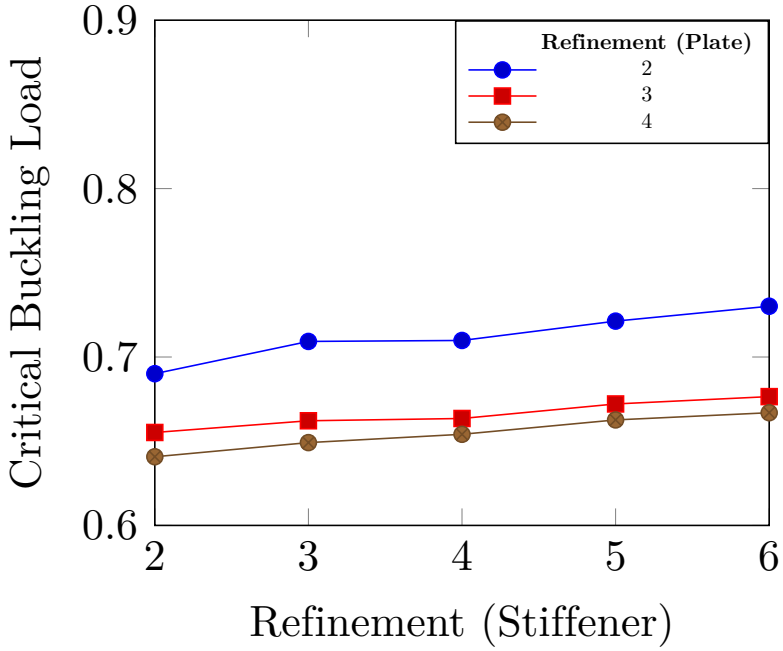

Figure 3.18: Variation of critical buckling load with respect to various stiffener and plate mesh sizes for $radius = 0.2$

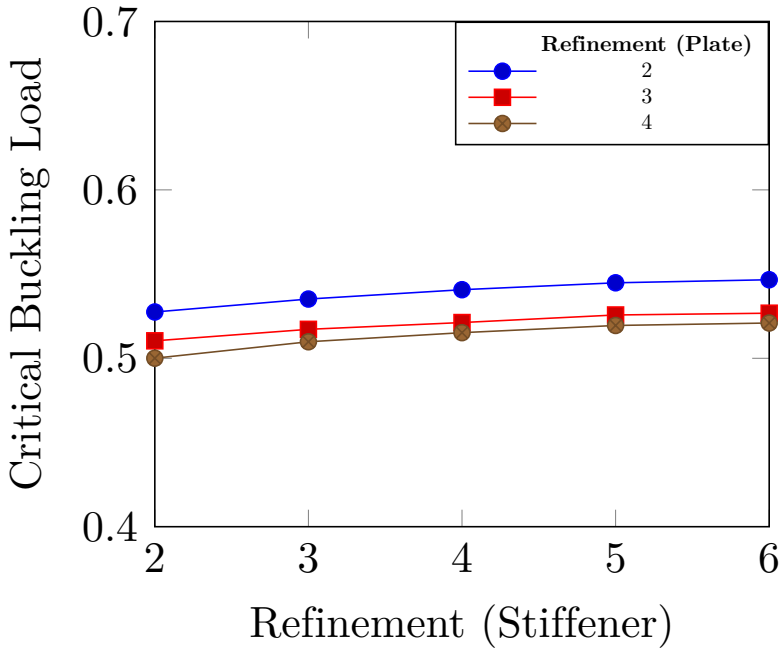

Figure 3.19: Variation of critical buckling load with respect to various stiffener and plate mesh sizes for $radius = 0.15$

Chapter 4

Analysis of Stiffened Laminated Composite Plates with Noncentric Cutouts Using Isogeometric Level Set Method

4.1 Introduction

In this chapter, thermal buckling analysis of stiffened composite plates with a cutout is presented. The internal cutouts are represented using level set functions. The plate is assumed to be subjected to a unit rise in temperature. The stiffness matrices are derived using the first-order shear deformation theory. The proposed method is validated by comparing it with available literature. Useful conclusions are derived from the response of stiffened composite plates due to change in width-to-thickness ratio, fiber orientation, ply layups, shape and size of the cutouts and the boundary conditions.

4.1.1 Level Set Function

A signed distance function is utilized here to identify the enriched elements (elements cut by the cutout boundary), the outer elements (elements that are the part of the plate) and inner elements (elements that fall completely within the cutout geometry) using the equation of a circle, given as:

$$\phi(\mathbf{X}) = |\mathbf{X} - \mathbf{X_c}| - r \tag{4.1}$$

Where $\phi(\mathbf{X})$ is the level set value at coordinates $\mathbf{X}$. $\mathbf{X_c}$ is the coordinates of the center of the circular cutout and r is the radius of the cutout. These values are stored at all control points for later use. Next, the coordinates of the points where the geometry of the cutout intersects the element is computed (Figure 4.1). This process will approximate the shape of the cutout as a polygon with sides equal to the number of enriched elements. This process has no impact on elements that are not cut by the interface.

The implemented enrichment function is:

$$\psi(\mathbf{X}) = \sum_{i=1}^{4} |\phi_I| N(\mathbf{X})_I - |\sum_{i=1}^{4} \phi_I N(\mathbf{X})_I| \tag{4.2}$$

The enrichment function ψ at coordinates $\mathbf{X}$ is evaluated as a combination of control point level set values and the shape functions. Compared to other choices for enrichment functions this has two major advantages. As the enrichment function has a zero value outside the cut elements as well as in the cut element control points there will be no contribution to

the stiffness matrix in an element that are not cut by the interface and the displacements evaluated at the control points will not have any extra contribution either.

4.1.2 Triangulation and Numerical Integration

Figure 4.1 shows a non enriched element (A) and an enriched element (B) in the $x-y$ coordinate system. Since some part of such enriched elements lie within the cutout, for numerical integration purposes, they have to be treated differently. For this, the coordinates of the points where the geometry of the cutout intersects the element is computed (Figure 4.1). The creation of additional points will enable the division of such a quadrilateral element into triangles and the process will approximate the shape of the cutout as a polygon with sides equal to the number of enriched elements

Consider one such triangular geometry (Δ_1). Let the function $f(x, y)$ determine some property at $[x, y]$, a point within this geometry. Suppose another property, that is evaluated by the integration of $f(x, y)$ over this geometry is of interest. An analytical calculation of the integrand is either impossible or very expensive. It is convenient to use Gauss quadrature formula in which the integrand is approximated as a weighted sum of the function values at a number of predetermined points (exact for n points for a function of order $2n-1$ in 1D). These points are given in a transformed coordinate system (natural coordinate system).

Thus, to integrate $f(x, y)$,

$$I = \int_{\Delta_1} f(x, y) dx dy \tag{4.3}$$

a transformation into this natural coordinate system and a change of variables is necessary.

This transformation is performed using a Jacobian matrix, $\mathbf{J_{el}}$ and is defined by

$$\begin{bmatrix} dx \\ \\ dy \end{bmatrix} = \mathbf{J_{el}} \begin{bmatrix} d\xi \\ \\ d\eta \end{bmatrix} \tag{4.4}$$

Where,

$$\mathbf{J_{el}} = \begin{bmatrix} \frac{\partial x}{\partial \xi} & \frac{\partial x}{\partial \eta} \\ \\ \frac{\partial y}{\partial \xi} & \frac{\partial y}{\partial \eta} \end{bmatrix} \tag{4.5}$$

Then it follows that

$$I = \frac{1}{2} \int_0^1 \int_0^{1-\eta} f(x(\xi,\eta), y(\xi,\eta)) \begin{vmatrix} \frac{\partial x}{\partial \xi} & \frac{\partial x}{\partial \eta} \\ \\ \frac{\partial y}{\partial \xi} & \frac{\partial y}{\partial \eta} \end{vmatrix} d\xi d\eta \tag{4.6}$$

By numerical integration the quantity can be evaluated

$$I \cong \frac{1}{2} \sum_1^i w_i f(x(\xi,\eta), y(\xi,\eta)) \begin{vmatrix} \frac{\partial x}{\partial \xi} & \frac{\partial x}{\partial \eta} \\ \\ \frac{\partial y}{\partial \xi} & \frac{\partial y}{\partial \eta} \end{vmatrix} \tag{4.7}$$

Where i is the number of Gauss points in the triangle. This will be useful in codes where element stiffness matrices for elements with enriched nodes are evaluated.

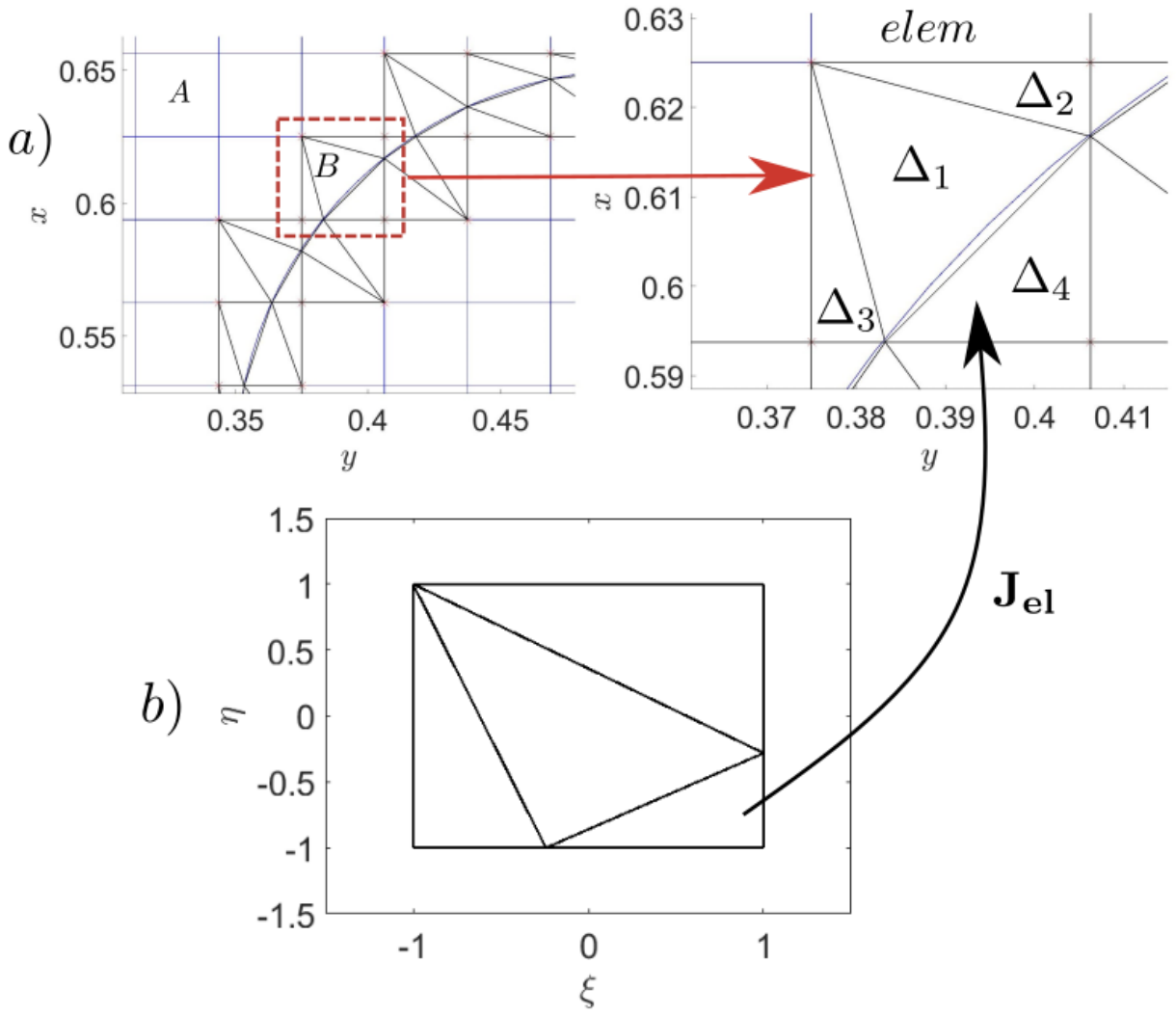

Figure 4.1: Mappings and transformation from physical space to natural space

The element stiffness matrix will have a shape as follows:

$$\mathbf{K_e^{ij}} = \iint_{elem} \mathbf{B_i^T D B_j} t dx dy \tag{4.8}$$

Where,

$$\mathbf{B_i} = [\mathbf{B_{STD}} \mid \mathbf{B_{ENR}}] \tag{4.9}$$

Where $\mathbf{B_i}$ could be one of $\mathbf{B_p}$, $\mathbf{B_s}$ or $\mathbf{B_p^{NL}}$. The subscripts **STD** and **ENR** refer to standard non-enriched elements and enriched elements respectively. For a four noded isoparametric element the shape functions are defined in the isoparametric domain. However, the **B** matrices are functions of the shape functions which are defined in the isoparametric coordinate system $\xi - \eta$ (Figure 4.2) , but the Gauss points and weights associated for a triangular domain aren't. They are defined in the $\xi' - \eta'$ coordinate system (Figure 4.3 with the vertices of the triangle located at:

$$[\xi'_1, \eta'_1] = [0\ 0]\,; [\xi'_2, \eta'_2] = [1\ 0]\,; [\xi'_1, \eta'_1] = [0\ 1]\,; \tag{4.10}$$

Hence, the mapping of these Gauss points to the isoparametric coordinate system is to be performed for each triangle.

These Gauss points can be mapped using nodal shape functions and isoparametric coordinates of vertices as follows:

$$\begin{bmatrix} \xi_{gp} & \eta_{gp} \end{bmatrix}_{\Delta_1} = \begin{bmatrix} 1-\xi'_{gp}-\eta'_{gp} \\ \xi'_{gp} \\ \eta'_{gp} \end{bmatrix}^T_{\Delta_1} \begin{bmatrix} \xi_1 & \eta_1 \\ \xi_2 & \eta_2 \\ \xi_3 & \eta_3 \end{bmatrix}_{\Delta_1} \tag{4.11}$$

The weight associated with each Gauss point will be scaled using the ratio of the areas of the triangles in the ξ-η coordinate system and the ξ'-η' coordinate system. We now have Gauss points and associated weights in the isoparametric coordinate system to in order to perform numerical integration.

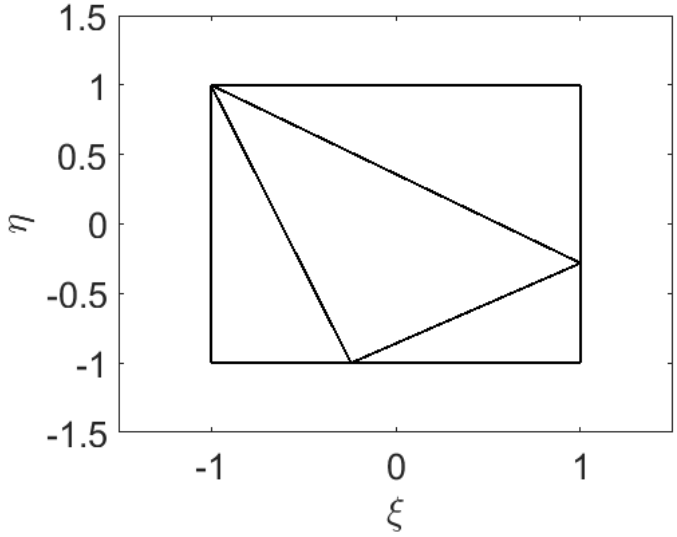

Figure 4.2: Element and triangle transformed into coordinate system appropriate for B_{matrix} calculation

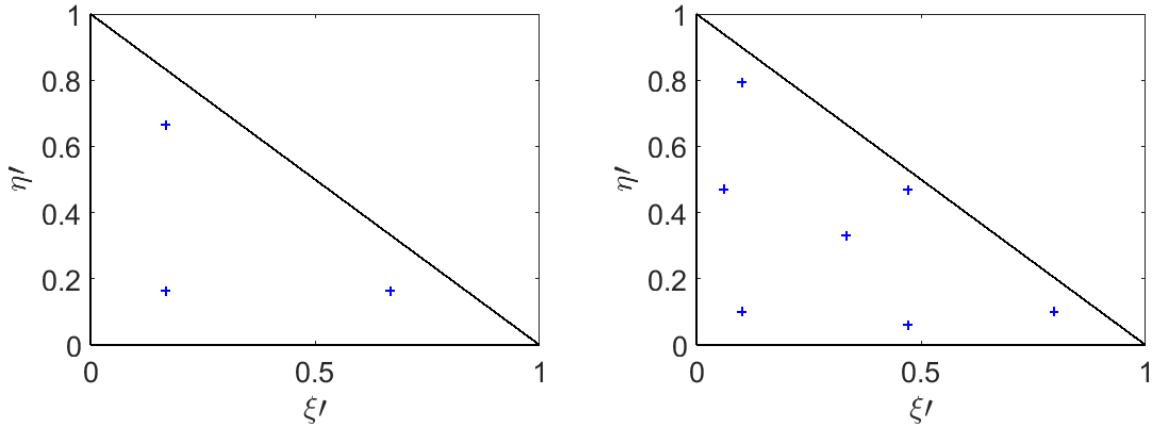

(a) 3 Gauss points (b) 7 Gauss points

Figure 4.3: Triangle transformed into coordinate system compatible with given Gauss-points

Now, all the tools needed for the numerical integration are available. The stiffness matrix contribution from the triangle can be calculated now as

$$\iint_{\Delta} \mathbf{B_i^T}(x,y)\mathbf{DB_j}(x,y)t dx dy = \frac{1}{2}\sum_{k=1}^{n} \mathbf{B_i}(x,y)^T \mathbf{DB}_j(x,y) t w_k \left|\mathbf{J}_{\Delta}\right| \left|\mathbf{J}_{el}\right| \tag{4.12}$$

Where B_i and B_j are either $\mathbf{B_{STD}}$ or $\mathbf{B_{ENR}}$, depending on what part of the stiffness matrix are currently being calculated and n is the number of Gauss points in the element.

The target expression (a sample entry in a $\mathbf{B_{STD}}$ matrix) is,

$$N_{1,x} = \frac{\partial \xi}{\partial x}\frac{\partial N_1}{\partial \xi} + \frac{\partial \eta}{\partial x}\frac{\partial N_1}{\partial \eta} \tag{4.13}$$

Where N is the basis function. While, for the enriched B-matrix $\mathbf{B_{ENR}}$,

$$\frac{\partial(\psi N_1)}{\partial x} = N_1 \frac{\partial \psi}{\partial x} + \frac{\partial N_1}{\partial x}\psi \tag{4.14}$$

Where, ψ is the enrichment function. Detailed Matlab code can be found in 6.2

4.2 Results and Discussion

To demonstrate and validate the method, thermal buckling analysis of curvilinearly stiffened laminated composite plates with various cutouts is carried out. Results are compared with existing literature for some cases while for some others, using commercially popular software like ABAQUS. Parametric studies were performed which show the influence of both the cutout profile and the shape and position of the curvilinear stiffeners in the results.

4.2.1 Thermal buckling of laminated composite plates

Over the years, and most recently [107], several researchers have analyzed the thermal buckling of symmetric laminated plates. A four-layer [0°/90°/90°/0°] laminated plate with the two ratios of $a/h = 10$ (Figure 3.2) and 100 were investigated for [25] two sets of boundary conditions. The plate is assumed to be a square of edge length 1 unit to make normalizations easy.

$$CCCC: \ u_0 = 0, v_0 = 0, \psi_x = 0, \psi_y = 0, w_0 = 0 \tag{4.15}$$

on all four edges.

$$SSSS: \begin{cases} u_0 = v_0 = w_0 = \phi_y = \phi_z = 0 \quad \text{on } x = 0,\ a \\ u_0 = v_0 = w_0 = \phi_x = \phi_z = 0 \quad \text{on } y = 0,\ b \end{cases} \tag{4.16}$$

Material properties are defined as [108], [25] and[107]

$$\begin{gathered} E_L/E_T = 15,\ G_{LT}/E_T = 0.5,\ G_{TT}/E_T = 0.3356, \\ \nu_{LT} = 0.3,\ \nu_{TT} = 0.49,\ \alpha_L/\alpha_0 = 0.015,\ \alpha_T/\alpha_0 = 1 \end{gathered} \tag{4.17}$$

where L and T refer to the directions parallel and perpendicular to the fibers and α_0 is the normalization factor for the thermal expansion coefficient. Table 4.1 illustrates the comparison of critical temperature obtained by NURBS-based IGA and FEM-Q16 [108], [25] and[107]. The critical buckling temperature values of the thinner plate have been scaled by 100.

Table 4.1: Critical thermal buckling load variation due to change in angle of orientation of the elliptical cutout

	SSSS		CCCC	
L/h	FEM−Q16	Present	FEM−Q16	Present
100	0.0996	0.0995	0.3348	0.3343
10	0.0757	0.0752	0.1601	0.1604

4.2.2 Isotropic plate with a circular hole at the center

In order to illustrate the performance of IGA code while modeling plates with holes, an isotropic plate with a circular hole at the center was considered. Variation of the critical thermal load with respect to the radius of the hole was compared against Avci et al.[109].

The results were obtained for simply supported (SSSS) and clamped (CCCC) boundary conditions. The material properties of the plate are given as:

$$E = 208\ GPa,\ \nu = 0.3,\ \alpha = 1.17e-5 \tag{4.18}$$

As seen from the Table 4.2, the results are in good agreement with [109].

Table 4.2: Variation of critical load with respect to radius of the circular cutout

	CCCC		SSSS	
$\frac{diameter}{width}$	Present	Avci	Present	Avci
0	29.35	29.16	10.83	10.97
0.1	28.01	28.57	10.64	10.82
0.2	29.17	29.07	10.52	10.68
0.3	35.27	35.37	11.01	11.14
0.4	49.53	49.67	12.48	12.57
0.5	78.74	78.55	15.41	15.34

4.2.3 Composite plate with elliptical cutout

To demonstrate the versatility and to validate the method, buckling analysis of plates with an elliptical cutout was considered. Results are compared with those obtained using ABAQUS. A unit square domain is considered with an elliptical cutout. The selected examples are for comparison purpose only and do not represent the full capabilities of the proposed method.

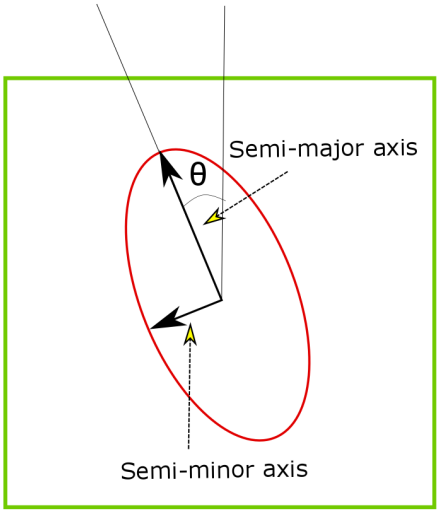

Figure 4.4: Dimensions and orientation of an elliptical cutout

The ellipse is defined by the semi major axis, the semi minor axis and the angle of orientation θ. For validation purposes, an ellipse of semi-major axis = 0.2, semi-minor axis = 0.1 and $\theta = 0$ was considered.

Table 4.3: The convergence of the critical thermal buckling load of a four-layer [0°/90°/90°/0°] laminated composite square plate.

Number of elements	**ABAQUS**	**Present**
16	0.636	0.653
64	0.406	0.421
256	0.3782	0.401
1024	0.377	0.381

It can be observed from Table 4.3 that level set IGA approach yields relatively the same rate of convergence as ABAQUS. For mode shape comparison (Figure 4.5) purposes, a plate with an elliptical cutout ($\theta = 45°$) was modeled in ABAQUS with an irregular mesh composed of 1028 elements. S8R: An 8-node doubly curved thick shell, reduced integration element was used to mesh the domain. IGA mode shape plot was obtained using 1024 elements.

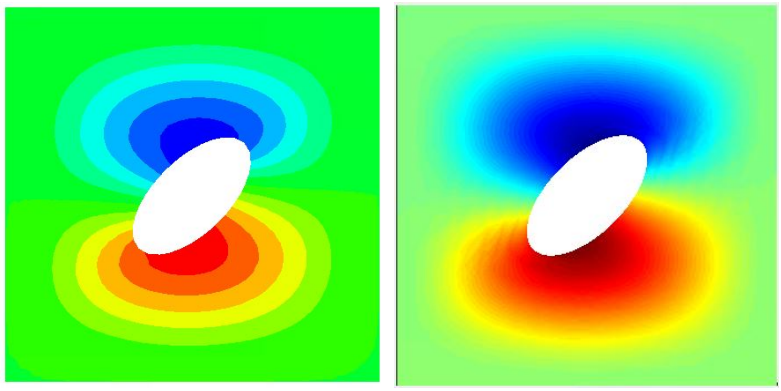

(a) ABAQUS (b) IGA

Figure 4.5: Buckling mode shape plots of a plate with an elliptical cutout ($\theta = 45°$)

Next, the variation of critical buckling load with respect to change in eccentricity and angle of orientation of the cutout was analyzed. Table 4.4 presents the results for three different eccentricities. The results of the present method (LSM) are compared with those obtained using the Multi-Patch method (MPM)

Table 4.4: Variation of thermal buckling load of a four-layer [0°/90°/90°/0°] laminated composite square plate.

θ	**Semi-minor axis=0.1 Semi-major axis=0.2**		**Semi-minor axis=0.1 Semi-major axis=0.3**		**Semi-minor axis=0.2 Semi-major axis=0.3**	
	LSM	**MPM**	**LSM**	**MPM**	**LSM**	**MPM**
0	0.381	0.379	0.413	0.402	0.633	0.633
15	0.395	0.390	0.443	0.438	0.659	0.653
30	0.427	0.421	0.532	0.525	0.729	0.715
45	0.469	0.460	0.641	0.630	0.809	0.807

4.2.4 Curvilinearly stiffened composite panels with a noncentric circular cutout

In this sub section, the influence of the noncentric circular cutouts on clamped stiffened composite panels is studied. The stiffener is isotropic with Young's modulus = E_T, Poisson's ratio = ν_{LT} and coefficient of thermal expansion = α_0. The stiffness ratio $\gamma = EI/bD$ and the area ratio $\delta = A_s/bt_p$ are 5 and 0.1 respectively unless specified. To check the robustness of the level set method, results for clamped curvilinearly stiffened composite plate are compared with those obtained using ABAQUS. A noncentric circular cutout of radius 0.15 with center at $(0.3, 0.7)$ was assumed. The curvilinear stiffener configuration was adopted from [78] and scaled proportionally to match the dimensions of the plate. From the ABAQUS library, the plate was meshed using 3040 S8R elements and curvilinear stiffener was meshed using 192 elements S8R elements (48 divisions along the arc length and 4 divisions along the depth direction). The IGA plate model was meshed using 4096 elements and the curvilinear stiffener using 32 elements. The critical buckling temperature result was observed to converge for this mesh configuration. The first five eigen buckling models were extracted for each case. As seen from Figure 4.6 the buckling mode shapes obtained using IGA and ABAQUS are comparable.

	Present		ABAQUS	
Mode		ΔT_{cr}		ΔT_{cr}
1	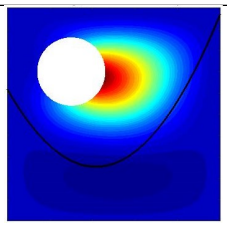	0.426	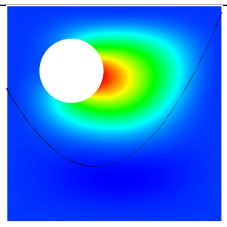	0.420
2	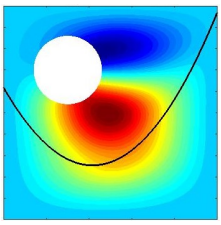	0.535	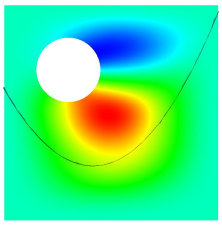	0.523
3	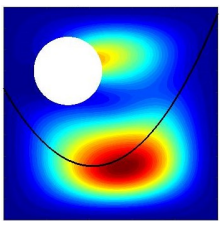	0.708	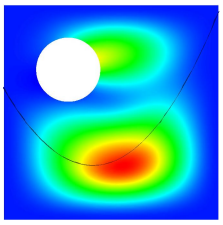	0.698
4	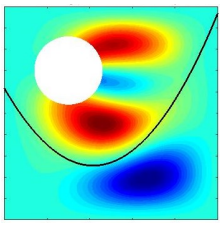	0.910	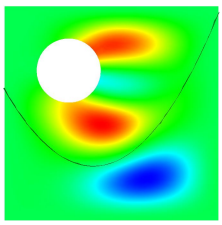	0.906
5	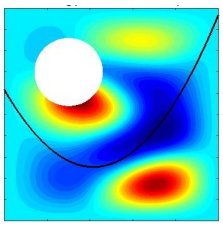	1.070	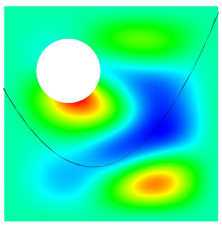	1.007

Figure 4.6: First five eigenmode shape plots for a plate with curvilinear stiffener using LSM and ABAQUS, a commercial available software.

4.2.5 Curvilinearly stiffened composite panels with an elliptical central cutout

In this section, results of curvilinearly stiffened composite panels with elliptical cutouts are presented. An ellipse of semi-major axis = 0.2 and semi-minor axis = 0.1 is considered for all cases. The variation of the critical thermal load with respect to angle orientations, ply orientations, stiffness ratios and different stiffener profiles (defined by $\Delta\epsilon$ Figure 3.11) are presented in Table 4.6 and Table 4.7. The results obtained using present method (LSM) and the Multi-Patch method (MPM) are in excellent agreement.

Table 4.6: Variation of critical buckling load with respect to angle of orientation of the elliptical cutout for different ply orientations for $\gamma = 5$

$\Delta\epsilon = 0$								
θ	**Antisymmetric Cross-Ply**		**Symmetric Cross-Ply**		**Symmetric Angle-Ply**		**Antisymmetric Angle-Ply**	
	LSM	**MPM**	**LSM**	**MPM**	**LSM**	**MPM**	**LSM**	**MPM**
0	0.475	0.473	0.413	0.406	0.425	0.423	0.456	0.455
45	0.507	0.497	0.494	0.488	0.370	0.366	0.436	0.434
$\Delta\epsilon = 0.25$								
0	0.559	0.553	0.492	0.481	0.469	0.462	0.548	0.542
45	0.598	0.592	0.595	0.590	0.406	0.395	0.525	0.521

Table 4.7: Variation of critical buckling load with respect to the angle of orientation of the elliptical cutout for different ply orientations for $\gamma = 10$

$\Delta\epsilon = 0$								
θ	**Antisymmetric Cross-Ply**		**Symmetric Cross-Ply**		**Symmetric Angle-Ply**		**Antisymmetric Angle-Ply**	
	LSM	**MPM**	**LSM**	**MPM**	**LSM**	**MPM**	**LSM**	**MPM**
0	0.488	0.485	0.417	0.409	0.443	0.443	0.469	0.468
45	0.509	0.509	0.502	0.495	0.83	0.378	0.448	0.449
$\Delta\epsilon = 0.25$								
0	0.590	0.581	0.509	0.501	0.485	0.479	0.576	0.572
45	0.619	0.612	0.618	0.610	0.410	0.405	0.560	0.554

4.2.6 Curvilinearly stiffened composite panels with a complicated cutout

The present method is applied to analyze a stiffened laminated composite plate with a clover shaped cutout Figure 4.7. The cutout is a boolean of three circles of radius 0.15 resulting in a clover shape. The center of circles **A**, **B** and **C** are at $(0.4, 0.65)$, $(0.5, 0.7)$ and $(0.5, 0.6)$ respectively. Figure 4.7 shows the mesh plot for the plate geometry with the red region being the enriched elements.

To check the accuracy of the level set algorithm, results for clamped curvilinearly stiffened composite plate with a clover shaped cutout are compared with those obtained using ABAQUS. The curvilinear stiffener configuration was adopted from [78] and scaled proportionally to match the dimensions of the plate. From the ABAQUS library, the plate was meshed using 3040 S8R elements and curvilinear stiffener was meshed using 192 elements S8R elements (48 divisions along the arc length and 4 divisions along the depth direction).

The IGA plate model was meshed using 4096 elements and the curvilinear stiffener using 32 elements. The first five eigen buckling models were extracted for each case. The buckling mode shapes obtained using the IGA approach are similar to those obtained using ABAQUS as can be seen from Figure 4.8.

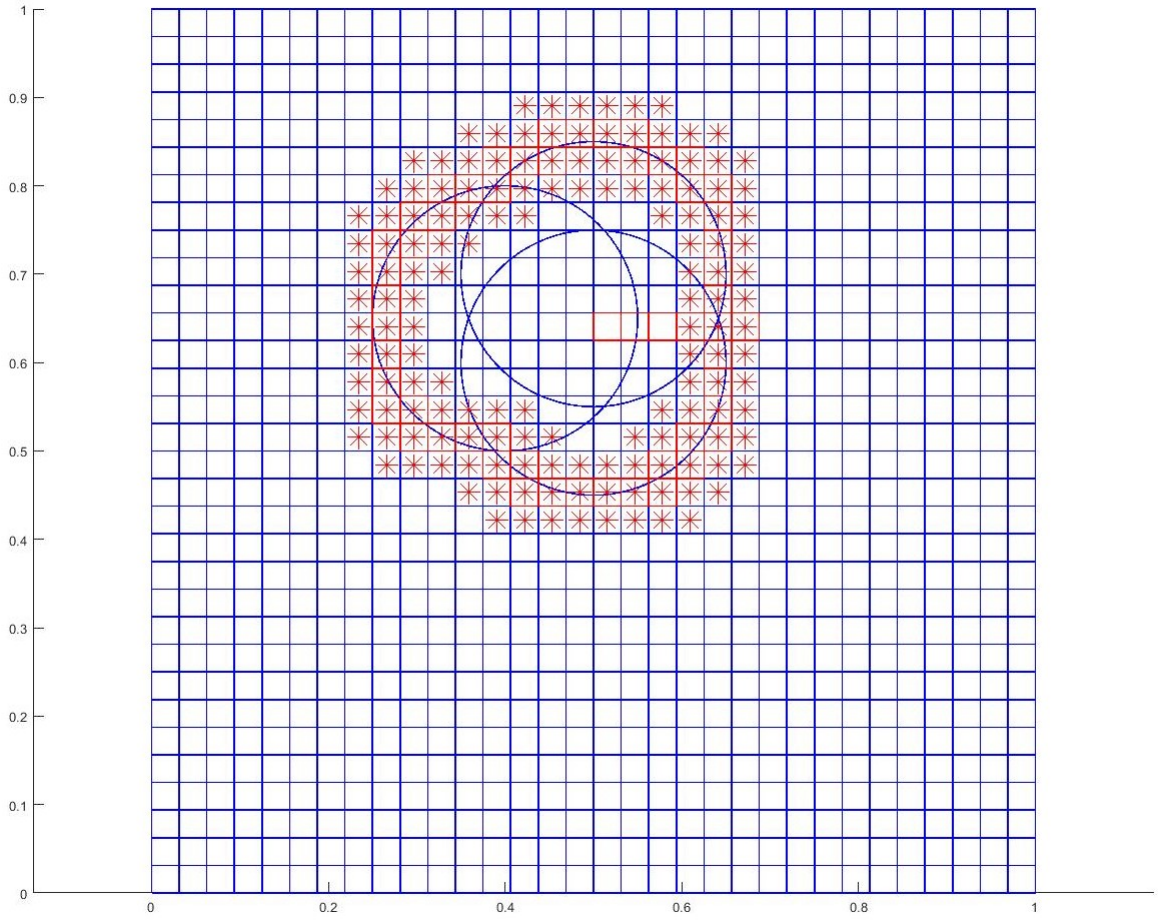

Figure 4.7: Isogeometric mesh plot of a plate with clover shaped cutout constructed with three cirles. The enriched elements are shown in red

	Present		ABAQUS	
Mode		ΔT_{cr}		ΔT_{cr}
1	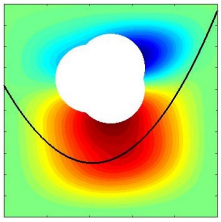	0.751	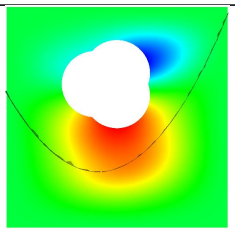	0.748
2	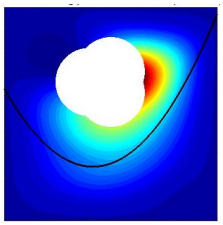	0.827	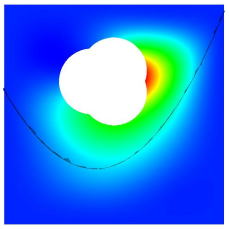	0.817
3	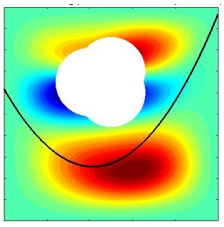	0.961	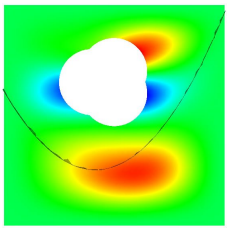	0.955
4	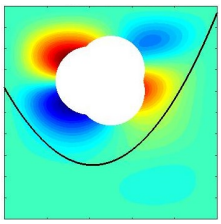	1.009	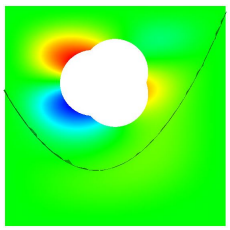	1
5	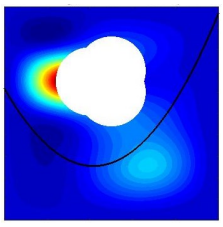	1.096	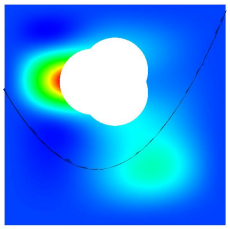	1.085

Figure 4.8: First five eigenmode shape plots for a plate with curvilinear stiffener using a LSM and ABAQUS, a commercial available software.

4.3 Advantages and limitations

One of the advantages of the level set method is their ability to use the same mesh controls on the plate for different types of cutouts. Figure 4.9 shows how the plate is discretized using 16 x 16 elements for circular as well as elliptical cutouts.

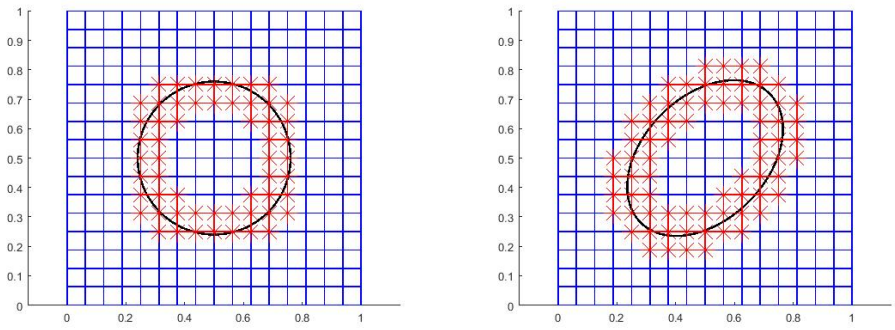

(a) circular (b) angled elliptical

Figure 4.9: Identical IGA mesh for circular and elliptical cutouts

Discussions in Section 4.1.2 describe the creation of additional degrees of freedom while implementing the level set method. Table 4.9 shows the number of additional degrees of freedom created for each levels of refinement for a plate with a cutout of radius 0.15. It can be observed that the total degrees of freedom (**nDoF** = Total number of Gauss points x 5) increase much steeply than the additional degrees of freedom (**Extra DoF**) with increase in refinement levels.

Table 4.9: Additional degrees of freedom with respect to an increase in refinement

Refinement	**nDoF**	**Extra DoF**
3	660	160
4	1920	300
5	6320	540

Next, computational cost due to these additional degrees of freedom was analyzed. Two cases were considered, a stiffened plate without any cutout (Case 1) and a stiffened plate with a central circular cutout of radius 0.15. The material properties, ply orientation and stiffener profile were the same as mentioned in Section 4.2.4. The computational time (in seconds) to perform the static and the eigenvalue analyses are compared for each case (Table 4.10, Figures 4.11 and 4.10). It is observed that the additional degrees of freedom have a much higher influence on the static analysis compared to the eigenvalue analysis. However, the difference is very little for lower levels of refinement.

Table 4.10: Computational time (in seconds) with respect to refinement for static and eigenvalue analyses

Refinement	4		5		6	
	Static	Eigenvalue	Static	Eigenvalue	Static	Eigenvalue
Case 1	0.0342	0.2045	0.2008	0.7087	1.2722	4.3813
Case 2	0.0504	0.2244	0.2014	0.8724	4.5132	4.5352

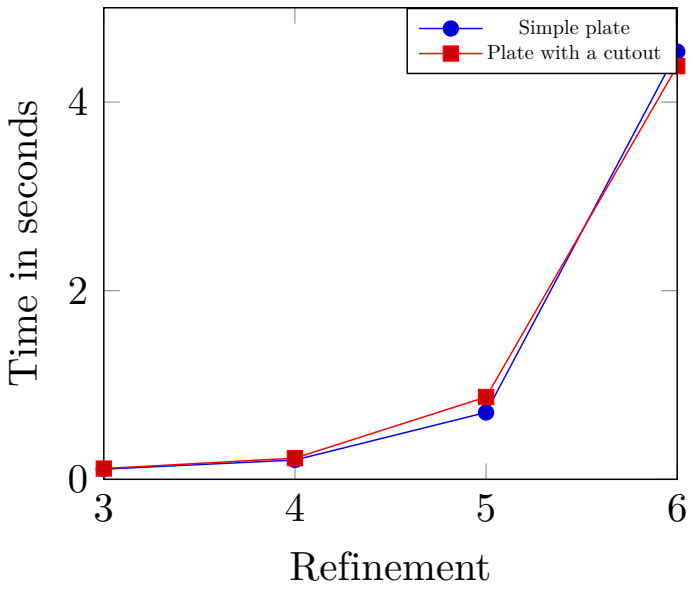

Figure 4.10: Variation in computational time (in seconds) with respect to refinement for eigenvalue analysis

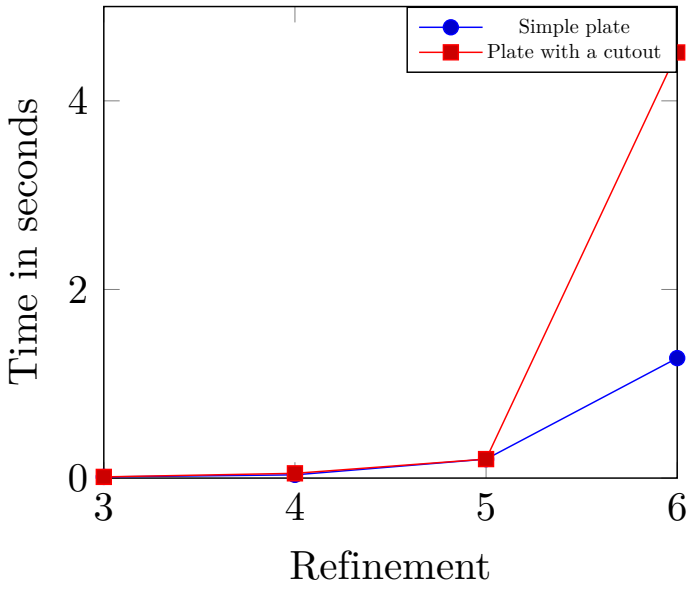

Figure 4.11: Variation in computational time (in seconds) with respect to refinement for static analysis

4.4 Convergence studies

Convergence studies on a stiffened plate with a cutout are not as straightforward as a simple plate problem since the size of the cutout, size of the stiffener and the plate meshes all affect the results. We consider a stiffened plate with a central circular cutout. The material properties, ply orientation and stiffener profile were the same as mentioned in Section 4.2.4. For convergence studies with respect to the increasing cutout size, an unstiffened plate was considered. It can be observed from Figure 4.12 that the rate of convergence becomes slower with an increase in the cutout radius.

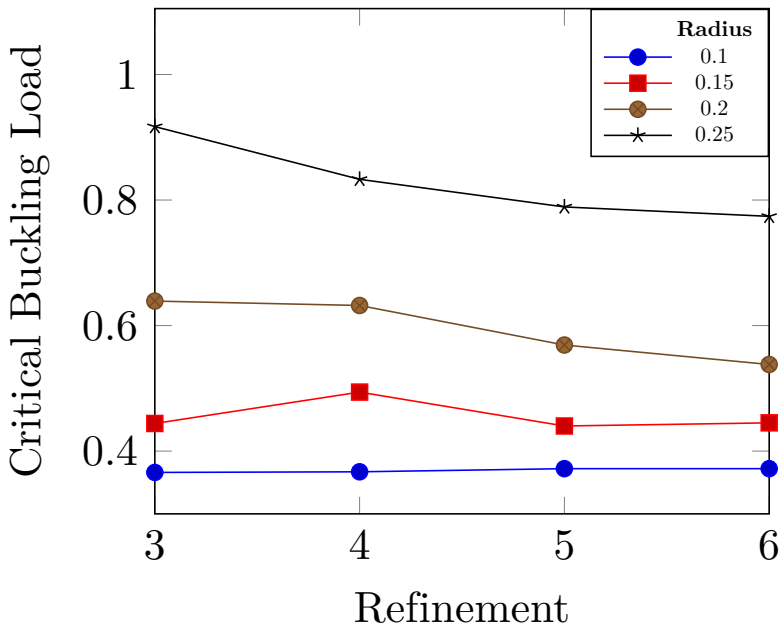

Figure 4.12: Variation of critical buckling load with respect to various plate mesh sizes for cutouts of increasing radii

Figures 4.13, 4.14 and 4.15 present the change of critical buckling loads with respect to various stiffener and plate mesh sizes for cutouts of varying radii. It is observed that for cutouts with relatively smaller radius (0.15 and 0.2), for each refinement levels of the plate mesh, the results converge for the 4^{th} order of refinement of the stiffener mesh. It is also observed that the plate mesh density has a higher influence on the results compared to the stiffener mesh density. However, as the radius of the cutout is increased to 0.25, the stiffener mesh density impacts the convergence to a much higher degree (Figure 4.13).

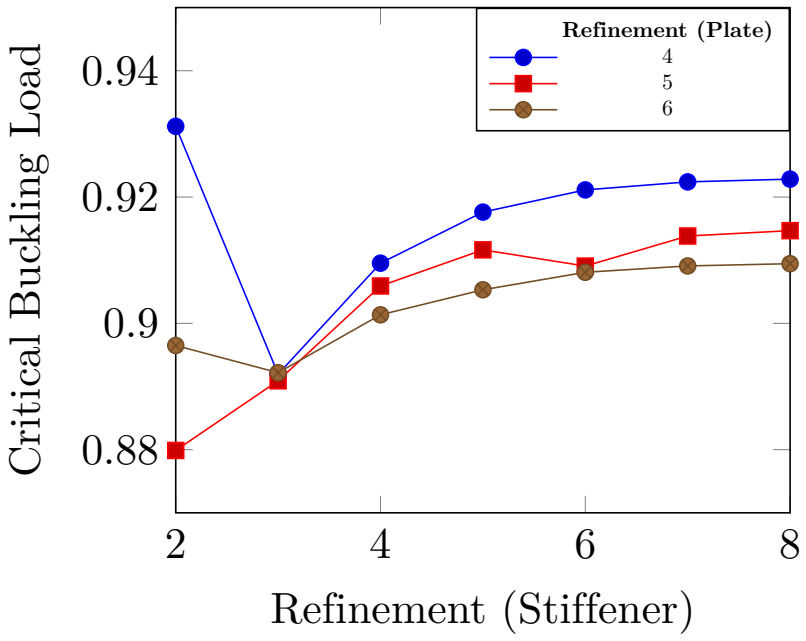

Figure 4.13: Variation of critical buckling load with respect to various stiffener and plate mesh sizes for $radius = 0.25$

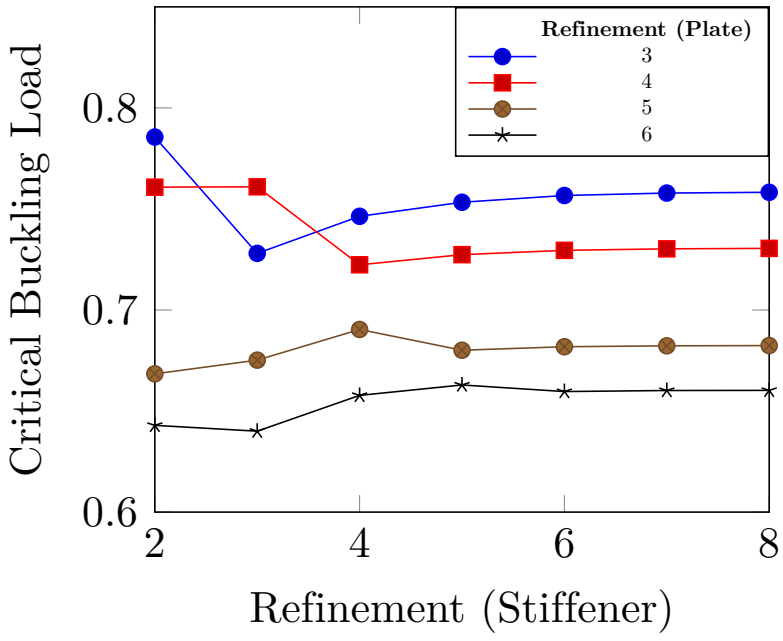

Figure 4.14: Variation of critical buckling load with respect to various stiffener and plate mesh sizes for $radius = 0.2$

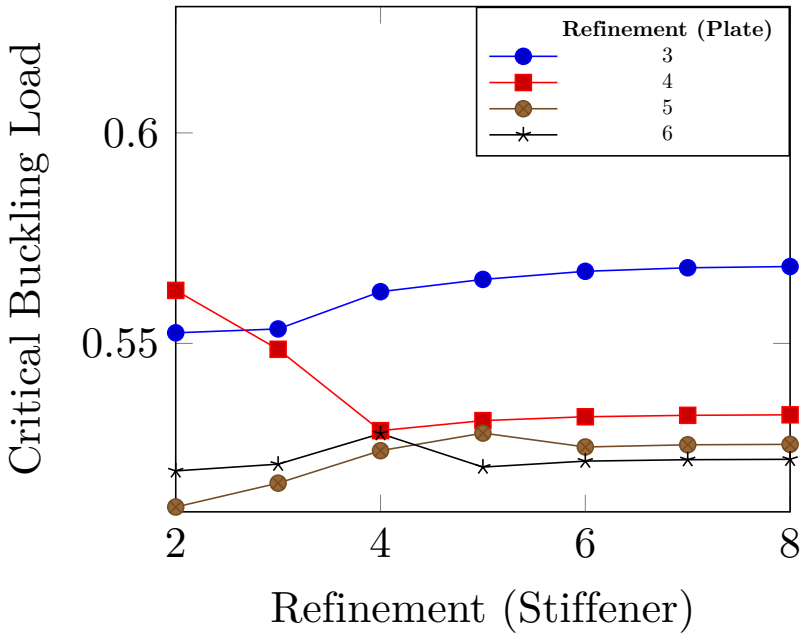

Figure 4.15: Variation of critical buckling load with respect to various stiffener and plate mesh sizes for $radius = 0.15$

Chapter 5

Vibration of Curvilinearly Stiffened Plate Using Isogeometric Analysis

5.1 Introduction

This chapter focuses on the isogeometric vibration analysis of curvilinearly stiffened composite panels. The stiffness matrices and the mass matrices are derived using the first-order shear deformation theory (FSDT). Cutouts are modeled using a single NURBS patch generated by creating a ruled surface between two curves. The proposed formulation is first validated by comparing it with available literature. The effects of width-to-thickness ratio, fiber orientation, ply layups, shape and size of the cutouts and the boundary conditions on the response of stiffened composite plates are then analyzed and the numerical results are used to derive useful conclusions.

5.1.1 Mathematical Foundation

In the first-order shear deformation theory (FSDT) the displacement field is considered as the first-order Taylor expansion of mid-plane variables with respect to plate thickness as follows:

Consider a stiffened composite panel as shown in Figure 5.1. The mid-plane of the panel O_{xy} the global coordinate system. The plate is assumed to have a uniform thickness with no plydrops. Let u be the displacements in the x-axis and v be the in-plane displacements along the y-axis. Let w be the transverse deflection along the z-axis.

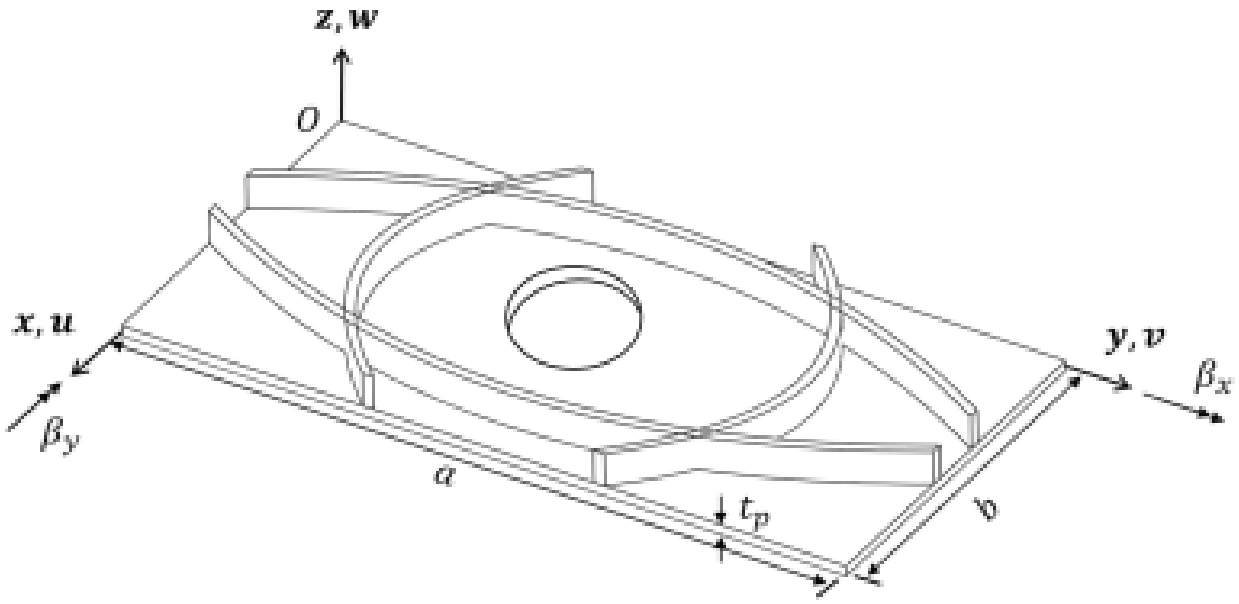

Figure 5.1: Geometry and nomenclature of a stiffened composite panel with a central cutout. Redrawn and modified from [1]

Let β_y and β_x be rotation components of the panel around the x- and y-axes, respectively. The displacement components of the panel is defined by the first-order shear-deformable theory as follows,

$$\begin{aligned} u\,(x,y,z,t) &= u_0\,(x,y,z,t) + z\beta_x\,(x,y,t) \\ v\,(x,y,z,t) &= v_0\,(x,y,z,t) + z\beta_y\,(x,y,t) \\ w\,(x,y,z,t) &= w_0\,(x,y,z,t) \end{aligned} \tag{5.1}$$

The plate strain energy U_p can be written as,

$$U_p = \frac{1}{2} \int\int_{\Omega} \boldsymbol{\varepsilon}_{\mathbf{p}}^{\mathbf{LT}} \mathbf{D_p} \boldsymbol{\varepsilon}_{\mathbf{p}}^{\mathbf{L}} \mathrm{d}\Omega \tag{5.2}$$

Where, $\mathbf{D}_p$ depends on the material property, stacking sequence, ply orientation and thickness of the plate. Derivation of $\mathbf{D}_p$ is explained in Section 3.2.2. The generalized strains ε_p and the generalized displacements $\mathbf{u_p}$ of the panel can be written as,

$$\boldsymbol{\varepsilon}_{\mathbf{p}}^{\mathbf{L}} = \begin{Bmatrix} \varepsilon_x^0 \\ \varepsilon_y^0 \\ \gamma_{xy}^0 \\ \kappa_x^0 \\ \kappa_y^0 \\ \kappa_{xy}^0 \\ \gamma_{xz}^0 \\ \gamma_{yz}^0 \end{Bmatrix} = \begin{bmatrix} \frac{\partial}{\partial x} & 0 & 0 & 0 & 0 & 0 \\ 0 & \frac{\partial}{\partial x} & 0 & 0 & 0 & 0 \\ \frac{\partial}{\partial x} & \frac{\partial}{\partial x} & 0 & 0 & 0 & 0 \\ 0 & 0 & 0 & 0 & \frac{\partial}{\partial x} & 0 \\ 0 & 0 & 0 & 0 & 0 & \frac{\partial}{\partial x} \\ 0 & 0 & 0 & 0 & \frac{\partial}{\partial x} & \frac{\partial}{\partial x} \\ 0 & 0 & 0 & \frac{\partial}{\partial x} & 1 & 0 \\ 0 & 0 & 0 & \frac{\partial}{\partial x} & 0 & 1 \end{bmatrix} \begin{Bmatrix} u_0 \\ v_0 \\ w_0 \\ \beta_x \\ \beta_y \end{Bmatrix} = \mathbf{B_p u_p} \tag{5.3}$$

The panel strain energy U_p for the composite panel is,

$$U_p = \frac{1}{2} \iint_{\Omega} \mathbf{u_p}^T \mathbf{B_p}^T \mathbf{D_p} \mathbf{B_p} \mathbf{u_p} d\Omega \tag{5.4}$$

The kinetic energy T_p for the composite panel is,

$$T_p = \frac{1}{2}\iint_{\Omega} \dot{\mathbf{u}}_p^T m_p \dot{\mathbf{u}}_p d\Omega \tag{5.5}$$

Where,

$$\mathbf{m_p} = \rho \begin{pmatrix} t & 0 & 0 & 0 & 0 \\ 0 & t & 0 & 0 & 0 \\ 0 & 0 & t & 0 & 0 \\ 0 & 0 & 0 & t^2/12 & 0 \\ 0 & 0 & 0 & 0 & t^2/12 \end{pmatrix} \tag{5.6}$$

5.1.2 Modeling of curvilinear stiffener

The modeling of stiffener for free vibration analysis follows the same procedure as Section 3.2.3. The stiffener strain energy U_s is written as:

$$U_s = \frac{1}{2}\int_{\Gamma} \varepsilon_{\mathbf{s}}^{\mathbf{LT}} \mathbf{D_s} \varepsilon_{\mathbf{s}}^{\mathbf{L}} \mathrm{d}\Gamma \tag{5.7}$$

The strain displacement relation of the composite stiffener is [98],

$$\varepsilon_{\mathbf{s}} = \begin{Bmatrix} \varepsilon_t^0 \\ \gamma_n^0 \\ \gamma_b^0 \\ \kappa_t^0 \\ \kappa_n^0 \end{Bmatrix} = \begin{bmatrix} \frac{d}{dt} & \frac{1}{R} & 0 & 0 & 0 \\ -\frac{1}{R} & \frac{d}{dt} & 0 & 0 & 0 \\ 0 & 0 & \frac{d}{dt} & 1 & 0 \\ 0 & 0 & 0 & \frac{d}{dt} & \frac{1}{R} \\ 0 & 0 & 0 & -\frac{1}{R} & \frac{d}{dt} \end{bmatrix} \begin{Bmatrix} u_t \\ v_n \\ w_b \\ \beta_t \\ \beta_n \end{Bmatrix} = \mathbf{B_s u_s} \tag{5.8}$$

where $\frac{1}{R}$ is the geometric curvature of the stiffener, computed at the integration points. Substituting Equation 5.8 into Equation 5.7 we get,

$$U_s = \frac{1}{2} \int_{\Gamma} \mathbf{u_s^T B_s^T D_s B_s^L u_s} \mathrm{d}\Gamma, \tag{5.9}$$

The $\boldsymbol{D}_s$ in the above strain energy equation is the rigidity matrix for the composite stiffener and is given by,

$$\begin{pmatrix} E_s A & 0 & 0 & E_s A e & 0 \\ 0 & G_s A_n & 0 & 0 & G_s A_n e \\ 0 & 0 & G_s A_b e & 0 & 0 \\ E_s A e & 0 & 0 & E_s I_n & 0 \\ 0 & G_s A_n e & 0 & 0 & G_s J_t \end{pmatrix} \tag{5.10}$$

The kinetic energy for the stiffener T_s is

$$T_s = \frac{1}{2}\int_{\Gamma} \dot{\mathbf{u}}_s^T m_s \dot{\mathbf{u}}_s d\Gamma \tag{5.11}$$

where m_s is the stiffener mass matrix and is given as,

$$m_s = \rho_s \begin{bmatrix} A & 0 & 0 & Ae & 0 \\ 0 & A & 0 & 0 & Ae \\ 0 & 0 & A & 0 & 0 \\ Ae & 0 & 0 & I_n & 0 \\ 0 & Ae & 0 & 0 & I_n + I_b \end{bmatrix} \tag{5.12}$$

Before building the linear system of equation of the stiffened plate, the degrees of freedom of the plate and curvilinear stiffener should be unified. Detailed steps to achieve this are as follows :

- First, the plate and the stiffener are meshed independently and the location of the stiffener control points is identified. Take Figure 5.2 for instance, where the control point A belongs to the plate element k.

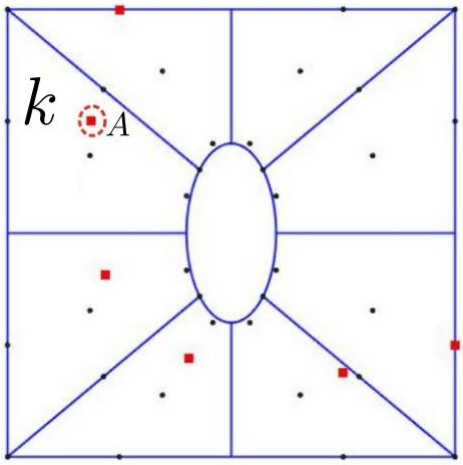

Figure 5.2: Mesh plot of the curvilinearly stiffened plate in the physical space.

We can compute the natural coordinates $(\bar{\xi}, \bar{\eta})$ of the stiffener control point in the plate element by solving Equation 5.13 since the stiffener and the plate control points are known.

$$\mathbf{r_s} \mid_A = \sum_{j=1}^{4} R_j(\bar{\xi}_A, \bar{\eta}_A)\mathbf{x_{p}}_j \mid_k . \tag{5.13}$$

- Since the natural coordinates are not obtained, the displacement of the stiffener is:

$$\mathbf{u_s} \mid_A = \sum_{j=1}^{4} R_j(\bar{\xi}_A, \bar{\eta}_A)\mathbf{u_{p}}_j \mid_k . \tag{5.14}$$

- The displacements of any points in the stiffener element can be expressed as:

$$\mathbf{u_{sg}} = \sum_{j=A} R_j(\varsigma)\mathbf{u_s}_j. \tag{5.15}$$

- Then, substituting Equation 5.14 into Equation 5.15 results in the following equation:

$$\mathbf{u_{sg}} = \sum_{j=A} R_j(\varsigma) \sum_{i=1}^{4} R_i(\bar{\xi}_j, \bar{\eta}_j)\mathbf{u_{p}}_i \mid_k \tag{5.16}$$

- Rewriting the displacement approximations in a matrix form,

$$\mathbf{u_{sg}} = \mathbf{N}_{ps}\mathbf{u_p} \mid_k . \tag{5.17}$$

- Now the displacement $\mathbf{u}_{sg}$ are described in the global coordinate system. Hence the stiffener displacements should be transformed to the local curvilinear coordinate system. The transformation matrix is:

$$\mathbf{T} = \begin{pmatrix} \cos\alpha & \sin\alpha & 0 & 0 & 0 \\ -\sin\alpha & \cos\alpha & 0 & 0 & 0 \\ 0 & 0 & 1 & 0 & 0 \\ 0 & 0 & 0 & \cos\alpha & \sin\alpha \\ 0 & 0 & 0 & -\sin\alpha & \cos\alpha \end{pmatrix}, \tag{5.18}$$

where α is the angle between the stiffener tangential direction t-axis and x-axis of the global coordinate system, whose value is calculated at each integration point.

$$\alpha = tan^{-1}\left(\frac{y'}{x'}\right) \tag{5.19}$$

The prime ' denotes the first derivative with respect to the stiffener arc length, $d()/d\Gamma$.

Hence, the stiffener strain energy U_s and the kinetic energy T_s can be rewritten as,

$$U_s = \frac{1}{2}\int \mathbf{u_p^T N_{ps}^T T^T B_s^{LT} D_s B_s^L T N_{ps} u_p} \mathrm{d}\Gamma, \tag{5.20}$$

$$T_s = \frac{1}{2}\int \mathbf{\dot{u}_p^T N_{ps}^T T^T m_s T N_{ps} \dot{u}_p} \mathrm{d}\Gamma, \tag{5.21}$$

Hamilton's principle can now be used in deriving the weak form of the governing equation.

$$\int_{t_1}^{t_2} [(\delta U_p + \delta U_s) - (\delta T_p + \delta T_s)] \mathrm{d}t = 0, \tag{5.22}$$

where t_1 and t_2 are the initial and final times, respectively. The principle expression is:

$$\int_{t_1}^{t_2} \left[\begin{array}{c} \int\int_\Omega \delta \mathbf{u_p^T (B_p^{LT} D_p B_p^L) u_p} \mathrm{d}\Omega + \int \delta \mathbf{u_p^T (N_{ps}^T T^T B_s^{LT} D_s B_s^L T N_{ps}) u_p} \mathrm{d}\Gamma \\ - \int\int_\Omega \delta \mathbf{u_p^T m_p \ddot{u}_p} \mathrm{d}\Omega - \int \delta \mathbf{u_p^T (N_{ps}^T T^T m_s T N_{ps}) \ddot{u}_p} \mathrm{d}\Gamma \end{array} \right] \mathrm{d}t = 0. \tag{5.23}$$

5.2 Results and Discussion

To demonstrate and validate the method, free vibration analysis of several plates with different curvilinear stiffeners were carried out. Results are compared with existing literature

for some cases while for some others, using commercially popular software like ABAQUS. Parametric studies were performed which show the influence of both the cutout profile and the shape and position of the curvilinear stiffeners in the results.

5.2.1 Isotropic plate with a circular hole at the center

In order to illustrate the performance of IGA code in modeling holes, an isotropic plate with a circular hole at the center was considered. The plate is assumed to have side length of 10 m and a thickness of 0.1 m. The hole has a radius of 1 m,.

$$SSSS: \begin{cases} u_0 = v_0 = w_0 = \phi_y = \phi_z = 0 \quad \text{on } x = 0,\ a \\ u_0 = v_0 = w_0 = \phi_x = \phi_z = 0 \quad \text{on } y = 0,\ b \end{cases} \tag{5.24}$$

The material properties are :

$$E = 208\ GPa,\ \nu = 0.3,\ \rho = 8,000 kg/m^2 \tag{5.25}$$

A normalized frequency parameter is defined by $\widetilde{\omega} = [\rho h \omega^2 a^4 / D(1-v^2)]^{1/4}$ with $D = Eh^3/12(1-v^2)$.

The first eight frequencies obtained by the current method are shown in Table 5.1. These results are compared against reference solutions in [110], [54]. The results are seen to be in good agreement with the reference solution.

Table 5.1: Normalized frequencies of clamped square plate with a circular hole.

Mode	**This work**	[110]	[54]
1	6.183	6.24	6.149
2	8.657	8.457	8.577
3	8.657	8.462	8.634
4	10.513	10.233	10.422
5	11.559	11.719	11.414
6	12.052	12.299	11.838
7	13.022	13.037	12.829
8	13.022	13.041	12.842

5.2.2 Isotropic plate with a complicated cutout

The present method is applied to analyze an isotropic plate with a heart shaped cutout (Figure 3.9). The thickness of the plate is $h = 0.05$m and the material parameters are

$$E = 200\ GPa,\ \nu = 0.3,\ \rho = 8000\ kg/m^3 \tag{5.26}$$

Shojaee et al. [2] analyzed the same geometry using IGA and classical laminate theory with multiple patches. The bending strip method was used to achieve compatibility between adjacent patches. In this work, the first order shear deformation theory was used and the plate was modeled with a single NURBS patch thus eliminating the use of multiple NURBS patches.

The normalized frequencies obtained using the present method are compared against some results from existing literature [2], MKI method [111], radial point interpolation method [112] and Element Free Galerkin method [113]. The results can be seen in good agreement

Table 5.2: Normalized natural frequencies of a simply supported plate with a heart shaped complicated cutout.

Mode	MultiPatch	MKI	EFG	RIPM	ABAQUS	Present
1	5.193	5.39	5.453	4.919	4.948	4.945
2	6.579	7.502	8.069	6.398	6.426	6.441
3	6.597	8.347	9.554	6.775	6.796	6.804
4	7.819	10.636	10.099	8.613	8.616	8.585
5	8.812	11.048	11.328	9.016	9.020	9.031
6	9.42	12.894	12.765	10.738	10.720	10.670
7	10.742	13.71	13.685	10.93	10.966	10.908
8	10.776	14.062	14.305	11.601	11.686	11.661
9	11.919	16.649	15.721	12.903	12.901	12.833
10	13.2	17.364	17.079	13.283	13.238	13.185

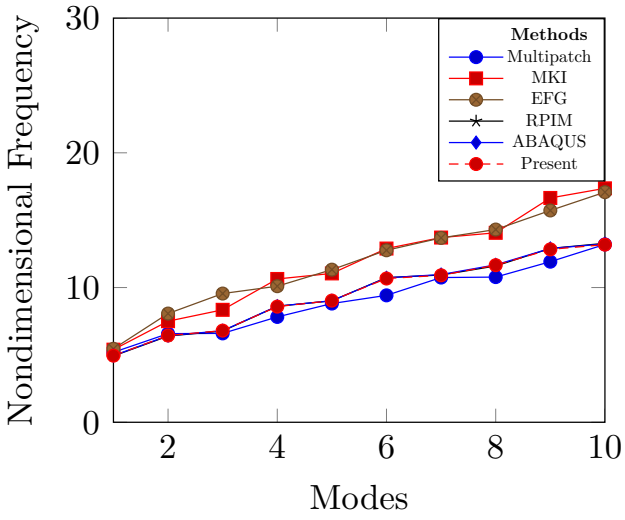

Figure 5.3: Normalized natural frequencies of a simply supported plate with a heart shaped complicated cutout.

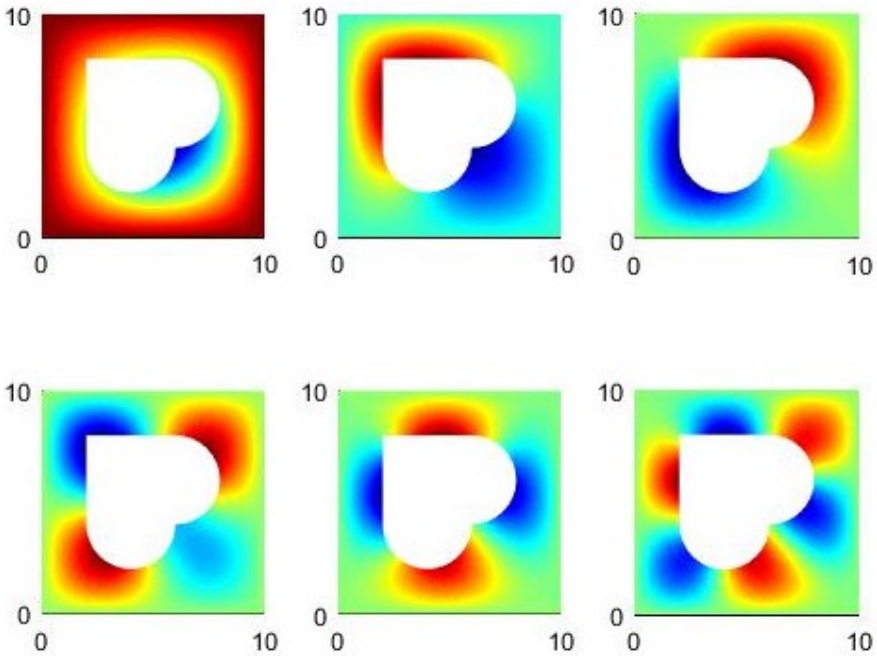

Figure 5.4: First six modes (IGA) of a simply supported square plate with a complicated cutout

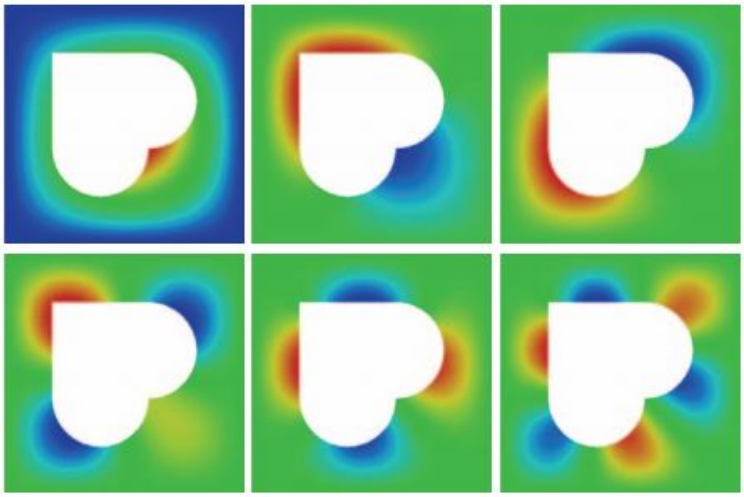

Figure 5.5: First six modes [2] of a simply supported plate with a heart shaped complicated cutout

with the reference solutions for the simply supported boundary condition. As opposed to [2], the current method obviates the necessity to use the bending strip methods for patch coupling. The overall computational cost required is hence reduced significantly.

5.2.3 Vibration of a Composite plate with a heart shaped cutout

A three-layered symmetric crossply laminated composite plate is considered Figure 3.9. The ratio of elastic constants are as follows:

$$E_L/E_T = 2.45,\ G_{LT}/E_T = 0.48,\ G_{TT}/E_T = 0.2,\ \nu_{LT} = 0.23 \tag{5.27}$$

mass density = 8,000 kg/m^3 and thickness $h = 0.06m$. The frequency is normalized using $\widetilde{\omega} = [\rho h \omega^2 a^4/D_{0.1}]^{1/2}$, with a=10m and $D_{0.1} = E_1 h^3/12(1 - v_{12}v_{21})$. The results were obtained for simply supported (SSSS) boundary condition.

$$SSSS: \begin{cases} u_0 = v_0 = w_0 = \phi_y = \phi_z = 0 \quad \text{on } x = 0,\ a \\ u_0 = v_0 = w_0 = \phi_x = \phi_z = 0 \quad \text{on } y = 0,\ b \end{cases} \tag{5.28}$$

The results were obtained for simply supported (SSSS) boundary conditions. The first six normalized frequencies of this model for various angle ply fiber orientations are presented in Table 5.3. The present solutions are compared with the results obtained by IGA and Kirchhoff theory with eight patches [2], EFG and MKI methods [111]. It can be observed that the present method delivers very good results which are in agreement with results from

published literature for considered angle ply orientations.

Table 5.3: Normalized natural frequencies of a simply supported laminated plate with a heart shaped cutout for various angle ply orientations.

Angle ply	Method	Mode					
		1	2	3	4	5	6
(15°/ −15°/ 15°)	This work	18.91	31.83	36.09	57.00	62.73	83.93
	IGA with 8-patches[2]	18.91	32.05	36.00	56.35	63.37	83.63
	EFG[111]	19.18	32.45	37.24	58.72	63.99	86.50
	MKI[111]	18.32	31.47	37.62	63.08	66.54	86.49
(30°/ −30°/ 30°)	This work	20.40	33.66	37.23	59.20	65.03	87.92
	IGA with 8-patches[2]	20.32	33.93	37.07	58.48	65.90	87.97
	EFG[111]	20.93	34.92	39.10	62.22	67.05	92.72
	MKI[111]	20.31	33.99	39.90	58.11	69.70	92.10
(45°/ −45°/ 45°)	This work	21.10	34.45	37.91	60.29	66.22	90.68
	IGA with 8-patches[2]	20.98	34.85	37.56	59.33	67.52	91.22
	EFG[111]	21.74	36.08	39.98	63.90	68.53	96.77
	MKI[[111]	20.99	34.90	39.27	63.38	69.02	96.59

5.2.4 Curvilinearly stiffened composite panels with central circular cutout

In this section, the influence of central cutouts on clamped stiffened composite panels is studied.

$$Clamped: \ u_0 = 0, v_0 = 0, \psi_x = 0, \psi_y = 0, w_0 = 0 \tag{5.29}$$

on all four edges. The stiffener is assumed to be fabricated from isotropic material with Young's modulus = E_T, Poisson's ratio = ν_{LT} and coefficient of thermal expansion = α_0. The stiffness ratio $\gamma = EI/bD$ and the area ratio $\delta = A_s/bt_p$ are 5 and 0.1 respectively, unless

specified otherwise. The ratio of elastic constants are as follows:

$$E_L/E_T = 15,\ G_{LT}/E_T = 0.5,\ G_{TT}/E_T = 0.3356,\ \nu_{LT} = 0.3 \tag{5.30}$$

mass density = 8,000 kg/m^3 and thickness $h = 0.01\ m$. The frequency is normalized using $\widetilde{\omega} = [\rho h \omega^2 a^4/D_{0.1}]^{1/2}$, with a=1 m and $D_{0.1} = E_1 h^3/12(1 - v_{12}v_{21})$. To check the accuracy of the displacement compatibility algorithm, results for clamped curvilinearly stiffened composite plate are compared with those obtained using ABAQUS. The curvilinear stiffener configuration was adopted from [105] and scaled proportionally to match the dimensions of the plate. From the ABAQUS library, the plate was meshed using 2040 S8R elements and curvilinear stiffener was meshed using 192 elements S8R elements (48 divisions along the arc length and 4 divisions along the depth direction). The IGA plate model was meshed using 1024 elements and the curvilinear stiffener using 32 elements. The normalized fundamental frequency was observed to converge for these mesh configurations. The first five eigenmodes were extracted for this case. The eigenmode plots obtained using the IGA approach are similar to the ones obtained using ABAQUS as can be seen from Figure 5.6.

	Present		ABAQUS	
Mode		$\widetilde{\omega}$		$\widetilde{\omega}$
1	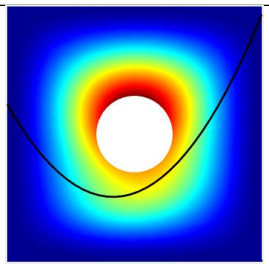	26.839	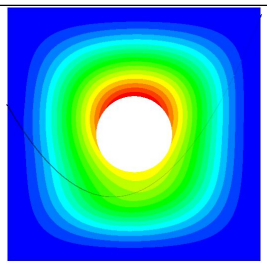	26.215
2	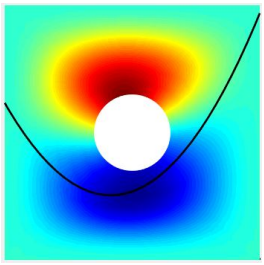	35.683	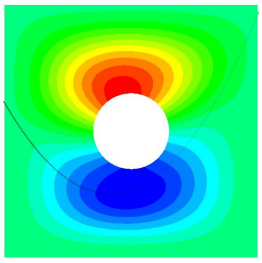	34.956
3	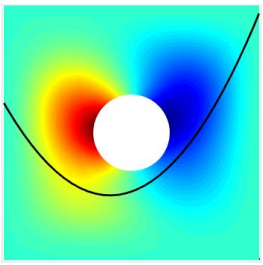	52.254	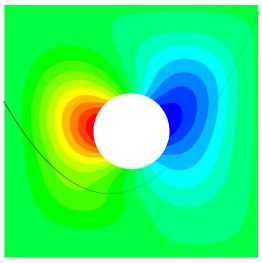	50.876
4	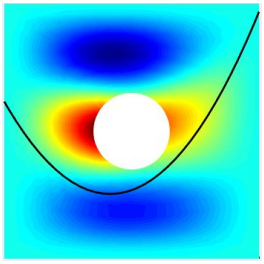	65.551	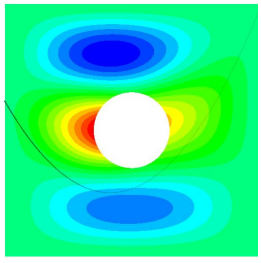	64.421
5	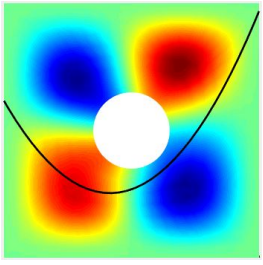	69.485	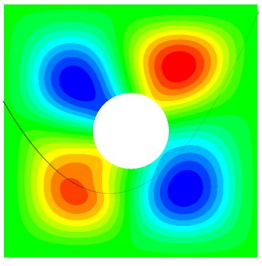	67.907

Figure 5.6: The first five eigenmode shape plots for a plate with curvilinear stiffener using a IGA and ABAQUS, a commercial available software.

5.2.5 Curvilinearly stiffened composite panels with an elliptical central cutout

In this section, results of curvilinearly stiffened composite panels with elliptical cutouts are presented. The ratio of elastic constants are as follows:

$$E_L/E_T = 15,\ G_{LT}/E_T = 0.5,\ G_{TT}/E_T = 0.3356,\ \nu_{LT} = 0.3 \tag{5.31}$$

mass density = 8,000 kg/m^3 and thickness $h = 0.01\ m$. The frequency is normalized by $\widetilde{\omega} = [\rho h\omega^2 a^4/D_{0.1}]^{1/2}$, with a=1 m and $D_{0.1} = E_1 h^3/12(1 - v_{12}v_{21})$. The results were obtained for clamped boundary condition.

An ellipse of semi-major axis = 0.2 m and semi-minor axis = 0.1 m is considered for all cases. The normalized first ten frequencies of a stiffend four layer composite laminate plate with respect to ply orientations, stiffness ratios and different stiffener profiles (defined by $\Delta\epsilon$ Figure 3.11) are presented in Table 5.5 and Table 5.6 and their fifth mode shapes are shown in Figures 5.5, 5.6, 5.7, 5.8, 5.9 and 5.11.

Table 5.5: Normalized frequencies for different ply orientations for $\gamma = 5$ and $\Delta\epsilon = 0$

Mode	**Antisymmetric Crossply**	**Symmetric Crossply**	**Symmetric Angleply**	**Antisymmetric Angleply**
1	23.986	25.407	23.572	23.582
2	38.356	34.523	37.198	38.044
3	44.347	47.911	39.978	42.451
4	61.730	60.599	60.905	64.111
5	76.728	64.747	71.808	73.009
6	84.472	77.037	80.460	76.987
7	92.642	88.814	86.570	83.375
8	97.597	100.505	88.596	100.486
9	113.239	112.436	106.260	110.241
10	131.673	117.184	114.723	115.131

Table 5.6: Normalized frequencies for different ply orientations for $\gamma = 5$ and $\Delta\epsilon = 0.25$

Mode	**Antisymmetric Crossply**	**Symmetric Crossply**	**Symmetric Angleply**	**Antisymmetric Angleply**
1	25.733	26.909	24.646	25.235
2	37.732	35.836	36.676	37.132
3	48.315	49.624	43.724	47.161
4	69.413	61.422	68.170	69.795
5	74.287	73.238	70.369	70.890
6	90.708	85.848	87.059	84.483
7	97.896	94.369	92.601	91.590
8	112.175	106.567	100.993	110.461
9	116.899	120.171	109.681	112.065
10	134.109	126.330	116.890	124.329

Table 5.7: Normalized frequencies for different ply orientations for $\gamma = 10$ and $\Delta\epsilon = 0$

Mode	**Antisymmetric Crossply**	**Symmetric Crossply**	**Symmetric Angleply**	**Antisymmetric Angleply**
1	24.558	25.884	24.338	24.204
2	39.728	35.893	38.942	39.532
3	44.829	48.349	40.774	42.883
4	63.772	62.179	62.164	65.975
5	78.058	66.348	73.699	74.667
6	86.129	79.246	81.491	77.525
7	92.842	89.915	87.746	83.964
8	99.651	100.505	88.801	101.741
9	114.029	112.995	108.705	111.953
10	134.182	119.439	115.836	118.263

Table 5.8: Normalized frequencies for different ply orientations for $\gamma = 10$ and $\Delta\epsilon = 0.25$

Mode	**Antisymmetric Crossply**	**Symmetric Crossply**	**Symmetric Angleply**	**Antisymmetric Angleply**
1	27.711	28.829	26.494	27.386
2	39.709	38.489	38.548	38.691
3	52.994	51.992	48.197	52.150
4	74.603	65.702	71.611	72.942
5	77.687	79.184	76.178	74.211
6	93.429	89.734	89.045	87.193
7	102.543	98.080	95.125	99.094
8	115.133	111.041	107.583	113.098
9	126.002	121.882	113.833	114.182
10	137.331	133.214	124.795	139.792

Table 5.9: The fifth mode shape plots for different ply orientations for $\gamma = 5$ and $\Delta\epsilon = 0$

Antisymmetric Crossply	**Symmetric Crossply**
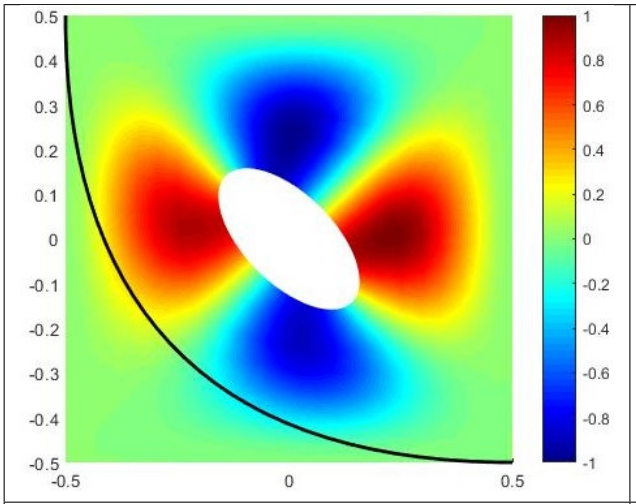	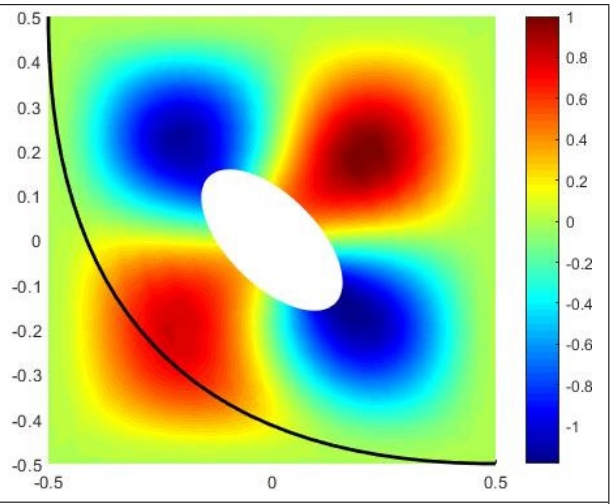
Symmetric Angleply	**Antisymmetric Angleply**
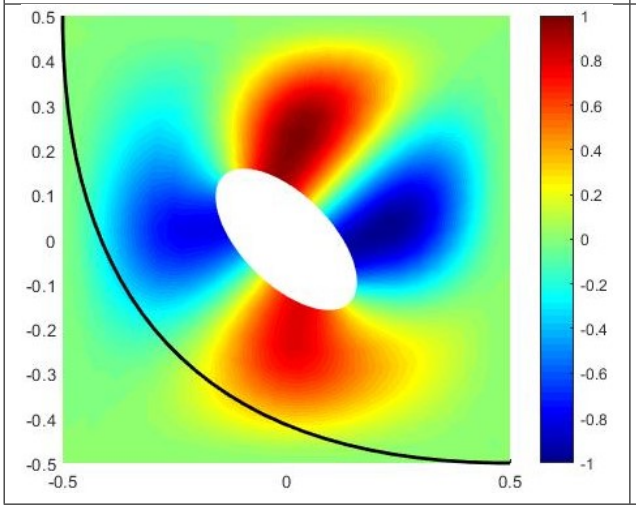	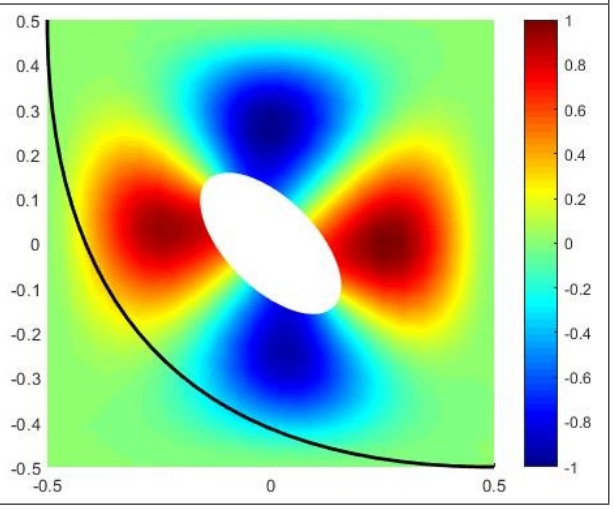

Table 5.10: The fifth mode shape plots for different ply orientations for $\gamma = 5$ and $\Delta\epsilon = 0.25$

Antisymmetric Crossply	**Symmetric Crossply**
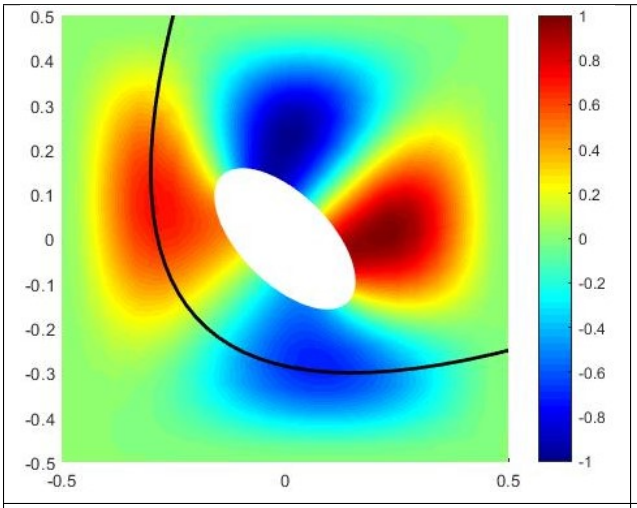	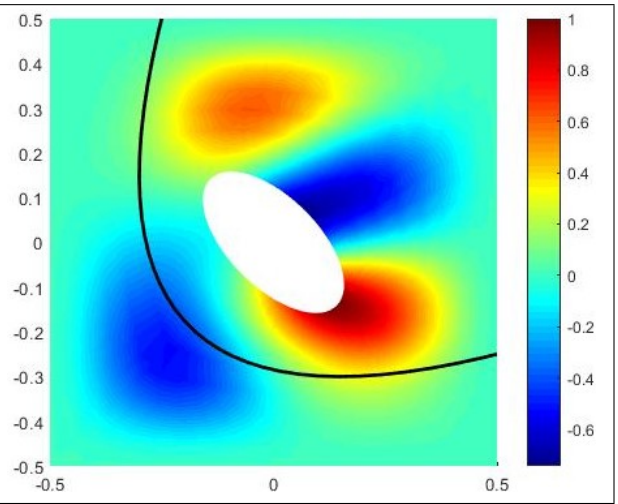
Symmetric Angleply	**Antisymmetric Angleply**
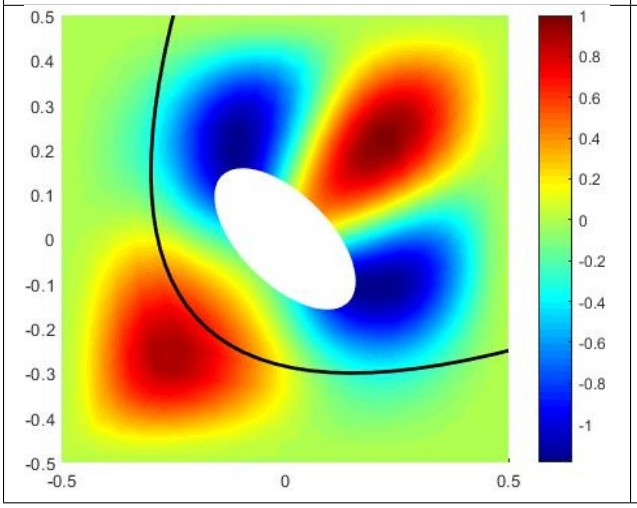	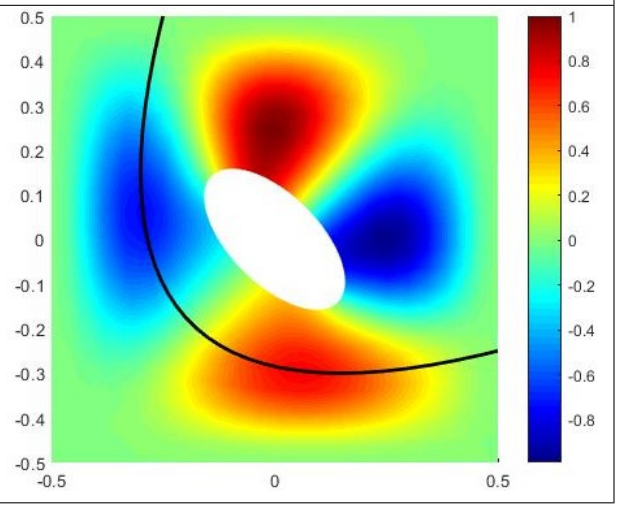

Table 5.11: The fifth mode shape plots for different ply orientations for $\gamma = 10$ and $\Delta\epsilon = 0$

Antisymmetric Crossply	**Symmetric Crossply**
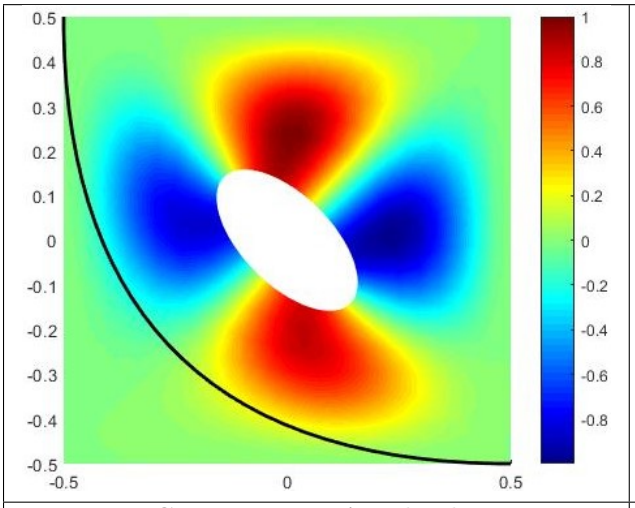	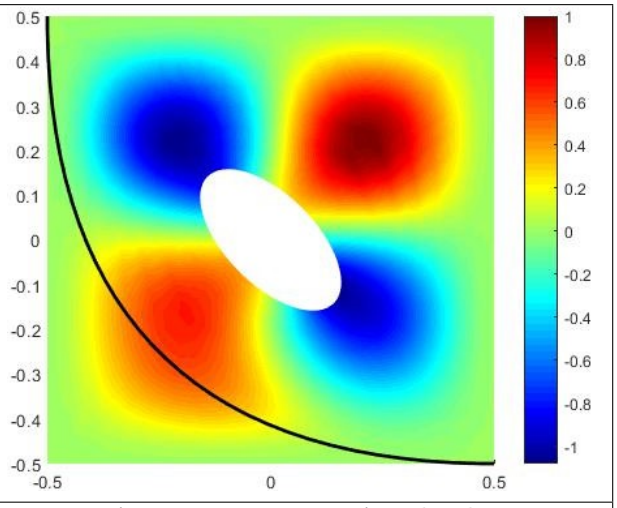
Symmetric Angleply	**Antisymmetric Angleply**
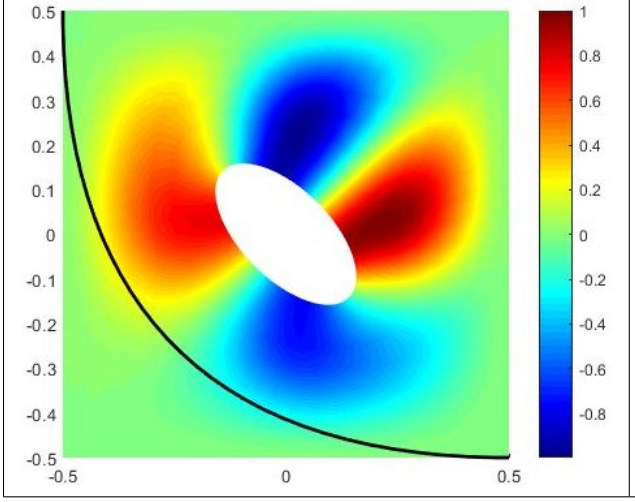	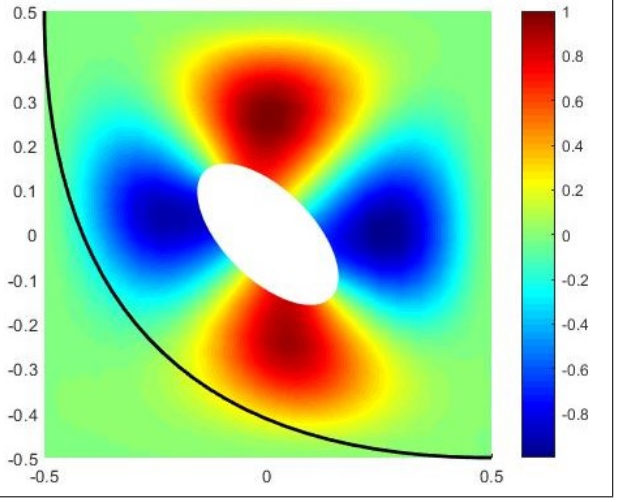

Table 5.12: The fifth mode shape plots for different ply orientations for $\gamma = 10$ and $\Delta\epsilon = 0.25$

Antisymmetric Crossply	**Symmetric Crossply**
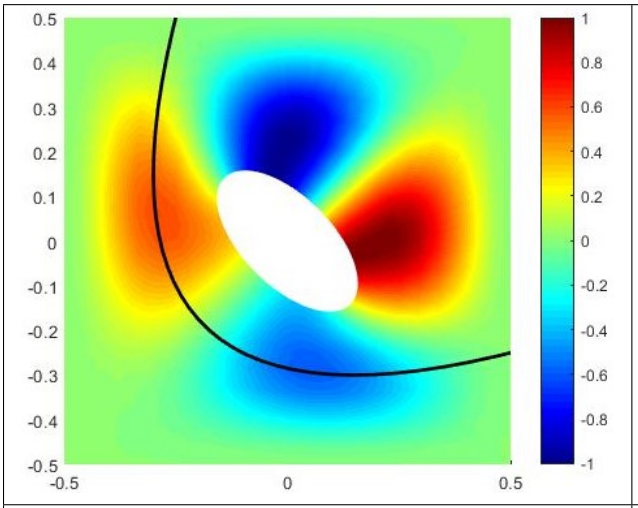	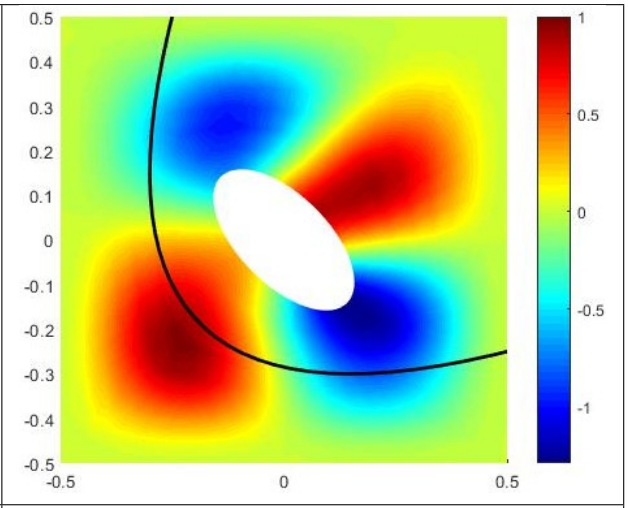
Symmetric Angleply	**Antisymmetric Angleply**
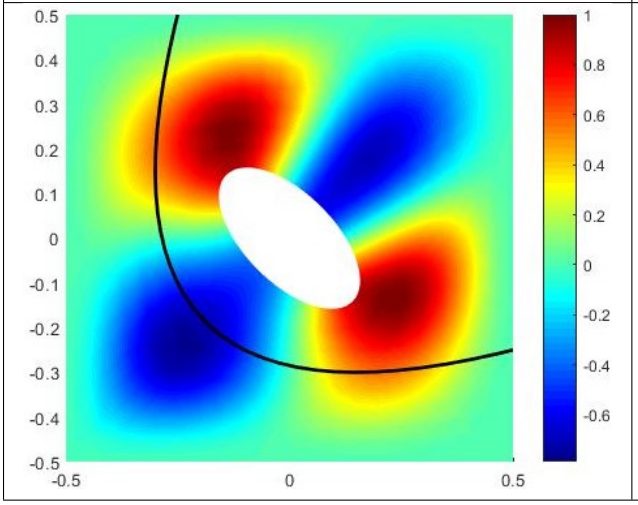	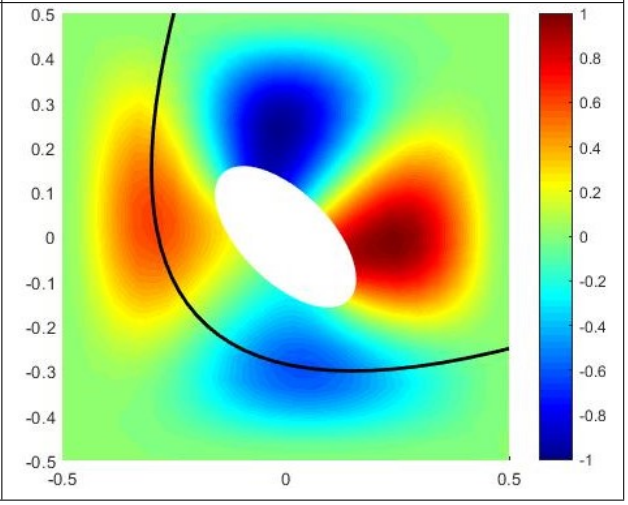

This chapter discusses the vibration analysis of curvilinearly stiffened plate with cutouts using a single NURBS patch. The efficiency of this method is described using numerical examples of laminated plates containing cutouts of various shapes and dimensions and for different boundary conditions, stiffener locations and curvature.

Chapter 6

Conclusions and Future work

This dissertation discusses the thermomechanical analyses performed on threaded fasteners and curvilinearly stiffened composite panels with internal cutouts.

Chapter 2 investigates two modeling techniques for the analysis of threaded connections : 1) a simplified model where the threads are reduced to smooth surfaces bonded to each other and 2) a detailed model where the threads' geometry is modeled as accurately as possible and frictional contacts are established between the surfaces of the threads to simulate the real behavior of this types of connection. The analysis shows that when only mechanical loads are applied the two techniques are able to assess the stresses with the same level of accuracy. In fact, there is little to no difference between the two approaches. On the other hand, if thermal loads are applied to the junction, there is a substantial difference in the predicted results. In particular, the first approach seems to over predict the stress value due to the strong constraint established by the bonded contact. In other words the model is over constrained in the vicinity of the thread interface. This problem does not appear if the second approach is implemented. In this case, the frictional contacts allow tangential slipping of the surfaces in contact relaxing the constraint and relieving the stresses at the

same time. From a feasibility and efficiency point of view the first approach is better than the second; in general, it requires lesser number of elements, lesser time to develop the model and less computational resources to solve. The two step global/local methodology proposed in this chapter shows the advantage in combining these two modeling techniques for the analysis of threaded joints subjected to thermo-mechanical load conditions. In this way it is possible to increase the efficiency of the first approach and at the same time achieve an accurate second approach by paying a small price for the computational resources.

In Chapter 3 NURBS isogeometric finite element analysis of stiffened laminated composite plates with cutouts is presented. The stiffened plate geometry with cutouts is modeled using NURBS basis functions. Furthermore, numerical results are presented for the thermal buckling response for various stiffener profiles, cutout dimensions and ply orientations. Available literature in this area of research was used to validate the code and the results were found to be in excellent agreement with them. A novel and efficient way of achieving displacement continuity between the stiffener and the plate is described. It was implemented by modifying the Newton-Raphson method using bounding boxes to compute the parametric coordinates given the coordinates of a particular control point of the stiffener in physical space. Complicated domain geometries were constructed by creating a ruled surface between the edge curves which greatly reduced the time to perform parametric studies. Building blocks of NURBS geometry construction like control points, knot vectors and associated weights are tabulated for various complicated shapes. Due to the implementation of FSDT, ensuring continuity between the patches using the bending strip method is avoided.

Chapter 4 discusses the level set method which requires very little computational effort to obtain a mesh independent description of the geometrical shape of a complicated cutout. The level sets discussed in that chapter are implemented in the form of a signed distance function which is both computationally inexpensive and easy to implement. Such an implementation is greatly useful since the tensor product nature of the NURBS basis functions only allows for global refinement and hence treating the trimmed objects such as internal cutouts is rather difficult. However, implementing the level set method obviates the use of trimmed NURBS surface to describe complex geometrical features like the cutouts. The efficiency of this method for thermal buckling analysis is described with the help of numerical examples for stiffened laminated plates containing complicated cutouts of various shapes and dimensions.

In Chapter 5 the isogeometric method has been successfully used for vibration analysis of a curvilinearly stiffened plate with cutouts using a single NURBS patch. The efficiency of this method is described with the help of numerical examples for stiffened laminated plates containing complicated cutouts of various shapes and dimensions and for different boundary conditions, stiffener locations and curvature. Modeling complicated cutout shapes using a single NURBS patch show that the results are in excellent agreement with those obtained using state of the art methods.

The following work can be further conducted in the future:

- The code can be easily modified and improved to capture the behaviour of variable-stiffness composite panels.

- The computational ease of performing an IGA can be used for multidisciplinary optimization problems resulting in weight reduction and enhancing structural capability of stiffened composite panels.
- The code can be further extended to capture the behaviour of microvascular carbon fiber/epoxy composites which increasingly represent a new class of strong, lightweight, thermally responsive structures for thermal management applications. The addition of microvascular channels also has the potential to improve and control the crashworthiness of carbon/epoxy composites
- Modeling material interfaces as fictitious domain is one of the many approaches available for crack propagation problems. In the context of Isogeometric analysis multiple material interfaces such as plate with an inclusion can be implemented easily by treating them as a multi-patch domain and coupling the interface constraints either through strong enforcement or through weak enforcement (Nitsche's method). This way of modeling of interfaces give much more freedom with respect to exactly tracing the interface boundaries.

6.1 Appendix A : MATLAB code to compute parametric coordinate of a point in physical space

This section contains the MATLAB code to compute the parametric coordinate of a point in physical space

```
function u = nrbreverse (nrb, x, varargin)
%
% nrbreverse: compute parametric point starting from physical point by
% inverting the NURBS map with a Newton scheme
%
% Calling Sequence:
%
%   u = nrbreverse (nrb, x)
%   u = nrbreverse (nrb, x, options)
%
%    INPUT:
%
%      nrb     - NURBS object
%      x       - physical point
%      options - options in the FIELD/VALUE format. Possible choices:
%        'u0'      : starting point in the parametric domain for Newton
```

```
17 %                     (Default = .5 * ones (ndim, 1))
18 %         'MaxIter' : maximum number of Newton iterations (Default = 10)
19 %         'Display' : if true the some info are shown (Default = true)
20 %         'TolX'    : tolerance for the step size in Newton iterations
21 %                     (Default = 1e-8)
22 %         'TolFun'  : tolerance for the residual in Newton iterations
23 %                     (Default = 1e-8)
24 %
25 %    OUTPUT:
26 %
27 %       u   - the parametric points corresponding to x
28 %
29 %
30   ndim = numel (nrb.number);
31   options = struct ('u0'       , .5*ones (ndim, 1), ...
32                     'MaxIter' , 10, ...
33                     'Display' , true, ...
34                     'TolX',      1e-8, ...
35                     'TolFun',    1e-8);
36   % Read the acceptable names
37   optionNames = fieldnames (options);
38   % Count arguments
```

```
39  nargin = length (varargin);
40  if (round (nargin/2) ~= nargin/2)
41     error ('nrbreverse needs propertyName/propertyValue pairs');
42  end
43
44  % Check options passed
45  for pair = reshape (varargin, 2, [])
46    if any (strcmp (pair{1}, optionNames))
47      options.(pair{1}) = pair{2};
48    else
49      error('%s is not a recognized parameter name', pair{1});
50    end
51  end
52
53  % x as column vector
54  x = x(:);
55
56  % Define functions for Newton iteration
57  f = @(U) nrbeval (nrb, num2cell (U)) - x;
58  jac = @(U) nrbjacobian (nrb, num2cell (U));
59
60  % Newton cycle
```

```
61    u_old = options.u0(:);
62    if (iscell (nrb.knots))
63      first_knot = reshape (cellfun (@(x) x(1),nrb.knots), size(u_old));
64      last_knot = reshape (cellfun (@(x) x(end),nrb.knots), size(u_old));
65    else
66      first_knot = nrb.knots(1);
67      last_knot = nrb.knots(end);
68    end
69    convergence = false;
70
71    for iter = 1:options.MaxIter
72      u_new = u_old - jac (u_old) \ f (u_old);
73      % Check if the point is outside the parametric domain
74      u_new = max (u_new, first_knot);
75      u_new = min (u_new, last_knot);
76
77      % Error control
78      if (norm (u_new - u_old) < options.TolX && norm (f (u_new)) <
          options.TolFun)
79        if (options.Display)
80          fprintf ('Newton scheme converged in %i iteration.\n', iter);
81                end
```

```
82          convergence = true;
83          break;
84        end
85
86        u_old = u_new;
87
88      end
89      u = u_new;
90
91        if (~convergence)
92  %       fprintf ('Newton scheme reached the maximum number of iterations
        (%i) without converging.\n', options.MaxIter);
93        u=[-1 -1];
94      end
95  end
96  function jac = nrbjacobian (nrb, u)
97      ders = nrbderiv (nrb);
98      [~, jac] = nrbdeval (nrb, ders, u);
99      jac = [jac{:}];
100 end
101 %!test
102 %! nrb = nrb4surf ([0 0], [1 0], [2 3], [5 4]);
```

```
%! p = nrbeval (nrb, {.25 .75});
%! u = nrbreverse (nrb, p, 'Display', false);
%! assert (norm (u - [.25; .75]) < 1e-8);
%!
```

Sample Input

```
nrb

        form: 'B-NURBS'
         dim: 4
      number: [13  3]
       coefs:  [4133 double]
       knots: {[116 double]  [0  0  0  1  1  1]}
       order: [3  3]

x

0.500000000000000   -0.250000000000000                    0

false
```

Sample Output

```
u
```

```
0.812500000000000    1.000000000000000
```

6.2 Appendix B : MATLAB code to compute Gauss point coordinates and associated weights of additional degrees of freedom

This section contains the MATLAB code to compute the Gauss point coordinates and associated weights of the additional degrees of freedom generated during the implementation of the level set method

```
function [W,Q]=discontQ4quad(order,phi)
corner = [1 2 3 4 1];
node   = [-1 -1; 1 -1; 1 1; -1 1];
% loop on element edges
for i = 1 : 4
    n1 = corner(i);
    n2 = corner(i+1);
    if ( phi(n1)*phi(n2) < 0 )
        r    = phi(n1)/(phi(n1)-phi(n2));
        pnt  = (1-r)*node(n1,:)+r*node(n2,:);
        node = [node;pnt];
```

```
12      end
13  end
14  % get decomposed triangles
15  tri = delaunay(node(:,1),node(:,2));
16  tri = tricheck(node,tri);
17  % loop over subtriangles to get quadrature points and weights
18  pt = 1;
19  for e = 1:size(tri,1)
20      [w,q]=quadrature(order,'TRIANGULAR',2);
21      % transform quadrature points into the parent element
22      coord = node(tri(e,:),:);
23      a     = det([coord,[1;1;1]])/2;
24      if ( a<0 )  % need to swap connectivity
25          coord = [coord(2,:);coord(1,:);coord(3,:)];
26          a = det([coord,[1;1;1]])/2;
27      end
28
29      if ( a~=0 )
30          for n=1:length(w)
31              N=lagrange_basis('T3',q(n,:));
32              w(n)
33              Q(pt,:) = N'*coord;
```

```
34                W(pt,1) = 2*w(n)*a;
35                pt = pt+1;
36            end
37        end
38    end
```

Sample Input

```
1  discontQ4quad(2,[2.602179124425164    2.784333568219847
       2.887301263230200    2.710205519913958])
```

Sample Output

```
1  W =
2
3      0.666666666666600
4      0.666666666666600
5      0.666666666666600
6      0.666666666666600
7      0.666666666666600
8      0.666666666666600
9
10 Q =
11
12     0.666666666666600    0.666666666666600
```

```
13    −0.333333333333400    0.666666666666600
14     0.666666666666600   −0.333333333333400
15    −0.666666666666600    0.333333333333200
16    −0.666666666666600   −0.666666666666800
17     0.333333333333400   −0.666666666666800
```

Bibliography

[1] W. Zhao and R. K. Kapania, "Buckling analysis of unitized curvilinearly stiffened composite panels," *Composite Structures*, vol. 135, pp. 365–382, 2016.

[2] S. Shojaee, E. Izadpanah, N. Valizadeh, and J. Kiendl, "Free vibration analysis of thin plates by using a NURBS-based isogeometric approach," *Finite Elements in Analysis and Design*, vol. 61, pp. 23–34, 2012.

[3] J. Mackerle, "Finite element analysis of fastening and joining: a bibliography (1990-2002)," *International Journal of Pressure Vessels and Piping*, vol. 80.4, pp. 253–271, 2003.

[4] T. T. Le, *Finite Element Stress Analysis of a Three-dimensional Threaded Screw*. PhD thesis, California State University, Long Beach, 2001.

[5] S. Sawa, I. Mitsutoshi, O. Yuya, and T. Sawa, "3-D FEM Stress Analysis of Screw Threads in Bolted Joints Under Static Tensile Loadings," in *ASME 2014 International Mechanical Engineering Congress and Exposition*, pp. 36–43, American Society of Mechanical Engineers, 2014.

[6] R. M. Rafatpanah, *Finite Element Analysis of a Three-dimensional Threaded Structural Fastener*. PhD thesis, Rensselaer Polytechnic Institute, Troy, N.Y, 2013.

[7] Y. Shoji and T. Sawa, "Stress concentration at the root of bolt thread," in *ASME*

2010 Pressure Vessels and Piping Division/K-PVP Conference, pp. 427–432, American Society of Mechanical Engineers, 2010.

[8] M. M. Islam and R. K. Kapania, "Global–local finite element analysis of adhesive joints and crack propagation," *Journal of Aircraft*, vol. 51, no. 1, pp. 310–319, 2014.

[9] T. Fukuoka and M. Nomura, "Proposition of helical thread modeling with accurate geometry and finite element analysis," *Journal of Pressure Vessel Technology*, vol. 130.1, no. 011204, 2008.

[10] G. M. Henson and B. A. Hornish, "An evaluation of common analysis methods for bolted joints in launch vehicles," in *51st AIAA/ASME/ASCE/AHS/ASC Structures, Structural Dynamics, and Materials Conference*, (Orlando, Florida), pp. 3022–3049, 12 - 15 April 2010.

[11] J. B. Ransom and N. F. Knight, "Global/local stress analysis of composite panels," *Computers & Structures*, vol. 37, no. 4, pp. 375–395, 1990.

[12] R. K. Kapania, S. G. Haryadi, and R. T. Haftka, "Global/local analysis of composite plates with cutouts," *Computational Mechanics*, vol. 19, no. 5, pp. 386–396, 1997.

[13] S. Haryadi, R. Kapania, and R. Haftka, "Global/local analysis of composite plates with cracks," *Composites Part B: Engineering*, vol. 29, no. 3, pp. 271–276, 1998.

[14] M. Jrad, M. R. Sunny, and R. K. Kapania, "Global–local analysis of composite plate with thin notch," *Journal of Aircraft*, vol. 51, no. 3, pp. 967–974, 2014.

[15] W. J. Renton, D. Olcott, W. Roeseler, R. Batzer, W. Baron, and A. Velicki, "Future of flight vehicle structures (2000 to 2023)," *Journal of Aircraft*, vol. 41, no. 5, pp. 986–998, 2004.

[16] A. K. Noor, W. S. Burton, and C. W. Bert, "Computational Models for Sandwich Panels and Shells," *Applied Mechanics Reviews*, vol. 49, no. 3, p. 155, 1996.

[17] W. S. Burton and A. K. Noor, "Three-dimensional solutions for thermomechanical stresses in sandwich panels and shells," *Journal of Engineering Mechanics*, vol. 120, no. 10, pp. 2044–2071, 1994.

[18] A. K. Noor and W. S. Burton, "Three Dimensional Solutions for Thermal Buckling of Multilayered Anisotropic Plates," *Journal of Engineering Mechanics*, vol. 118, no. 4, pp. 683–701, 1992.

[19] L.-W. Chen and L.-Y. Chen, "Thermal Buckling of Laminated Composite Plates," *Journal of Thermal Stresses*, vol. 10, no. 4, pp. 345–356, 1987.

[20] C. H. Wu and T. R. Tauchert, "Thermoelastic analysis of laminated plates I: Symmetric specially orthotropic laminates," *Journal of Thermal Stresses*, vol. 3, no. 2, pp. 247–259, 1980.

[21] W. J. Chen, P. D. Lin, and L. W. Chen, "Thermal buckling behavior of thick composite laminated plates under nonuniform temperature distribution," *Computers and Structures*, vol. 41, no. 4, pp. 637–645, 1991.

[22] M. Prabhu and R. Dhanaraj, "Thermal buckling of laminated composite plates," *Computers & Structures*, vol. 53, no. 5, pp. 1193–1204, 1994.

[23] R. Rolfes, A. K. Noor, and H. Sparr, "Evaluation of transverse thermal stresses in composite plates based on first-order shear deformation theory," *Computer Methods in Applied Mechanics and Engineering*, vol. 167, no. 3-4, pp. 355–368, 1998.

[24] T. Kant and R. Khare, "Finite element thermal stress analysis of composite laminates using a higher-order theory," *Journal of Thermal Stresses*, vol. 17, no. 2, pp. 229–255, 1994.

[25] C. Sarath Babu and T. Kant, "Refined higher order finite element models for thermal buckling of laminated composite and sandwich plates," *Journal of Thermal Stresses*, vol. 23, no. 2, pp. 111–130, 2000.

[26] T. Kant and C. Babu, "Thermal buckling analysis of skew fibre-reinforced composite and sandwich plates using shear deformable finite element models," *Composite Structures*, vol. 49, no. 1, pp. 77–85, 2000.

[27] A. J. Ferreira, L. M. Castro, and S. Bertoluzza, "A high order collocation method for the static and vibration analysis of composite plates using a first-order theory," *Composite Structures*, vol. 89, no. 3, pp. 424–432, 2009.

[28] L. V. Tran, A. J. Ferreira, and H. Nguyen-Xuan, "Isogeometric analysis of functionally graded plates using higher-order shear deformation theory," *Composites Part B: Engineering*, vol. 51, pp. 368–383, 2013.

[29] C. H. Thai, S. Kulasegaram, L. V. Tran, and H. Nguyen-Xuan, "Generalized shear deformation theory for functionally graded isotropic and sandwich plates based on isogeometric approach," *Computers and Structures*, vol. 141, pp. 94–112, 2014.

[30] J. N. Reddy, "A Simple Higher-Order Theory for Laminated Composite Plates," *Journal of Applied Mechanics*, vol. 51, no. 4, p. 745, 1984.

[31] H. Nguyen-Xuan, L. V. Tran, C. H. Thai, S. Kulasegaram, and S. P. Bordas, "Isogeometric analysis of functionally graded plates using a refined plate theory," *Composites Part B: Engineering*, vol. 64, pp. 222–234, 2014.

[32] A. J. Ferreira, C. M. Roque, and R. M. Jorge, "Analysis of composite plates by trigonometric shear deformation theory and multiquadrics," *Computers and Structures*, vol. 83, no. 27, pp. 2225–2237, 2005.

[33] E. Carrera, "Evaluation of Layerwise Mixed Theories for Laminated Plates Analysis," *AIAA Journal*, vol. 36, no. 5, pp. 830–839, 1998.

[34] H. Murakami, "Laminated Composite Plate Theory With Improved In-Plane Responses," *Journal of Applied Mechanics*, vol. 53, no. 3, pp. 661–666, 1986.

[35] T. J. Hughes, J. A. Cottrell, and Y. Bazilevs, "Isogeometric analysis: CAD, finite elements, NURBS, exact geometry and mesh refinement," *Computer Methods in Applied Mechanics and Engineering*, vol. 194, no. 39-41, pp. 4135–4195, 2005.

[36] Austin Cottrell, J.; Hughes, T.J.R.; Bazilevs, Y., *Isogeometric Analysis: Toward Integration of CAD and FEA*. John Wiley & Sons, 2009.

[37] J. A. Cottrell, A. Reali, Y. Bazilevs, and T. J. Hughes, "Isogeometric analysis of structural vibrations," *Computer methods in Applied Mechanics and Engineering*, vol. 195, no. 41-43, pp. 5257–5296, 2006.

[38] N. D. Manh, A. Evgrafov, A. R. Gersborg, and J. Gravesen, "Isogeometric shape optimization of vibrating membranes," *Computer Methods in Applied Mechanics and Engineering*, vol. 200, no. 13-16, pp. 1343–1353, 2011.

[39] Y. Bazilevs, M.-C. Hsu, and M. Scott, "Isogeometric fluid–structure interaction analysis with emphasis on non-matching discretizations, and with application to wind turbines," *Computer Methods in Applied Mechanics and Engineering*, vol. 249, pp. 28–41, 2012.

[40] N. Nguyen-Thanh, N. Valizadeh, M. Nguyen, H. Nguyen-Xuan, X. Zhuang, P. Areias, G. Zi, Y. Bazilevs, L. De Lorenzis, and T. Rabczuk, "An extended isogeometric thin shell analysis based on Kirchhoff–Love theory," *Computer Methods in Applied Mechanics and Engineering*, vol. 284, pp. 265–291, 2015.

[41] L. V. Tran, H. A. Ly, J. Lee, M. A. Wahab, and H. Nguyen-Xuan, "Vibration analysis of cracked FGM plates using higher-order shear deformation theory and extended isogeometric approach," *International Journal of Mechanical Sciences*, vol. 96, pp. 65–78, 2015.

[42] H. Kapoor and R. K. Kapania, "Geometrically nonlinear NURBS isogeometric finite element analysis of laminated composite plates," *Composite Structures*, vol. 94, no. 12, pp. 3434–3447, 2012.

[43] H. Kapoor, R. K. Kapania, and S. R. Soni, "Interlaminar stress calculation in composite and sandwich plates in NURBS Isogeometric finite element analysis," *Composite Structures*, vol. 106, pp. 537–548, 2013.

[44] L. V. Tran, C. H. Thai, H. T. Le, B. S. Gan, and J. Lee, "Engineering Analysis with Boundary Elements Isogeometric analysis of laminated composite plates based on a four-variable refined plate theory," *Engineering Analysis with Boundary Elements*, vol. 47, pp. 68–81, 2014.

[45] P. Phung-Van, L. V. Tran, A. Ferreira, H. Nguyen-Xuan, and M. Abdel-Wahab, "Nonlinear transient isogeometric analysis of smart piezoelectric functionally graded material plates based on generalized shear deformation theory under thermo-electro-mechanical loads," *Nonlinear Dynamics*, vol. 87, no. 2, pp. 879–894, 2017.

[46] E. Carrera, "Transverse Normal Strain Effect on Thermal Stress Analysis of Homogeneous and Layered Plates," *AIAA Journal*, vol. 43, no. 10, pp. 2232–2242, 2005.

[47] X. Qin, C. Dong, F. Wang, and Y. Gong, "Free vibration analysis of isogeometric curvilinearly stiffened shells," *Thin-Walled Structures*, vol. 116, pp. 124–135, 2017.

[48] M. Mukhopadhyay and A. Mukherjee, "Finite element buckling analysis of stiffened plates," *Computers & structures*, vol. 34, no. 6, pp. 795–803, 1990.

[49] B. G. Prusty and S. Satsangi, "Finite element transient dynamic analysis of laminated stiffened shells," *Journal of Sound and Vibration*, vol. 248, no. 2, pp. 215–233, 2001.

[50] G. Eccher, K. J. R. Rasmussen, and R. Zandonini, "Elastic buckling analysis of perforated thin-walled structures by the isoparametric spline finite strip method," *Thin-Walled Structures*, vol. 46, no. 2, pp. 165–191, 2008.

[51] G. B. Chai, "Free vibration of laminated composite plates with a central circular hole," *Composite Structures*, vol. 35, no. 4, pp. 357–368, 1996.

[52] M. Aydin Komur, F. Sen, A. Ataş, and N. Arslan, "Buckling analysis of laminated composite plates with an elliptical/circular cutout using FEM," *Advances in Engineering Software*, vol. 41, no. 2, pp. 161–164, 2010.

[53] D. Kumar and S. B. Singh, "Effects of boundary conditions on buckling and post-buckling responses of composite laminate with various shaped cutouts," *Composite Structures*, vol. 92, no. 3, pp. 769–779, 2010.

[54] G. R. Liu, X. Zhao, K. Y. Dai, Z. H. Zhong, G. Y. Li, and X. Han, "Static and free vibration analysis of laminated composite plates using the conforming radial point interpolation method," *Composites Science and Technology*, vol. 68, no. 2, pp. 354–366, 2008.

[55] C. C. Chen, S. Kitipornchai, C. W. Lim, and K. M. Liew, "Free vibration of symmetrically laminated thick-perforated plates," *Journal of Sound and Vibration*, vol. 230, no. 1, pp. 111–132, 2000.

[56] H. R. Ovesy and J. Fazilati, "Buckling and free vibration finite strip analysis of composite plates with cutout based on two different modeling approaches," *Composite Structures*, vol. 94, no. 3, pp. 1250–1258, 2012.

[57] S. Natarajan, A. J. Ferreira, and H. Nguyen-Xuan, "Analysis of cross-ply laminated plates using isogeometric analysis and unified formulation," *Curved and Layered Structures*, vol. 1, no. 1, pp. 1–10, 2014.

[58] T. T. Yu, S. Yin, T. Q. Bui, and S. Hirose, "A simple FSDT-based isogeometric analysis for geometrically nonlinear analysis of functionally graded plates," *Finite Elements in Analysis and Design*, vol. 96, no. C, pp. 1–10, 2015.

[59] Y. Bazilevs, C. Michler, V. M. Calo, and T. J. Hughes, "Isogeometric variational multiscale modeling of wall-bounded turbulent flows with weakly enforced boundary conditions on unstretched meshes," *Computer Methods in Applied Mechanics and Engineering*, vol. 199, no. 13-16, pp. 780–790, 2010.

[60] Y. Bazilevs, V. M. Calo, T. J. R. Hughes, and Y. Zhang, "Isogeometric fluid-structure interaction: theory, algorithms, and computations," *Computational Mechanics*, vol. 43, no. 1, pp. 3–37, 2008.

[61] J. A. Evans, Y. Bazilevs, I. Babuška, and T. J. Hughes, "n-Widths, *sup*-infs, and optimality ratios for the k-version of the isogeometric finite element method," *Computer Methods in Applied Mechanics and Engineering*, vol. 198, no. 21-26, pp. 1726–1741, 2009.

[62] T. J. R. Hughes, A. Reali, and G. Sangalli, "Efficient quadrature for NURBS-based isogeometric analysis," *Computer Methods in Applied Mechanics and Engineering*, vol. 199, no. 5-8, pp. 301–313, 2010.

[63] F. Auricchio, F. Calabrò, T. J. Hughes, A. Reali, and G. Sangalli, "A simple algorithm for obtaining nearly optimal quadrature rules for NURBS-based isogeometric analysis," *Computer Methods in Applied Mechanics and Engineering*, vol. 249-252, pp. 15–27, 2012.

[64] N. Valizadeh, T. Bui, V. Vu, H. Thai, and M. Nguyen, "Isogeometric Simulation for Buckling, Free and Forced Vibration of Orthotropic Plates," *International Journal of Applied Mechanics*, vol. 05, no. 02, p. 1350017, 2013.

[65] S. Yin, J. S. Hale, T. Yu, T. Q. Bui, and S. P. Bordas, "Isogeometric locking-free plate element: A simple first order shear deformation theory for functionally graded plates," *Composite Structures*, vol. 118, no. 1, pp. 121–138, 2014.

[66] C. V. Verhoosel, M. A. Scott, T. J. R. Hughes, and R. de Borst, "An isogeometric analysis approach to gradient damage models," *International Journal for Numerical Methods in Engineering*, vol. 86, no. 1, pp. 115–134, 2011.

[67] J. Lu, "Isogeometric contact analysis: Geometric basis and formulation for frictionless contact," *Computer Methods in Applied Mechanics and Engineering*, vol. 200, no. 5-8, pp. 726–741, 2011.

[68] W. A. Wall, M. A. Frenzel, and C. Cyron, "Isogeometric structural shape optimization," *Computer Methods in Applied Mechanics and Engineering*, vol. 197, no. 33-40, pp. 2976–2988, 2008.

[69] J. Kiendl, K.-U. Bletzinger, J. Linhard, and R. Wüchner, "Isogeometric shell analysis with Kirchhoff–Love elements," *Computer Methods in Applied Mechanics and Engineering*, vol. 198, no. 49-52, pp. 3902–3914, 2009.

[70] J. Kiendl, Y. Bazilevs, M. C. Hsu, R. Wüchner, and K. U. Bletzinger, "The bending strip method for isogeometric analysis of Kirchhoff-Love shell structures comprised of multiple patches," *Computer Methods in Applied Mechanics and Engineering*, vol. 199, no. 37-40, pp. 2403–2416, 2010.

[71] L. A. Piegl and W. Tiller, "Geometry-based triangulation of trimmed NURBS surfaces," *Computer-Aided Design*, vol. 30, no. 1, pp. 11–18, 1998.

[72] S. Shojaee, N. Valizadeh, E. Izadpanah, T. Bui, and T. V. Vu, "Free vibration and buckling analysis of laminated composite plates using the NURBS-based isogeometric finite element method," *Composite Structures*, vol. 94, no. 5, pp. 1677–1693, 2012.

[73] R. Schmidt, R. Wüchner, and K. U. Bletzinger, "Isogeometric analysis of trimmed NURBS geometries," *Computer Methods in Applied Mechanics and Engineering*, vol. 241-244, pp. 93–111, 2012.

[74] S. S. Ghorashi, N. Valizadeh, and S. Mohammadi, "Extended isogeometric analysis for

simulation of stationary and propagating cracks," *International Journal for Numerical Methods in Engineering*, vol. 89, no. 9, pp. 1069–1101, 2012.

[75] E. Rank, M. Ruess, S. Kollmannsberger, D. Schillinger, and A. Düster, "Geometric modeling, isogeometric analysis and the finite cell method," *Computer Methods in Applied Mechanics and Engineering*, vol. 249-252, pp. 104–115, 2012.

[76] D. Schillinger, L. Dedè, M. A. Scott, J. A. Evans, M. J. Borden, E. Rank, and T. J. Hughes, "An isogeometric design-through-analysis methodology based on adaptive hierarchical refinement of NURBS, immersed boundary methods, and T-spline CAD surfaces," *Computer Methods in Applied Mechanics and Engineering*, vol. 249-252, pp. 116–150, 2012.

[77] W. S. Burton and A. K. Noor, "Three Dimensional Solutions for Thermomechanical Stresses in Sandwich Panels and Shells," *Journal of Engineering Mechanics*, vol. 120, no. 10, pp. 2044–2071, 1994.

[78] A. Y. Tamijani and R. K. Kapania, "Buckling and Static Analysis of Curvilinearly Stiffened Plates Using Mesh-Free Method," *AIAA Journal*, vol. 48, pp. 2739–2751, Dec 2010.

[79] P. Shi, R. K. Kapania, and C. Y. Dong, "Vibration and Buckling Analysis of Curvilinearly Stiffened Plates Using Finite Element Method," *AIAA Journal*, vol. 53, no. 5, pp. 1319–1335, 2015.

[80] P. Hao, B. Wang, K. Tian, G. Li, and X. Zhang, "Optimization of curvilinearly stiffened panels with single cutout concerning the collapse load," *International Journal of Structural Stability and Dynamics*, vol. 16, no. 07, p. 1550036, 2016.

[81] K. Liew, Y. Xiang, S. Kitipornchai, and M. Lim, "Vibration of rectangular Mindlin plates with intermediate stiffeners," *Journal of Vibration and Acoustics*, vol. 116, no. 4, pp. 529–535, 1994.

[82] K. Liew, Y. Xiang, S. Kitipornchai, and J. Meek, "Formulation of Mindlin-Engesser model for stiffened plate vibration," *Computer Methods in Applied Mechanics and Engineering*, vol. 120, no. 3-4, pp. 339–353, 1995.

[83] J. Reddy and A. Khdeir, "Buckling and vibration of laminated composite plates using various plate theories," *AIAA Journal*, vol. 27, no. 12, pp. 1808–1817, 1989.

[84] E. Carrera, F. Miglioretti, and M. Petrolo, "Accuracy of refined finite elements for laminated plate analysis," *Composite Structures*, vol. 93, no. 5, pp. 1311–1327, 2011.

[85] R. Rikards, A. Chate, and O. Ozolinsh, "Analysis for buckling and vibrations of composite stiffened shells and plates," *Composite Structures*, vol. 51, no. 4, pp. 361–370, 2001.

[86] S. Patel, P. Datta, and A. H. Sheikh, "Buckling and dynamic instability analysis of stiffened shell panels," *Thin-Walled Structures*, vol. 44, no. 3, pp. 321–333, 2006.

[87] H. Zeng and C. Bert, "A differential quadrature analysis of vibration for rectangular stiffened plates," *Journal of Sound and Vibration*, vol. 241, no. 2, pp. 247–252, 2001.

[88] G. Wei, Y. Zhao, and Y. Xiang, "Discrete singular convolution and its application to the analysis of plates with internal supports. Part 1: Theory and algorithm," *International Journal for Numerical Methods in Engineering*, vol. 55, no. 8, pp. 913–946, 2002.

[89] Y. Zhao, G. Wei, and Y. Xiang, "Discrete singular convolution for the prediction of high frequency vibration of plates," *International Journal of Solids and Structures*, vol. 39, no. 1, pp. 65–88, 2002.

[90] L. Zhou and W. X. Zheng, "Moving least square Ritz method for vibration analysis of plates," *Journal of Sound and Vibration*, vol. 290, no. 3-5, pp. 968–990, 2006.

[91] M. Olson and C. Hazell, "Vibration studies on some integral rib-stiffened plates," *Journal of Sound and Vibration*, vol. 50, no. 1, pp. 43–61, 1977.

[92] M. Olson, "Efficient modelling of blast loaded stiffened plate and cylindrical shell structures," *Computers & Structures*, vol. 40, no. 5, pp. 1139–1149, 1991.

[93] O. K. Bedair and M. Troitsky, "A study of the fundamental frequency characteristics of eccentrically and concentrically simply supported stiffened plates," *International Journal of Mechanical Sciences*, vol. 39, no. 11, pp. 1257–1272, 1997.

[94] Z.-S. Liu, J. Hansen, and D. Oguamanam, "Eigenvalue sensitivity analysis of stiffened

plates with respect to the location of stiffeners," *Structural Optimization*, vol. 16, no. 2-3, pp. 155–161, 1998.

[95] A. H. Sheikh and M. Mukhopadhyay, "Large amplitude free flexural vibration of stiffened plates," *AIAA Journal*, vol. 34, no. 11, pp. 2377–2383, 1996.

[96] *ANSYS 16.0 User Help Manual*.

[97] M. Leapchuse, "Schaum's Outline of Theory and Problems of Differential Geometry," 1969.

[98] L. Martini and R. Vitaliani, "On the polynomial convergent formulation of a C^0 isoparametric skew beam element," *Computers and Structures*, vol. 29, no. 3, pp. 437–449, 1988.

[99] P. Shi, R. K. Kapania, and C. Dong, "Vibration and buckling analysis of curvilinearly stiffened plates using finite element method," *AIAA Journal*, vol. 53, no. 5, pp. 1319–1335, 2015.

[100] L. Piegl and W. Tiller, *The NURBS Book*. Springer Science & Business Media, 2012.

[101] Y. Bazilevs, V. M. Calo, J. A. Cottrell, J. A. Evans, T. J. Hughes, S. Lipton, M. A. Scott, and T. W. Sederberg, "Isogeometric analysis using T-splines," *Computer Methods in Applied Mechanics and Engineering*, vol. 199, no. 5-8, pp. 229–263, 2010.

[102] L. L. Piegl and W. Tiller, *The NURBS Book*, vol. 28. Springer Science & Business Media, 1996.

[103] L. V. Tran, M. A. Wahab, and S.-E. Kim, "An isogeometric finite element approach for thermal bending and buckling analyses of laminated composite plates," *Composite Structures*, vol. 179, pp. 35–49, 2017.

[104] A. Avci, S. Kaya, and B. Daghan, "Thermal buckling of rectangular laminated plates with a hole," *Journal of Reinforced Plastics and Composites*, vol. 24, no. 3, pp. 259–272, 2005.

[105] A. Y. Tamijani and R. K. Kapania, "Buckling and static analysis of curvilinearly stiffened plates using mesh-free method," *AIAA Journal*, vol. 48, no. 12, pp. 2739–2751, 2010.

[106] W. Zhao and R. K. Kapania, "Buckling analysis of unitized curvilinearly stiffened composite panels," *Composite Structures*, vol. 135, pp. 365–382, 2016.

[107] L. V. Tran, M. A. Wahab, and S. E. Kim, "An isogeometric finite element approach for thermal bending and buckling analyses of laminated composite plates," *Composite Structures*, vol. 179, pp. 35–49, 2017.

[108] T. Kant and C. S. Babu, "Thermal buckling analysis of skew fibre-reinforced composite and sandwich plates using shear deformable finite element models," *Composite Structures*, vol. 49, no. 1, pp. 77–85, 2000.

[109] A. Avci, S. Kaya, and B. Daghan, "Thermal buckling of rectangular laminated plates with a hole," *Journal of Reinforced Plastics and Composites*, vol. 24, no. 3, pp. 259–272, 2005.

[110] M. Huang and T. Sakiyama, "Free vibration analysis of rectangular plates with variously-shaped holes," *Journal of Sound and Vibration*, vol. 226, no. 4, pp. 769–786, 1999.

[111] T. Q. Bui, M. N. Nguyen, and C. Zhang, "An efficient meshfree method for vibration analysis of laminated composite plates," *Computational Mechanics*, vol. 48, no. 2, pp. 175–193, 2011.

[112] X. Cui, G. Liu, G. Li, and G. Zhang, "A thin plate formulation without rotation dofs based on the radial point interpolation method and triangular cells," *International journal for numerical methods in engineering*, vol. 85, no. 8, pp. 958–986, 2011.

[113] G. R. Liu and X. L. Chen, "A mesh-free method for static and free vibration analyses of thin plates of complicated shape," *Journal of Sound and Vibration*, vol. 241, no. 5, pp. 839–855, 2001.